

DEVELOPMENT OF VIRTUAL 3D TACTILE DISPLAY
BASED ON ELECTROMAGNETIC LOCALIZATION

By

Kai Deng

A Dissertation Submitted to the Faculty of the
Department of Aerospace and Mechanical Engineering

In Partial Fulfillment of the Requirements

For the Degree of

DOCTOR OF PHILOSOPHY

With a Major in

MECHANICAL ENGINEERING

In the Graduate College

THE UNIVERSITY OF ARIZONA

2009

THE UNIVERSITY OF ARIZONA
GRADUATE COLLEGE

As members of the Dissertation Committee, we certify that we have read the dissertation prepared by Kai Deng, entitled Development of Virtual Tactile Display Based on Electromagnetic Localization, and recommend that it be accepted as fulfilling the dissertation requirement for the Degree of Doctor of Philosophy.

Eniko T. Enikov	4/13/2009
	Date
John G. Williams	4/13/2009
	Date
Parviz E. Nikraves	4/13/2009
	Date
Olgierd A. Palusinski	4/13/2009
	Date

Final approval and acceptance of this dissertation is contingent upon the candidate's submission of the final copy of the dissertation to the Graduate College.

I hereby certify that I have read the dissertation prepared under my direction and recommend that it be accepted as fulfilling the dissertation requirement.

Dissertation Director: Eniko T. Enikov	Date
--	------

STATEMENT BY AUTHOR

This dissertation has been submitted in partial fulfillment of requirements for an advanced degree at the University of Arizona and is deposited in the University Library to be made available to borrowers under rules of the Library.

Brief quotations from this dissertation are allowable without special permission, provided that accurate acknowledgement of source is made. Requests for permission for extended quotation from or reproduction of this manuscript in whole or in part may be granted by the head of the major department or the Dean of the Graduate College when in his or her judgment the proposed use of the material is in the interests of scholarship. In all other instances, however, permission must be obtained from the author.

SIGNED: _____
Kai Deng

ACKNOWLEDGEMENTS

I would like to sincerely acknowledge the consistent support from my advisor Dr. Enikov. Under his supervision, I developed an active work fashion and gradually approached toward the completion of this dissertation. I also wish to give many thanks to my colleagues Mr. Vasco Polyzoev and Mr. Edward White for their consistent help with the experiment aspects of this project. Thanks are also expressed to Mr. Dale Drew for his excellent work and tremendous patience to the mechanical machining requested by this project.

I greatly appreciate the support from my wife, Qian. She gave me significant help in electromagnetic simulation, provided feedback of my work, and has been consistently patient and tolerant to my busy life throughout 4 years study. At last but not the least, thanks my parents Huaigui Deng and Guanglin Yuan and my sister Tao Deng. Without their understandings and supports, none of this would be possible.

For my daughter Sarah

TABLE OF CONTENTS

LIST OF FIGURES	8
LIST OF FIGURES-CONTINUED.....	9
LIST OF FIGURES-CONTINUED.....	10
LIST OF TABLES	11
ABSTRACT.....	12
1. INTRODUCTION	14
1.1 Overview of Existing Tactile Display Devices	14
1.2 Motivation and Description of the Proposed Device	20
2. DESIGN OF THE ELECTROMAGNETIC LOCALIZATION SYSTEM.....	24
2.1 Principle of EM Positioning.....	25
2.2 3DOF Position Detection	32
2.3 Signal Processing Steps.....	34
2.3.1 Signal Generation.....	34
2.3.2 Received Signal Processing.....	38
2.4 EM Interference.....	45
2.5 Position Measurement Results	49
2.5.1 Position Calibration	50
2.5.2 Time-budget Design.....	54
3. DESIGN OF ELECTROMAGNETIC ACTUATOR	57
3.1 Concept I: Eddy Current Actuator Method	57
3.2 Concept II: Permanent Magnet Actuator Method	65
3.3 Perception Limit of Vibratory Stimulation.....	75
4. SYSTEM INTEGRATION	79
4.1 Device structure and Experiment Setup	79
4.2 Heat Sink Design.....	80
5. EVALUATION	84
5.1 Shape Perception Test.....	84

TABLE OF CONTENTS-CONTINUED

5.2 Discussion and Future Work	92
6. CONCLUSION.....	94
APPENDICES	96
APPENDIX A: COMPLETE CIRCUIT SCHEMATICS	97
1. DRIVER BOARD SCHEMATICS.....	97
2. RECEIVER BOARD SCHEMATICS	98
APPENDIX B: MATLAB SOURCE CODE.....	99
1. Main code	99
2. Functions	104
APPENDIX C: ASSEMBLY SOURCE CODE.....	105
1. PIC16F690 Source Code for Position Control.....	105
2. PIC16F684 Source Code for Actuation Frequency Control.....	127
APPENDIX D: ANSYS SOURCE CODE	131
REFERENCES	134

LIST OF FIGURES

Fig. 1-1 2D tactile display based on electromagnetically driven resonators.	15
Fig. 1-2 2D tactile display based on multilayer MEMS design.	16
Fig. 1-3 2D image display by using large actuators screen.	17
Fig. 1-4 3D tactile display by using pin array driven by stepping motors.	18
Fig. 1-5 3D tactile display formed by pin array with refined height varying step.	18
Fig. 1-6 Integrated VR device formed by PHANToM and CyberGlove	20
Fig. 1-7 Block diagram of human-in-loop shape display.	21
Fig. 1-8 Main components and signal of the proposed tactile display system.	22
Fig. 2-1 Working principle of a general position detector.	24
Fig. 2-2 Hall Effect principle illustration.	26
Fig. 2-3 Working principle of magnetoresistive sensor	27
Fig. 2-4 Working principle of AC magnetic field measurement.	30
Fig. 2-5 Principle of AC EM position measurement.	33
Fig. 2-6 Signal generation circuit configuration.	35
Fig. 2-7 (a) The simulated frequency response and (b) simulated and measured transient response of the bandpass filter.	37
Fig. 2-8 Main signal processing steps.	38
Fig. 2-9 Parallel bandpass filter for signal amplification.	38
Fig. 2-10 Frequency response of the parallel bandpass reponse.	40
Fig. 2-11 Designed amplifier circuit for signal amplification.	41
Fig. 2-12 Active low pass filter configuration.	43
Fig. 2-13 Photograph of the PCB containing signal processing module.	44
Fig. 2-14 Bode plot of the low pass filter.	44
Fig. 2-15 Skin depth of human and copper as function of frequency.	46
Fig. 2-16 FEA model for EM interference simulation.	47
Fig. 2-17 Interference percentage versus distance.	48
Fig. 2-18 Photograph of the fabricated device with the separation distance suggested from simulation results.	49
Fig. 2-19 Simulation results of 1% interference boundary.	49
Fig. 2-20 Distortion caused by position measurement error.	51
Fig. 2-21 Position measurement results within display area where $Z=166$ mm.	53
Fig. 2-22 The working space is divided into 8 small cuboids for position calibration.	53
Fig. 2-23 Parallel timing design for PC and microcontroller.	54

LIST OF FIGURES-CONTINUED

Fig. 2-24 Measured computation time per cycle.	55
Fig. 2-25 Display of data sampling rate over users scanning rate.	56
Fig. 3-1 Repulsive force generated from 2 current filaments.	58
Fig. 3-2 Calculation model for two coils by dividing their cross sections.	59
Fig. 3-3 Electrical system implementation for eddy current based EM actuation.	60
Fig. 3-4 Block diagram of the simulation process.	61
Fig. 3-5 SIMULINK model of the force simulation.	62
Fig. 3-6 Coil geometry used in simulation.	63
Fig. 3-7 Simulation results of force and velocity.	64
Fig. 3-8 Simulation results for driving current and armature current.	65
Fig. 3-9 Working principle of permanent magnet based EM actuation.	66
Fig. 3-10 Equivalent current source model of a permanent magnet.	67
Fig. 3-11 Coil geometry parameter definition.	69
Fig. 3-12 Force simulation based on coil's geometry.	71
Fig. 3-13 Winding machine for coil's fabrication.	72
Fig. 3-14 Measured flux density at bottom and top surface of the magnet.	73
Fig. 3-15 Measured force characteristics versus input current.	74
Fig. 3-16 Experiment setup for measuring magnetic force.	74
Fig. 3-17 Experiment setup for vibration stimulation test.	75
Fig. 3-18 Schematic illustration of the charging/discharging curve of the capacitor. .	76
Fig. 3-19 Frequency response of the actuation energy efficiency.	77
Fig. 3-20 Frequency preference of the perception threshold.	78
Fig. 4-1 (a) Photograph of the device and (b) tactile display spatially defined by 3 beacon coils, and the master circuit board for signal transmission	80
Fig. 4-2 Schematic illustration of the device structure.	80
Fig. 4-3 Power density as a function of vibration frequency.	81
Fig. 4-4 Simulation structure of (a) actuator attached to holder and (b) actuator attached to heat sink	82
Fig. 4-5 Steady state temperature of the device with and without heat sink.	83
Fig. 5-1 (a) Photograph of the device setup (b) Shape test set 1 from 2 volunteers. ...	85

LIST OF FIGURES-CONTINUED

- Fig. 5-2 Shape test set 2 (a) 2 horizontal plates with 6 mm thickness and 50 mm separation; (b) 2 vertical plates with 10 mm thickness and 50 mm separation; (c) cube of 70 mm side length; (a1 a2 a3, b1 b2 b3 and c1 c2 c3) are correspondent perceived shapes drawn by volunteers. The vibration frequency inside these shapes is fixed at 75 Hz, no vibration outside shapes.87
- Fig. 5-3 Shape test set 3 (a) L shape structure; (b) Half sphere with 65 mm radius; (c) Half hollow sphere with outer and inner radius of 60 mm and 37 mm respectively. (a1 a2 a3, b1 b2 b3 and c1 c2 c3) are correspondent perceived shapes drawn by volunteers. The vibration frequency for (a) is 75 Hz inside shape, no vibration outside the shape; for (b) is 15 Hz at center of sphere, and linearly increase to 120 Hz at the surface, no vibration outside the sphere; for (c) is 15 Hz at the middle of inner and outer surface, and linearly increase to 120 Hz at inner and outer sphere surfaces.89
- Fig. 5-4 Shape test set 4 (a) sphere with 35 mm radius (b) hollow sphere with outer and inner radius of 30 mm and 20 mm respectively. (a1 a2 a3 and b1 b2 b3) are correspondent perceived shapes drawn by volunteers. The vibration frequency is identically configured to shape test 2 (b) and 2 (c).91
- Fig. 5-5 Multiple actuator solution to (a) thin plate display and (b) curved surface display.93

LIST OF TABLES

TABLE 2-1 PARAMETERS OF BEACON COIL.....	36
TABLE 2-2 PARAMETERS OF BANDPASS FILTER.....	40
TABLE 3-1 PARAMETERS OF ACTUATOR	72
TABLE 3-2 VIBRATION TEST RESULTS.....	78

ABSTRACT

This dissertation describes the development of an assist-device aimed to deliver 3D graphic information to the visually impaired people. A human-in-loop approach was used to analyze whether a virtual 3D shape can be transferred correctly to the human users.

The proposed device consists of two major parts: (a) A system of position sensors for real time localization based on magnetization, and (b) A single vibratory actuator working at varied frequencies based on its real time location. The error bound of the position measurement was tested to be 2 mm, which defined the machine resolution of the shape display. In order to realize the refresh rate of the localization that can follow user's scanning speed, the parallel data processing sequences for computer and microcontroller were designed. Additionally, vibratory electromagnetic (EM) actuators were discussed based on eddy current and permanent magnet methods. The simulation study showed that eddy current method was not applicable for millimeter size coil. Accordingly, the permanent magnet method was developed and the force detection threshold of human tactile perceptions was studied.

Virtual shape perception experiments were made with participation of 3 volunteers who were not aware of the 3D shape information prior to the tests. Based on the four sets of shape tests, we conclude that the majority of the shape information is able to be delivered to users by using the proposed device. Difficulties for perceiving the

local sharp profile e.g. thin plates and large curvature in small shapes may be better addressed by multiple actuators simultaneously providing shape information in the local boundary detection.

The major contribution of this dissertation is the 3D shape display implemented by a miniature and low cost device. The developed device utilizes both passive stimulation and active search so that a commonly used large scale actuators matrix based on mere active touch method is avoided. The studies on the required force/energy input from the actuator showed that EM actuators can be miniaturized to millimeter scale without sacrificing the ability to induce tactile stimulation. Additional uniqueness of the proposed system is the ability to present hollow features, which is impossible to display by the existing devices.

1. INTRODUCTION

With the emergence of the World Wide Web (WWW), the scientific presentations increasingly involve graph media and illustrations. The people lacking eyesight are accordingly facing the increasing difficulty to access the progress of the technology and catch up with their up-to-date education. Although several types of computer-aided software were devised to transfer selective information into Braille language, the major obstacle of the communication for visually impaired people is the deficient delivery of the graphic information. The most reliable way to introduce a certain shape or graph to them is to actually produce a physical model. While rapid prototyping technology allows production of such models, its cost and size requirements are prohibitively high for everyday use. As a reason, the interest in devising tactile display devices has been significantly increasing.

1.1 Overview of Existing Tactile Display Devices

Among the existing tactile display devices, major progress has been made in regard to alphanumeric and two dimensional (2D) graphics display based on spatially discriminated stimulation onto human skin. An example is the magnetic resonator based 2D tactile display developed by Fukuda et al [1], which is shown in Figure 1-1. The device contains 3×3 tactile vibrator array. The vibration of each actuator produces “1” or “0” state to form the line presentation. This actuators array has a relatively

large spacing, 4 mm, because of the cross talk between the neighboring actuators.

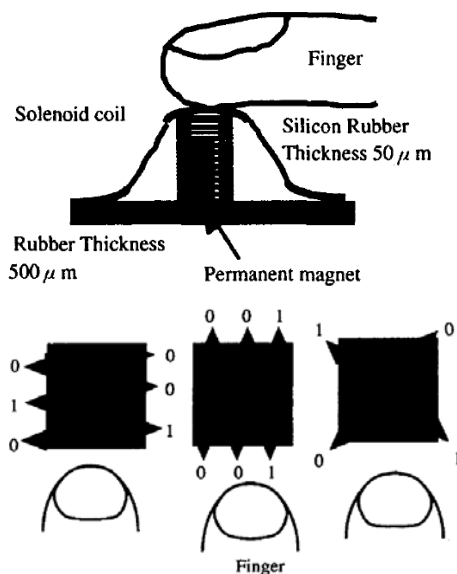


Fig. 1-1 2D tactile display based on electromagnetically driven resonators [1].

A subsequent attempt to produce a miniaturized device, replacing the bulky vibrators was based on micro electro mechanical system (MEMS) technology. Hafez [2] proposed an approach of producing both mechanical and thermal stimulation based on multilayer micro fabrication, which is shown in Figure 1-2. Array of surface-mount micro coils can be fabricated by micromachining process. The printed circuit board (PCB) layer is used to drive the micro coils layer. The third layer containing a flexible magnetic structure is driven by high frequency current to produce vibratory stimulation to the operator. However, the coil's dimension is below sub millimeter range and the according actuation displacement stroke is several micrometers. This amplitude of the vibration is difficult to produce sensations to human skin.

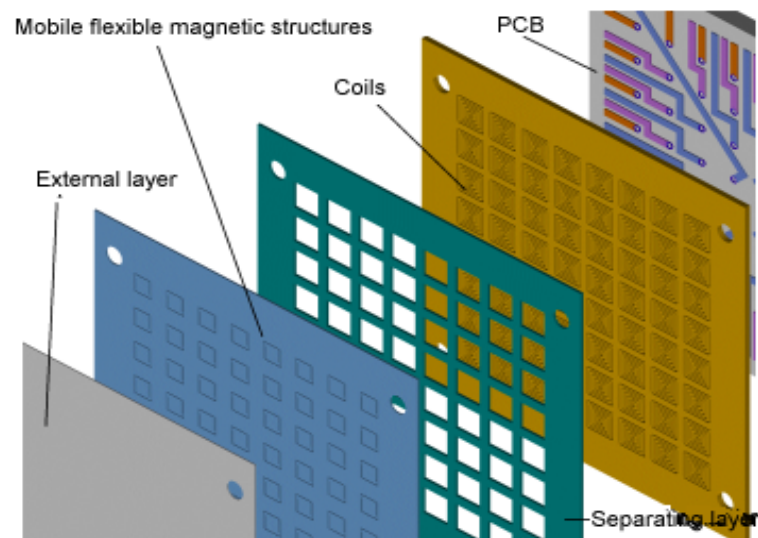


Fig. 1-2 2D tactile display based on multilayer MEMS design [2].

Furthermore, Maucher et al [3] developed a tactile vision substitution system (TVVS) based on large piezoelectric actuator array guided by an optical position sensor in order to display 2D patterns to the blind people. However, a very high voltage (200V) is needed to drive piezoelectric actuator to reach a perceivable displacement (0.7 mm).

Recently, Iwata et al [4] proposed a haptic surface to convey a certain projected 2D image into a rigidity map formed by a large actuators screen. The working principle of the system is shown in Figure 1-3. An image of the virtual object is projected onto the surface of the flexible screen. Deformation of the screen converts the 2D image from the projector into a solid image therefore the user can touch the image directly based on force feedback. However, this device displays shapes by using a complete touch feedback, which is difficult for miniaturization toward

everyday use.

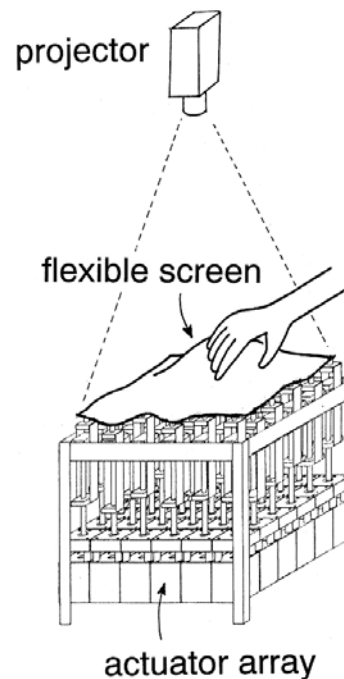


Fig. 1-3 2D image display by using large actuators screen [4].

The devices discussed above all aim to display 2D shapes. While these devices represent an improvement over traditionally Braille-only language, a 2D projection to our three dimensional (3D) world often remains difficult to interpret. In order to introduce the 3rd dimension of the shape, Kawai et al [5, 6] proposed to use pin array with varied raised height to mimic 3D surfaces. The device contains pin arrays spacing 5 mm driven by stepping motors, depicted by Figure 1-4. The controlled signal to each motor comes from a computer input command.

A similar system developed by Shinohara et al [7] containing 64×64 pin matrix is shown in Figure 1-5. The raised height has a more refined step (0.1 mm) compared with [6]. The presented 3D figure is converted into the control signal of each driver of

the pin. These two 3D tactile display devices, however, are facing two major challenges. Firstly, it is impossible to present hollow objects since both sides of a surface need to be displayed. Secondly, the actual size of the perception platform must be large in order to incorporate a complete active touch feedback, thus difficult for potential miniaturization.

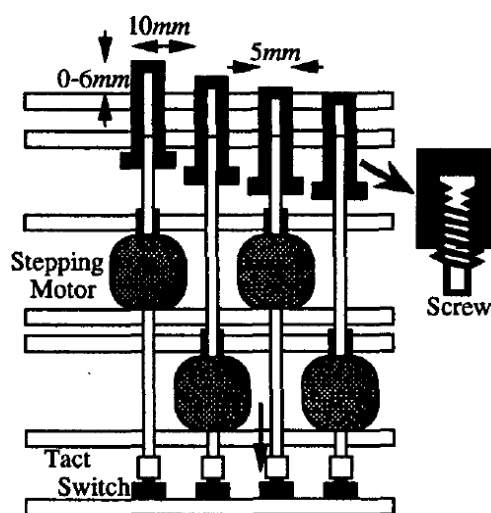


Fig. 1-4 3D tactile display by using pin array driven by stepping motors [6].

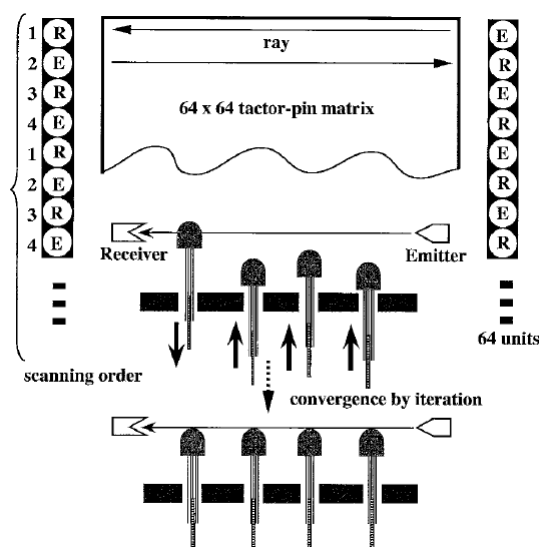


Fig. 1-5 3D tactile display formed by pin array with refined height varying step [7].

Recent attempt was to use non-contact method based on ultrasound for producing tactile sensation [8]. The non-contact method inherently improves the tactile distinction during perception. However, the proposed device has a limited spatial resolution of 20 mm, which makes it difficult to display a complex object containing small features.

Another group of devices, known as virtual reality (VR) devices, have been exploited as impressing the operators by tracing the virtual object through force feedback [9-12]. However, most of the existing VR devices serve the purpose of providing interaction for sighted people to manipulate virtual objects, thus are more or less associated with visual complexity and visual interactivity with virtual environment. One effort to enhance accessibility of visually-impaired people to VR tools was made by Nikolakis et al [13], who developed the integration of two VR devices- PHANToMTM (referred as personal haptic interface mechanism [9]) and CyberGraspTM data glove [14] shown in Figure 1-6.

The combined device provides force feedback to all five fingers and palm such that a sense of grasp turns to be more realistic compared with single PHANToM device, and meanwhile benefits from preventing penetration before grasping the object compared with single CyberGrasp device. Although this specially designed virtual environment is developed for customized applications, the complexity of hardware, the complexity of 3D virtual environment as well as the inefficiency in using combination of both devices partially undermine its merit [13]. Additionally,

like the general VR devices that do not allow penetration of the object surfaces, the integrated tool is not suitable for displaying hollow 3D shapes within a closed surface.

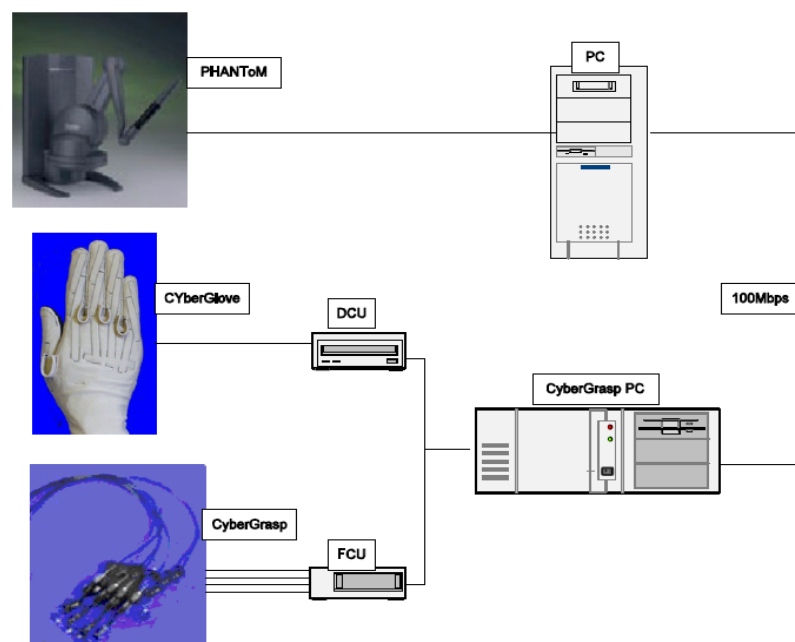


Fig. 1-6 Integrated VR device formed by PHANToM and CyberGlove [13].

1.2 Motivation and Description of the Proposed Device

This dissertation proposes a 3D tactile display device based on vibrotactile feedback realized by an alternate current (AC) activated electromagnetic (EM) position detector combined with a wearable EM actuator. The advantage of vibrotactile device is the smaller actuation effort required to stimulate the skin, which leads to the convenience toward miniaturization. 100 μm stroke is reported to be sufficient to perceive vibrotactile information exerted on fingertip [15]. According to the stiffness of fingertip pressed against flat surface which is 3.5 N/mm for 1 mm displacement [15], the actuation force required for a $2 \times 2 \text{ mm}^2$ actuator under a 20×10

mm² fingertip to produce a 100 μ m perceivable stroke is calculated to be 7 mN. Comparatively, existing 3D tactile display and VR devices typically require sustainability of 1-3 N force [7, 13, 16], which accordingly requires larger power and larger size of the driving element.

The proposed shape perception scheme in this dissertation incorporates a human-in-loop interfaced with computer-generated virtual shape as illustrated by the block diagram in Figure 1-7. The reference shape is recorded through its coordinates for comparison. When the operator's hand moves, the finger's position is measured and compared with reference shape in real time. The comparison results in a decision to command the actuator and produce vibratory stimulation to the finger at an adjustable frequency based on relative positions of fingertip to the shape. By scanning and perceiving the 3D shape, human subjects are able to establish an image of this 3D object. The objective of this study is to conclude whether or not the proposed device can deliver to the users majority of information of a reference 3D shape.

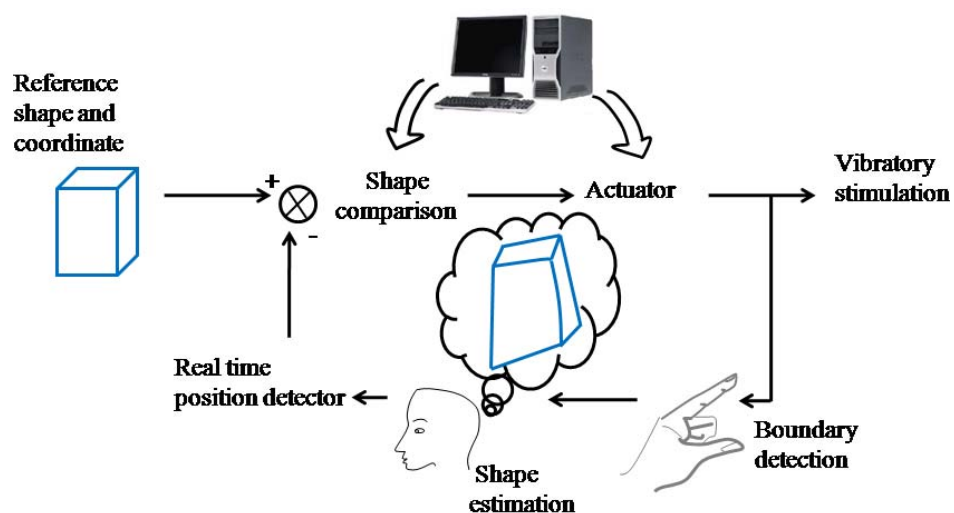


Fig. 1-7 Block diagram of human-in-loop shape display.

Figure 1-8 shows the main components used in this system. During operation, the microcontroller applies a pulse width modulation (PWM) to the beacon coils to create a time-varied magnetic field in the space. EM receivers detect the strength of the magnetic field and send the output voltage to the analog to digital converter (ADC). The digitized data is then fed back to microcontroller therefore providing a continuous localization data source. Personal computer (PC) can retrieve these data through RS 232 communication standard to compute the momentary position. The comparison result of the location and reference shape is then transferred into the value of the actuation frequency and is sent to microcontroller using an external interrupt. The actuator is then engaged to vibrate at the commanded frequency available from 0~977 Hz, providing a continuous vibratory stimulation to user.

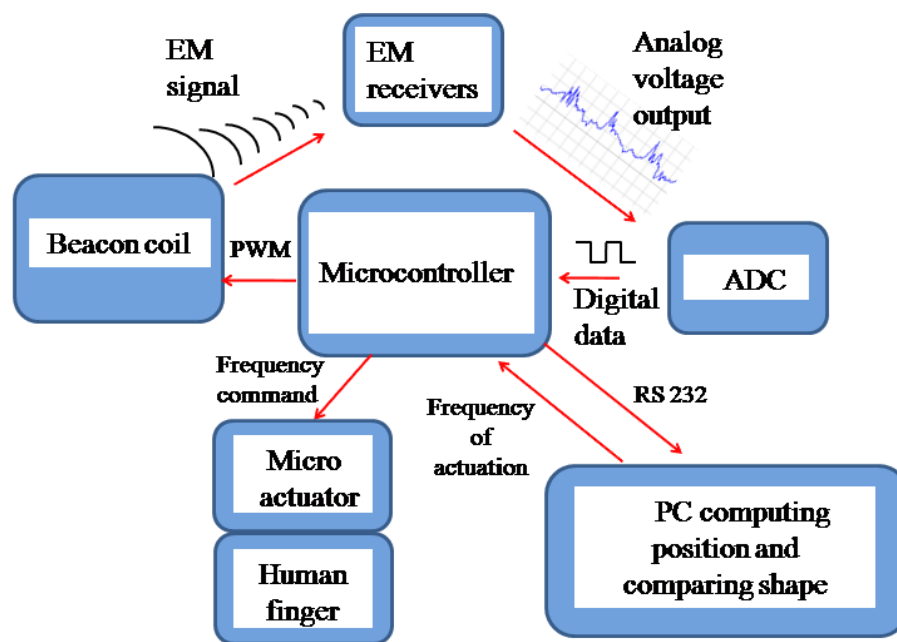


Fig. 1-8 Main components and signal of the proposed tactile display system.

Many types of skin stimulator / tactile actuators have been exploited, which can be generally categorized into thermal, electric and mechanical actuation. The challenge of the thermal actuator is that the changing rate of the temperature is not sufficient to produce a distinct sensation to human skin [2]. On the other hand, the electric actuator suffers from a very low pain threshold and various responses to the same stimulation due to the large variation of the individual electrical impedance [15]. Comparatively, mechanical tactile actuator, also termed as vibrotactile, provides much higher pain threshold [15, 17] as well as more consistent sensation among different users.

For the structure of this dissertation, design of the position detection system is described in chapter 2; design of the vibratory actuator based on electro magnetization is discussed in chapter 3; integration of the device from position detector and actuator is provided in chapter 4; the device evaluation and the experimental results are covered in chapter 5; summary of the dissertation is given in chapter 6.

2. DESIGN OF THE ELECTROMAGNETIC LOCALIZATION SYSTEM

The main components of the position detection comprise signal source, sensor, and signal processor. The working principle of a general position detection is schematically shown in Figure 2-1. The signal source (transmitter) provides a continuously detectable signals transmitting into the space. The signal received by sensor (receiver) is mainly a function of the position. Therefore the output of sensor can be transferred to the processor which contains numeric solvers to compute the positions out of the measurements.

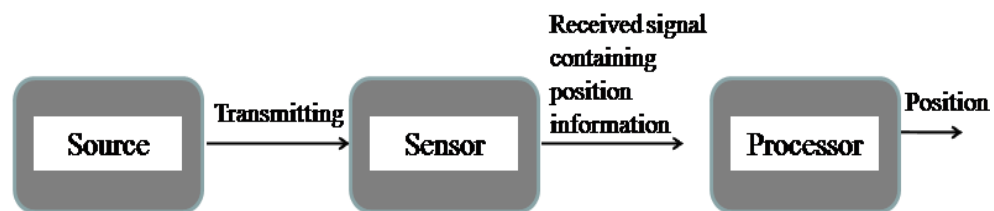


Fig. 2-1 Working principle of a general position detector.

Two types of commonly used position detection schemes are optical and EM methodologies. In optical approach, typical signal source and sensor is light emitting diodes (LEDs) and camera, respectively [18]. The position is computed by the projections of LEDs to the image planes of the cameras. Optical position tracker, however, requires a clear line-of-sight throughout the measurement, which is difficult to adapt to our display system due to the operator's movement.

Comparatively, EM positioning approach is more robust to nearby human

activities because the nonmagnetic and low conductive human body has ignorable disturbance to the intermediate frequency magnetic signal transmission. Different sensing schemes can be utilized to detect magnetic signal that reflects sensor's location. Hall Effect sensor [19] and magnetoresistive sensor [20] are able to measure the static magnetic field in order of milli-Tesla. However, the milli-Tesla range of magnetic field needs to be generated by large scale beacon coil or permanent magnet that works close to sensor. The alternative approach is to inductively detect an alternate current (AC) activated magnetic field by using a multi-turn coil. In this way the sensitivity of the sensor can be boosted by the factor of the operating frequency and coil's number of turns according to Faraday's law of induction [21].

2.1 Principle of EM Positioning

A beacon coil or permanent magnet can create a magnetic field distribution in the space. For static magnetic field (activated by direct current (DC) or created by static permanent magnet), a Hall Effect sensor or magnetoresistive sensor can be used as detector.

Principle of Hall effect is described in Figure 2-2. When applying a constant DC current I across the conductor without external magnetic field, no accumulated charges are built to form the potential across the conductor, as shown in Figure 2-2(a). Assume the presence of a magnetic flux density B perpendicular to the conductor plate, the current will be distorted due to a continuous Lorentz force resulting in the

accumulated charges on the conductor surfaces, shown in Figure 2-2(b). The corresponding potential produced by this external magnetic field can be written as [22]

$$V_H = \frac{I}{dne} \cdot B, \quad (2-1)$$

where d is the thickness of the conductor, n is the charge carrier density, and e is the electron charge. Hall Effect sensor aims to detect V_H of equation (2-1), which is a linear function of the magnetic field flux density in the direction normal to the conductor plane.

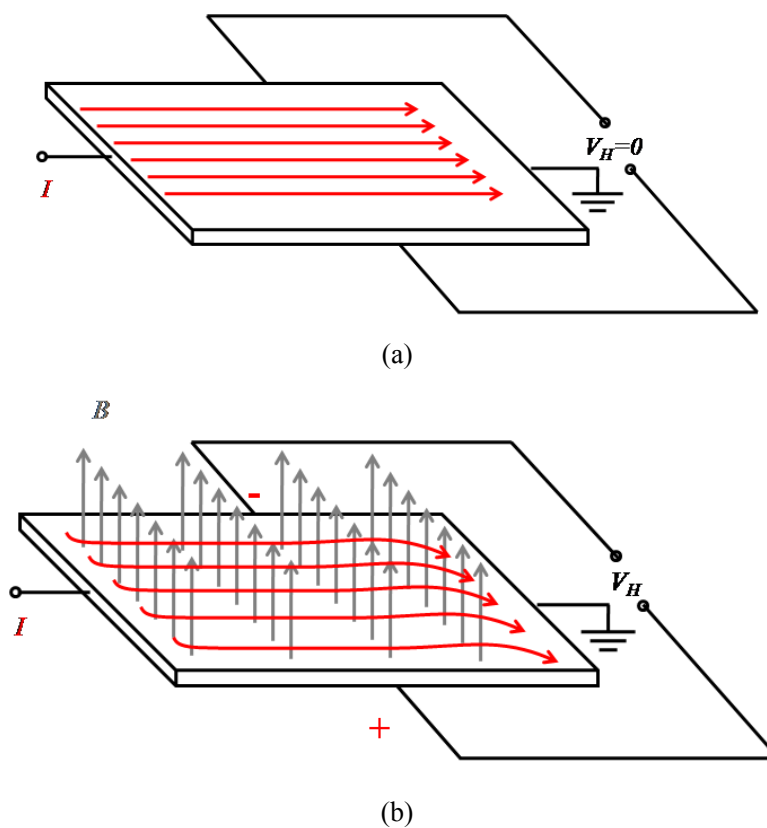


Fig. 2-2 Hall Effect principle illustration.

Magnetoresistive sensors make use of the magnetoresistive effect, the property of a current-carrying magnetic material to change its resistivity in the presence of an external magnetic field. Figure 2-3 shows a strip of ferromagnetic material- permalloy ($\text{Ni}_{81}\text{Fe}_{19}$). Without external field, the permalloy has an internal magnetization vector parallel to the current flow. With the magnetic field H , the internal magnetization vector of the permalloy will rotate around an angle α . As a result, the resistance of the permalloy will change as a function of the rotation angle, as given by [20]

$$R = R_0 + \Delta R_0 \cos^2 \alpha , \quad (2-2)$$

where R_0 and ΔR_0 are material parameters; ΔR_0 is typically in order of 2~3% [20, 23]. Equation (2-2) can be linearized to equation (2-3) when the external field is small compared with permalloy's internal magnetization.

$$R = R_0 + \frac{\Delta R_0}{2} + \Delta R_0 \frac{H_y}{H_0} . \quad (2-3)$$

In equation (2-3), H_0 is the internal magnetization of the permalloy. The change of resistance can be detected by using a Wheatstone bridge circuit.

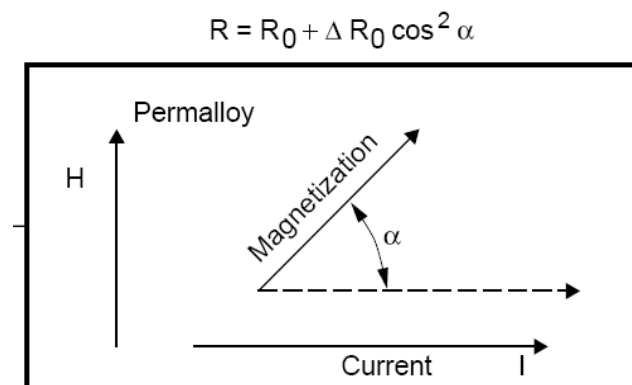


Fig. 2-3 Working principle of magnetoresistive sensor [23].

The static EM detection benefits from the immunity to eddy noise. Adjacent object, even with low conductivity, may generate eddy current caused by the time-varied magnetic field. This eddy noise leads to a location dependent noise with the same frequency of the signal source, which can not be filtered out by general analog filters. The challenge of these two devices for position detection as mentioned previously, is their low sensitivities. Typical sensitivity of the Hall sensor is ranged from 10~30 mV/mT [24, 25]. The highest sensitivity is found to be 280 mV/mT with the output limited to ± 7.5 mV [26]. Magnetoresistive sensor has the same order of sensitivity with the linear output range in 1~10 kA/m. In order to utilize these two sensors to measure position based on milli-Tesla signal distribution, either a bulky thick beacon coil / permanent magnet or the sensor placed very close to the signal source should be used. For tactile display, we plan to allow a 10~20 cm scale effective range for the position detection. An empirical model to calculate this magnetic field for a multi-turn beacon coil is [27]

$$B = \frac{1.5k}{r^3}, \quad (2-4)$$

$$k = \mu_0 INA$$

where r , μ_0 , I , N , A is the distance between sensor and beacon, vacuum permeability, beacon coil's current, beacon coil's number of turns, and beacon coil's area, respectively. For the beacon coil wound by American Wire Gauge (AWG) 26, a maximal allowable DC current is 0.36 A [28]. Assume the diameter of coil is 0.1 m. In order to reach a target flux density of 5 mT to utilize Hall Effect sensor or

magnetostrictive sensor, the number of turns of the coil is calculated to be 7500 through equation (2-4). As a result, the designed coil would be extremely thick, as would cause the error of the flux density formulation. Additionally, the electrical resistance of the coil is more than 500 Ω . Therefore a very high voltage (180 V) needs to be supplied in order to sustain the 0.36 A current, which is not desired for this project. Consequently, an alternative magnetization method is desired. One such method is based on AC excitation.

AC activated EM position detector inductively measures the change of the flux by using small coils. Faraday's induction law [21] states that an electromotive force can be generated due to a change of the magnetic flux through the circuit described by

$$\varepsilon = -\frac{d\phi}{dt}, \quad (2-5)$$

where ε is the electromotive force (induced voltage), and ϕ is the magnetic flux through the coil.

As an AC is applied to the beacon coil, the spatially distributed magnetic field will be established at the same varying frequency. For the intermediate frequency (less than 2 MHz), EM wave propagation time between beacon and sensing coils can be ignored. Therefore the magnetic field is in phase with the driving signal. A amplification factor of operating frequency can be multiplied to the output of sensor. This factor significantly increases the sensor's sensitivity and renders a miniature signal generation system driven by a low supply voltage possible.

Figure 2-4 depicts the principle of sinusoidal positioning system.

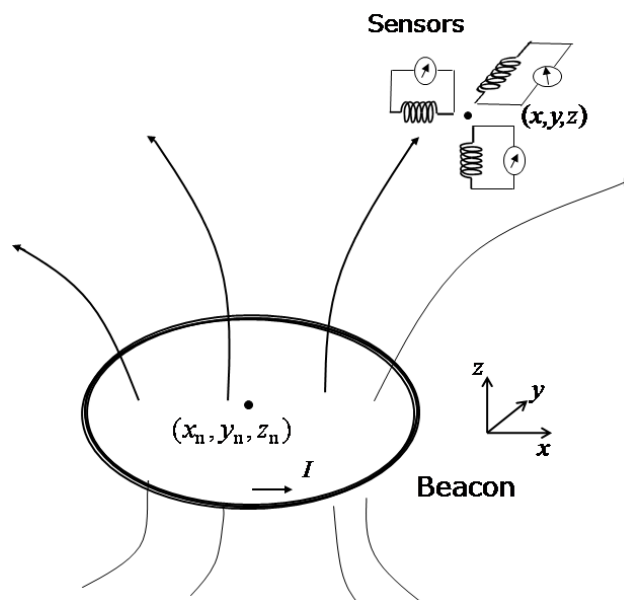


Fig. 2-4 Working principle of AC magnetic field measurement.

As the AC in form of

$$I = I_0 \sin \omega t \quad (2-6)$$

is applied to the beacon coil, the flux density is synchronically created over the space in time domain, which is

$$B = B(x, y, z) \sin \omega t, \quad (2-7)$$

where ω is the angular frequency of applied current. A formulation suitable for numerical calculation derived in [27] is

$$\begin{aligned}
B_x(x, y, z) &= \frac{3k}{r^5} (x - x_n)(z - z_n) \\
B_y(x, y, z) &= \frac{3k}{r^5} (y - y_n)(z - z_n) \\
B_z(x, y, z) &= \frac{k}{r^5} [2(z - z_n)^2 - (x - x_n)^2 - (y - y_n)^2] \\
|B|(x, y, z) &= \sqrt{B_x^2 + B_y^2 + B_z^2} = \frac{k}{r^4} \sqrt{3(z - z_n)^2 + r^2}
\end{aligned} \tag{2-8}$$

where B_x , B_y , B_z and $|B|$ are the x, y, z components and the magnitude of the flux density caused by current I_0 respectively; $k = \mu_0 I_0 N A$, where μ_0 is the free space permeability, N and A are the number of turns and the area of beacon coil respectively; $r = \sqrt{(x - x_n)^2 + (y - y_n)^2 + (z - z_n)^2}$ is the distance between measured location and the center of the n^{th} beacon coil, where (x_n, y_n, z_n) is the corresponding center coordinates of the beacon coil.

To measure this flux density, three small coils are placed perpendicularly with one another to directly measure the induced voltages that accordingly represent three components of the flux density, shown in Figure 2-4. Substitute equations (2-6) and (2-7) into equation (2-5), we obtain the induced voltages as

$$\begin{aligned}
V_\xi &= \omega N_\xi S_\xi B_\xi \cos(\omega t) \\
V_\eta &= \omega N_\eta S_\eta B_\eta \cos(\omega t), \\
V_\zeta &= \omega N_\zeta S_\zeta B_\zeta \cos(\omega t)
\end{aligned} \tag{2-9}$$

where V_i , N_i , S_i ($i = \xi, \eta, \zeta$) are the i^{th} sensor coil's induced voltage, number of turns, and the area; B_i is the flux density's component projected to the i^{th} sensor coil's sensitive direction. Note that there is a 90 degree phase lag between induced voltage and the applied current.

2.2 3DOF Position Detection

Equation (2-9) correlates the measured voltages to the external magnetic field as well as sensor coil's local orientations. In order to obtain the global position of the device, one could directly apply equation (2-9) to each component of the induced voltage and solve the position (x,y,z) and sensor's orientation. However this approach is currently not successful in respects of accuracy and converging time required by shape display. Therefore we used the alternative way to formulate the magnitude of the flux density instead of each component, and aimed to compute an (x, y, z) position without its orientation. This scheme is applicable for single actuator device with the assumption that the 3 sensing coils measure a geometric point. We will discuss the inaccuracy associated with this assumption and the calibration method to correct this error in section 2.4. But on the other hand, we also gain benefits from 3 DOF magnitude formulation over 6 DOF components formulation. Specifically,

- (1) 3 DOF of position extraction needs smaller computing effort, which yields a faster refresh rate of real time localization.
- (2) Complexity in designing a phase (polarity) detection circuit can be avoided because the signal magnitude is always positive.

To measure the magnitude, 3 identical sensing coils are used to keep the linearity between the induced voltage and the magnetic field coorespondance. Square root summation of the three induced voltages shown in equation (2-9) can be written as

$$\begin{aligned}
|V| &= \sqrt{V_{\xi}^2 + V_{\eta}^2 + V_{\zeta}^2} \\
&= \omega NS \sqrt{B_{\xi}^2 + B_{\eta}^2 + B_{\zeta}^2}, \\
&= \omega NS |B|
\end{aligned} \tag{2-10}$$

where $|B|$ is the magnitude of the flux density vector represented by the resolution of sensing coil's local orientation.

Substitute equation (2-10) into (2-8), we get

$$|V|(x, y, z) = \frac{\omega NSk}{r^4} \sqrt{3(z - z_n)^2 + r^2}. \tag{2-11}$$

In order to uniquely solve the (x, y, z) coordinates by using equation (2-11), a minimum number of 3 beacon coils is needed. The working principle of the 3 DOF position measurement based on magnitude detection is shown in Figure 2-5.

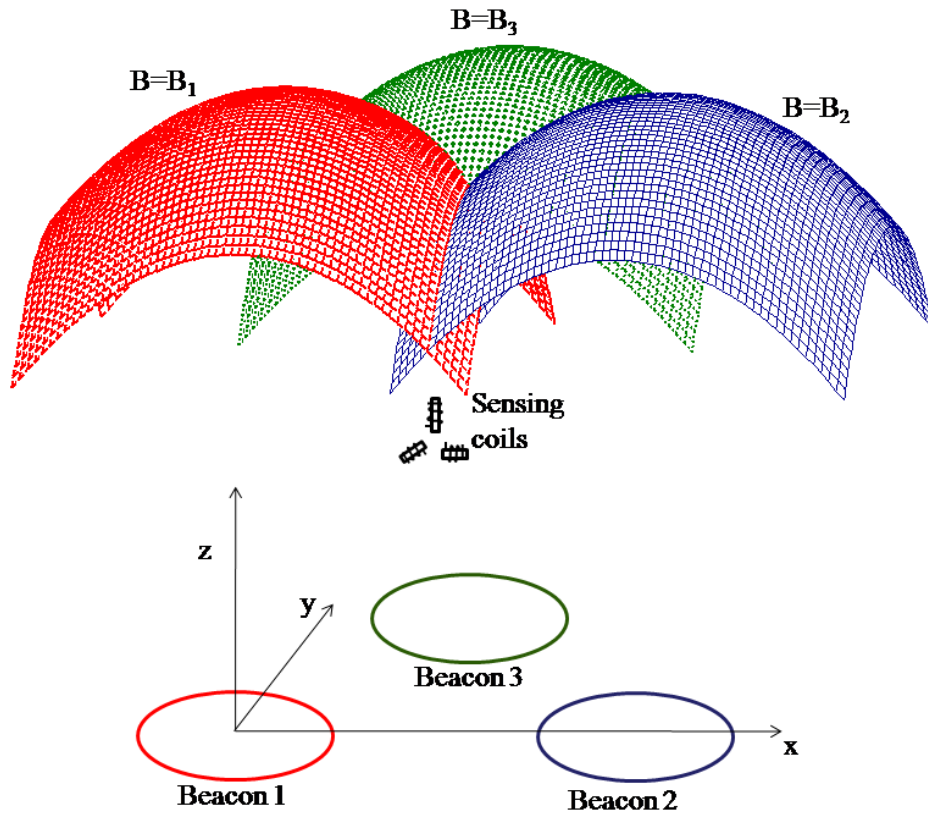


Fig. 2-5 Principle of AC EM position measurement.

During the measurement cycle, the 3 beacon coils are activated sequentially. The mobile sensor consisting of 3 perpendicularly orientated multi-turn coils is localized by matching the measured flux density created by each of the beacon coils. B_1 , B_2 and B_3 are the flux density of the 3 isomagnetic surfaces produced by beacon 1, beacon 2 and beacon 3 respectively. The unique intersection point of these surfaces suggests that the location can be uniquely determined from this signal distribution. The co-planarity of these beacon coils is not a requirement, rather, a convenience. The 3 orthogonal sensing coils are used to measure 3 components of the flux density, whose square roots summation can be computed to represent the magnitude of the flux density vector at that very location.

2.3 Signal Processing Steps

The signal management of the EM position detection consists of two major parts: magnetic signal generation and induced voltage signal processing. The following sections will describe each of them respectively.

2.3.1 Signal Generation

The magnetic field is generated from a periodic pulse signal (working at 125 KHz) applied on the beacon coil. A sharp bandpass filter implemented by serial *RLC* circuit shown in Figure 2-6 is used to eliminate the harmonic components of the square wave. The 5 V peak-peak square wave is realized by the embedded module from PIC16F684

microcontroller, while a field effect transistor (FET) driver is used to increase the pulse amplitude from 5 V to power supply voltage (12 V). Specific in this experiment, we use LM5110-1. Two switches are configured such that one is on while the other is off and accordingly provides periodic charging and discharging to the capacitor C_b and beacon coil with inductance L_b . As a result, the applied pulse voltage is transferred to the AC flowing through the circuit and therefore establishes the sinusoidal magnetic field in the space.

The transfer function of this system can be written as

$$\frac{I_b}{V} = \frac{C_b s}{C_b L_b s^2 + r_b C_b s + 1} \quad , \quad (2-12)$$

where I_b and V are the current passing through the beacon coil and the applied pulse voltage respectively; C_b and r_b are the capacitance and resistance selected for the filter performance; L_b is the inductance of the beacon coil. Table 2-1 shows the parameter of the beacon coil.

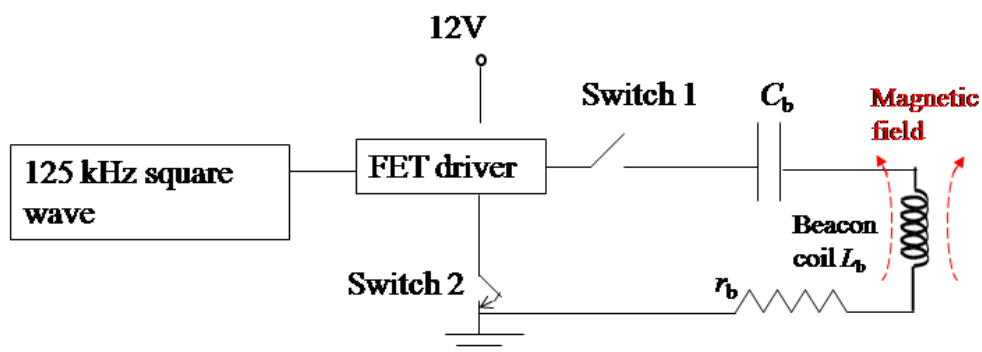
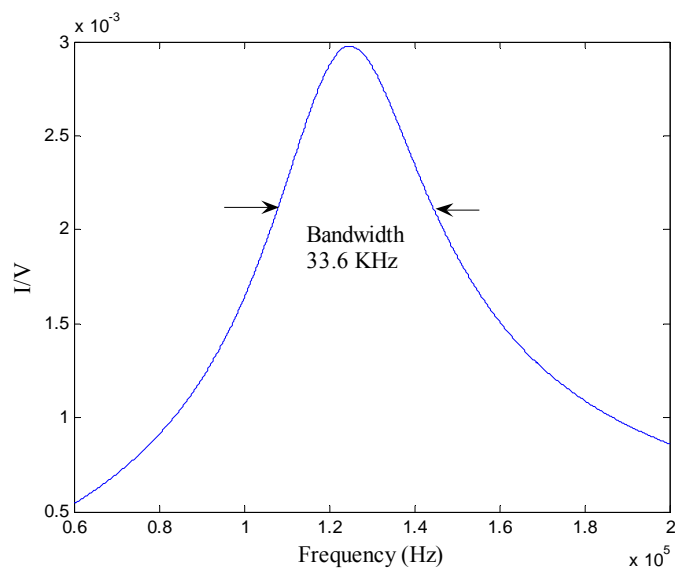


Fig. 2-6 Signal generation circuit configuration.

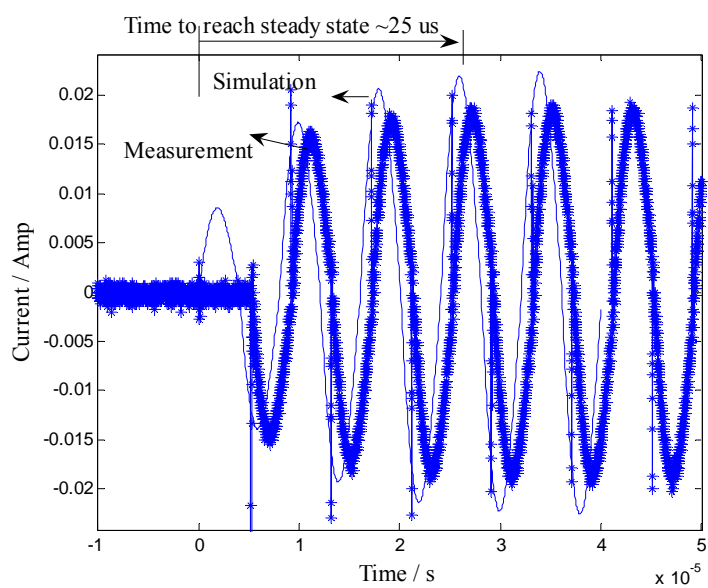
TABLE 2-1
PARAMETERS OF BEACON COIL

Item	Value
Radius	5.1 cm
Number of turns	80
Resistance	4 Ω
Inductance	1.45 mH
Operating frequency	125 KHz

The designed beacon coil has inductance $L_b=1.45$ mH. To realize 125 KHz resonant frequency, we selected C_b by making the second order and zeroth order term of the demoninator in equation (2-12) cancelled out at the corresponding frequency. r_b value determines the amplitude of the current as well as the transient response of system. Small value of r_b will increase the current amplitude but meanwhile lower the speed for the system to reach steady state. A value of $r_b =332 \Omega$ is selected for applicable transient response (25 μ s settling time). The corresponding current amplitude is 18 mA. The simulated frequency and time domain response as well as the measured time-domain waveform are illustrated in Figure 2-7. The simulated and measured results consistantly indicate a settling time of about 25 μ s, which is sufficient for the analog / digital data transmission requirement. The details of system time-budget design will be shown in section 2.5. Note that the measured current amplitude is slightly smaller than simulation results due to a minor mismatch between the capacitance and inductance used for serial filter. The phase delay of the actual measurement in order of micro-seconds is mainly caused by nonzero response time of the IC switches.



(a)



(b)

Fig. 2-7 (a) The simulated frequency response and (b) simulated and measured transient response of the bandpass filter.

2.3.2 Received Signal Processing

The sensing signal is detected by measuring the induced voltage in the periodic varying magnetic field. A block diagram of the main signal processing steps is shown in Figure 2-8.

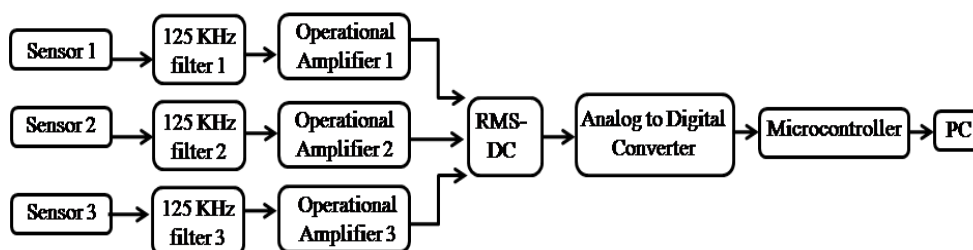


Fig. 2-8 Main signal processing steps.

A second-order band-pass filter is used at the input stage to select the signal at the working frequency of 125 kHz. This filter is specifically a tuned resonant circuit shown in Figure 2-9.

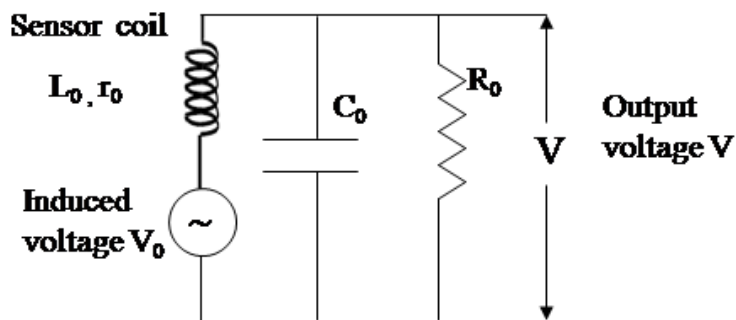


Fig. 2-9 Parallel bandpass filter for signal amplification.

The induced signal is considered as a voltage source that allows current to flow through the sensing coil whose inductance and resistance are L_0 and r_0 , respectively.

The external components, capacitor C_0 and resistor R_0 , are selected to resonate the output voltage at the working frequency 125 kHz. The transfer function of this filter can be described as

$$\frac{V}{V_0} = \frac{R_0}{R_0 C_0 L_0 s^2 + (r_0 R_0 C_0 + L_0) s + r_0 + R_0} \quad , \quad (2-13)$$

The peak response and Q factor can be found by substituting the resonant frequency into equation (2-13). To do this, we enforce the second order and the zeroth order term of the denominator to be cancelled at the center frequency, thus we have

$$-R_0 C_0 L_0 \omega_0^2 + r_0 + R_0 = 0 \quad , \quad (2-14)$$

where ω_0 is the resonant angular frequency. The corresponding magnitude (Q factor) is

$$Q = \left| \frac{V}{V_0} \right|_{\omega_0} = \frac{1}{r_0 \sqrt{\frac{C_0}{L_0}} + \frac{\sqrt{L_0}}{R_0}} \quad (2-15)$$

In order to maximize Q factor, the components C_0 and R_0 are selected such that denominator of (2-15) gets minimum value. For two dependent nonnegative variables, their summation gets minimum value only if they are equal. Therefore we have

$$r_0 \sqrt{\frac{C_0}{L_0}} = \frac{\sqrt{L_0}}{R_0} \quad . \quad (2-16)$$

Combine equations (2-14) and (2-16) and substitute the designed peak frequency

$$\omega_0 = 2\pi \cdot 125 \text{ KHz},$$

we can solve to get C_0 and R_0 . Table 2-2 summaries the components values used in this filter. The designed filter has a frequency response illustrated in Figure 2-10.

TABLE 2-2
PARAMETERS OF BAND PASS FILTER

Parameters	Values
r_0	145 Ω
L_0	7.1 mH
C_0	228 pF
R_0	214 K Ω
ω_0	785400 s^{-1}

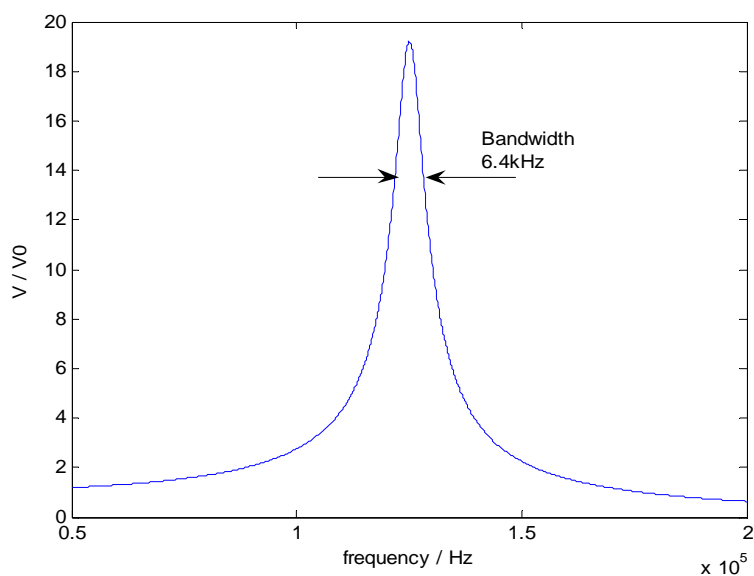


Fig. 2-10 Frequency response of the parallel bandpass response.

According to Figure 2-10, the band pass filter amplifies the induced voltage by 19 times at the resonant frequency. After this filter, the signal needs to be further amplified by using operation amplifier (Op-amp). A practical difficulty lies in the fact

that a convenient PCB circuit board contains only two terminals for power supply, i.e. positive potential and ground. Therefore a negative potential needed for supplying a general difference Op-amp is not available. (Although voltage regulator that provides negative output is available in the market, the output is noisy when the switching frequency of the circuit is higher than regulator's own characteristic frequency). Considering this, all the signal inputs to the difference Op-amp must be offset by half of the rail-rail voltage to assure that the full signal swing is within the rail-rail limit, which is 0~5 V for the current system. However, since the signal to be amplified is a differential voltage across the coil, offsetting both terminals of the coil yields a negative difference voltage in half of its pulse period, which is still out of the rail to rail limit. In order to address this, a circuit configured as Figure 2-11 is used.

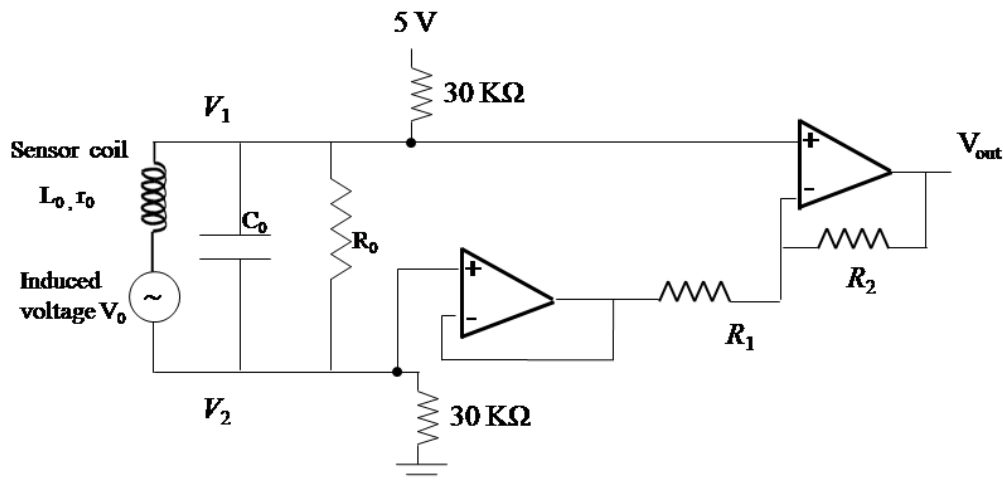


Fig. 2-11 Designed amplifier circuit for signal amplification.

The 125 KHz bandpass filter (identical to Figure 2-9) is offset by two 30 KΩ resistors between power supply (5 V) and ground. These two voltage divider resistors

are selected as 10% of the Op-amp input impedance. Superposition principle yields a DC offset which is equal to 2.5 V added to the original AC induced voltages, V_1 and V_2 . In order to amplify the difference voltage ($V_1 - V_2$), two Op-amps are configured for implementing an overall transfer function of

$$V_{\text{out}} = \frac{R_2}{R_1}(V_1 - V_2) + V_1, \quad (2-17)$$

where V_1 and V_2 are the induced voltages at two terminals of the coil with the 2.5 V DC offset, which can be written as

$$\begin{aligned} V_1 &= 2.5 + V_s \sin(\omega_0 t) \\ V_2 &= 2.5 + V_s \sin(\omega_0 t + \varphi) \end{aligned} \quad (2-18)$$

where V_s is the amplitude of the induced voltage and φ is the phase difference of the two terminals. Substituting equation (2-18) into equation (2-17), we have

$$V_{\text{out}} = 2.5 + \frac{R_2}{R_1}(V_1 - V_2) + V_s \sin(\omega_0 t). \quad (2-19)$$

Equation (2-19) indicates that the output voltage is offset by 2.5 V based on an amplified sinusoidal signal, which is assured to be within 0~5 V rail-rail limit. The tradeoff is that the output signal is not a pure amplification of the induced voltage ($V_1 - V_2$). The extra term $V_s \sin(\omega_0 t)$ coming from V_1 is a disturbance. We select $R_1 = 4.7 \text{ k}\Omega$ and $R_2 = 47 \text{ k}\Omega$ to realize the amplification gain of 10. Under such a high gain, the disturbance term can be negligible. Therefore the overall output signal can be written as

$$V_{\text{out}} \approx 2.5 + \frac{R_2}{R_1}(V_1 - V_2). \quad (2-20)$$

After the signal filtering and amplification, we use an RMS-DC (referred as root mean square to direct current) detector to directly measure the root-mean-square value of this sinusoidal voltage waveform. The converted DC signal is then subjected to an active low pass filter shown in Figure 2-12, so as to remove the 125 kHz frequency noise mixed within the DC signal. The transfer function of this low pass filter can be described as

$$\frac{V_{DC}}{V_{in}} = \frac{1}{(1 + C_3 R_3 s)^2} \quad (2-21)$$

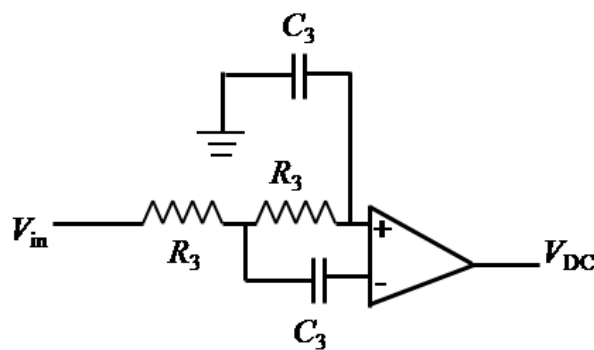


Fig. 2-12 Active low pass filter configuration.

Select $R_3=2.2 \text{ K}\Omega$, $C_3=10 \text{ nF}$, we can obtain a cut off frequency of 4.65 KHz. The magnitude of 125 KHz signal is decreased down to 0.3% (-50 db). The corresponding time constant is 22 μs , which is about the same as the settling time of the signal generation. Bode plot of this system is shown in Figure 2-13. The detailed circuitry design for signal generation and signal processing is shown in Appendix A. The picture of the fabricated printing circuit board (PCB) containing the whole signal processing module is shown in Figure 2-14.

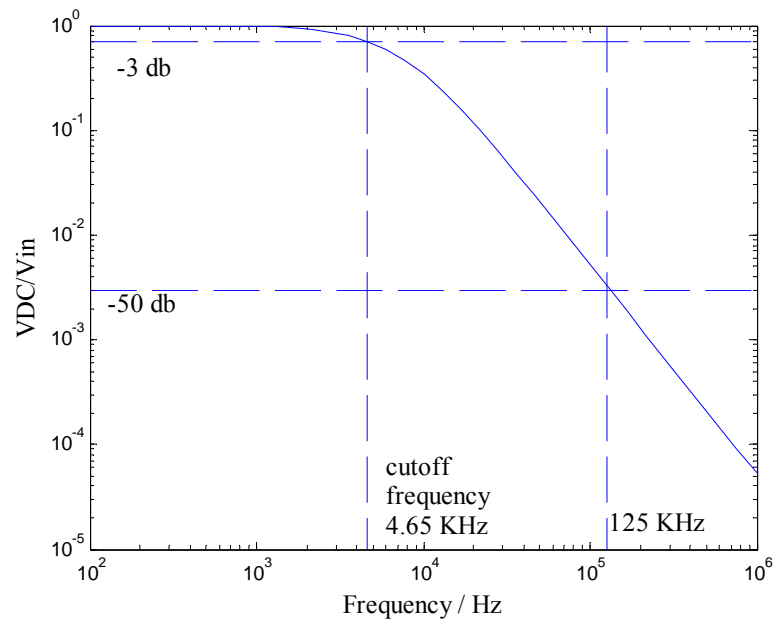


Fig. 2-14 Bode plot of the low pass filter.

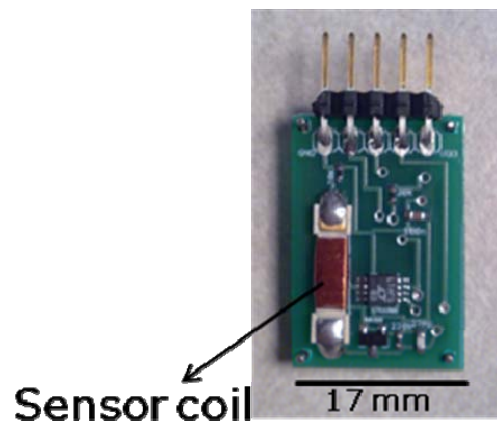


Fig. 2-13 Photograph of the PCB containing signal processing module.

2.4 EM Interference

One of the major environment's disturbances to EM system is the magnetic material that behaves as local magnetic concentrator or annihilator, distorting the adjacent magnetic field lines. The other noise source is the conductor's induction that creates eddy current which opposes the existing magnetic field. Both of these disturbances are not removable by using electronic filtering or compensation.

Since the beacon coils are activated asynchronously, their mutual inductance can be ignored. But the sensing coils containing copper threads and ferrite magnetic core are placed close to each other (to detect the signal toward a small area reflecting a geometric point). Besides, human body's conductivity is another possible disturbance to the EM field. These interferences should be considered.

Skin depth is the parameter for assessing the material's transparency to EM wave. If the skin depth is large enough compared with the material's dimension, then its interference to the magnetic field is negligible.

Figure 2-15 illustrates the skin depth of human and copper as function of frequency by using the formula [28]

$$\delta = \sqrt{\frac{\rho}{\mu_0 \mu_r f \pi}}, \quad (2-22)$$

where ρ is material's resistivity, f is frequency, μ_0 and μ_r is the free space and material permeability, respectively. Resistivity of copper [30] and human [31] is found to be $1.7 \times 10^{-8} \Omega\text{m}$ and $2 \Omega\text{m}$ respectively.

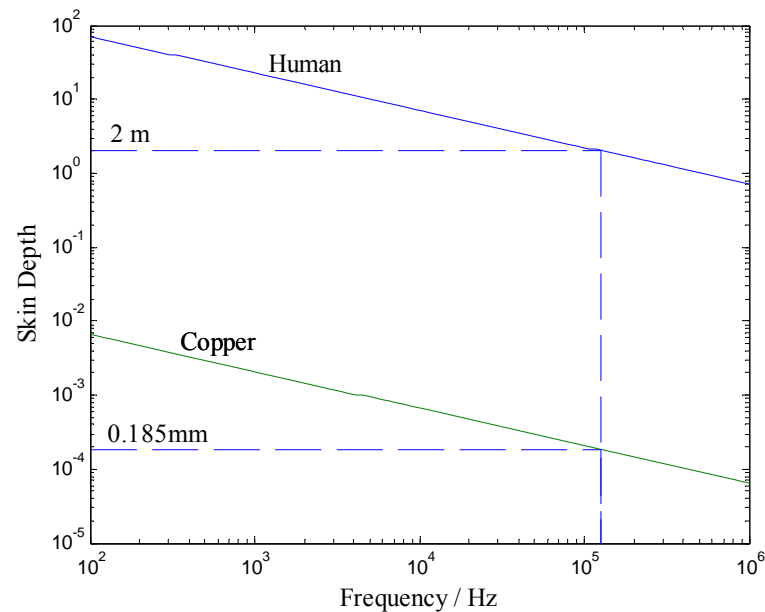


Fig. 2-15 Skin depth of human and copper as function of frequency.

At the 125 kHz working frequency, copper and human have skin depth of 0.185 mm and 2 m, respectively. The sensing coils' dimension is in centimeter's range, which is comparable and even larger than its skin depth. Therefore the interference between these sensing coils should be counted and avoided. From the Figure 2-15, we note that dimension of the human body participated in tactile display (finger and arm) is one order less than its skin depth. Therefore human body's disturbance should be negligible. (The interference factor is in order of $e^{-10} \sim 10^{-5}$)

In order to quantitatively analyze the interferences, finite element analysis (FEA) software COMSOL is used to simulate the signal transmission process. Figure 2-16 shows the simulation model. Signal source is the beacon coil with the radius of 5.08 cm. Cross section of the beacon coil is assumed to be circular with diameter of 5 mm,

shown on the right part of Figure. Sensing coil is placed along the center line of the beacon coil with dimension described in figure. The relative permeability of the core of the sensing coil is set to be 10000. 125 KHz AC with magnitude of 18 mA is applied to beacon coil. Axial symmetrical boundary condition is applied to the center line of coils. Magnetic insulation condition is applied to the other 3 sides of the boundary box.

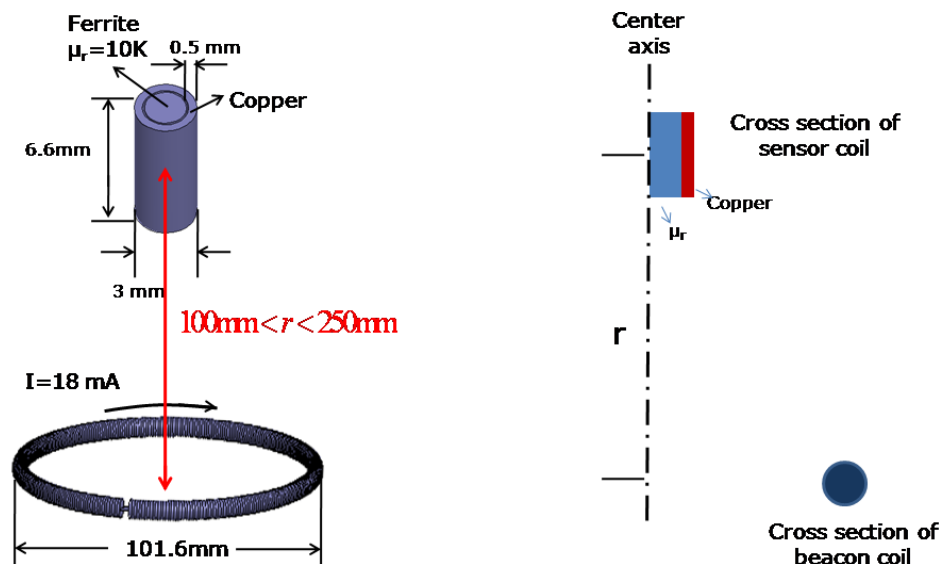


Fig. 2-16 FEA model for EM interference simulation.

The testing point is the assumed position of the center of the adjacent sensing coil, which is 6.6 mm away from the center line. Figure 2-17 shows the percentage of the flux density variation as a function of distance between sensing coil and beacon coil.

The simulation results indicate that the magnetic field can be affected by about 8% by the adjacent sensing coil, and is not dependent on the sensing coil's vertical

locations. In order to reduce this interference, we need to place the sensing coils apart from each other. To calculate the exact distance that sensors should be kept between each other, we use the same simulation to compute how the interference field decay by distance.

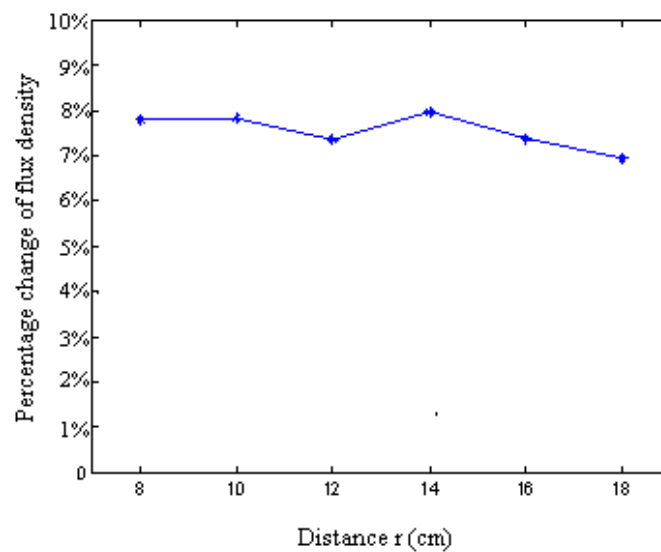


Fig. 2-17 Interference percentage versus distance.

Figure 2-18 shows the simulation results of the two distances between sensing coil and beacon coil: 150mm and 250mm. The 1% interference boundary is drawn by interpolation of multiple test points. This simulation suggests that a 10 mm distance should be kept in order to have a negligible EM interference between each sensor at the two locations where $r=100$ mm and $r=250$ mm. We consider that for other positions between 150 mm and 250 mm, the conclusion is still valid. Based on this result, a design of three sensing coils with 12 mm separation distance is shown in Figure 2-19.

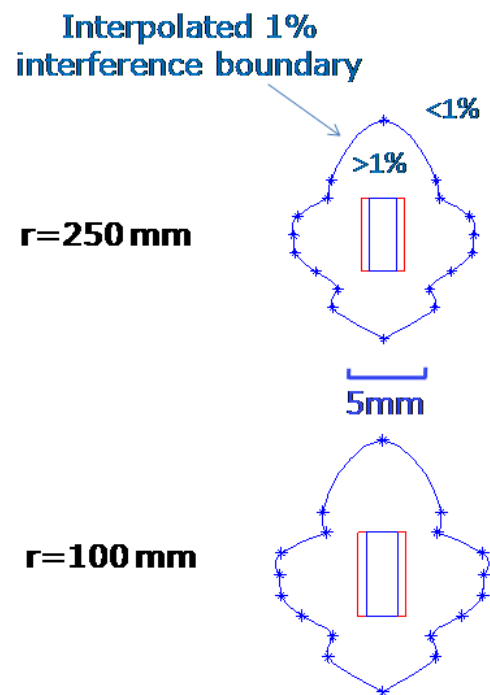


Fig. 2-19 Simulation results of 1% interference boundary.

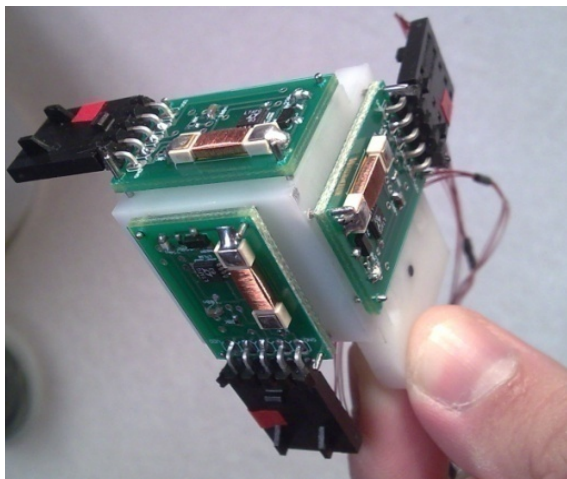


Fig. 2-18 Photograph of the fabricated device with the separation distance suggested from simulation results.

2.5 Position Measurement Results

The accuracy of the position measurement determines the machine resolution of the shape display. The refresh rate of the position measurement decides the speed limit of the user's scanning. These two crucial parameters will be discussed in the section 2.5.1 and section 2.5.2, respectively.

2.5.1 Position Calibration

Due to the separation of the sensing coils, the actual measured position is within a proximity of the 3 sensing coils. Besides, there is accumulative error associated with the numerical formulation of equation (2-8) and tolerance of RMS-DC converter. Therefore the measured position is often deviated from the actuator's position. Figure 2-20 depicts this deviation between true and measured locations of 8 points forming a cuboid spanning the display area. The cuboid formed by the measured coordinates is distorted and offset to its real shape.

In order to adjust the measured position to the actuator's position, we apply a calibration method based on shape function correlating the 3D natural to Cartesian coordinates frames used in Finite Element Analysis (FEA) [31]. In brief, a set of boundary points in both the natural (measured) and Cartesian (true) coordinates are obtained. And then a set of shape functions (in form of matrix) are calculated to adjust the measurement.

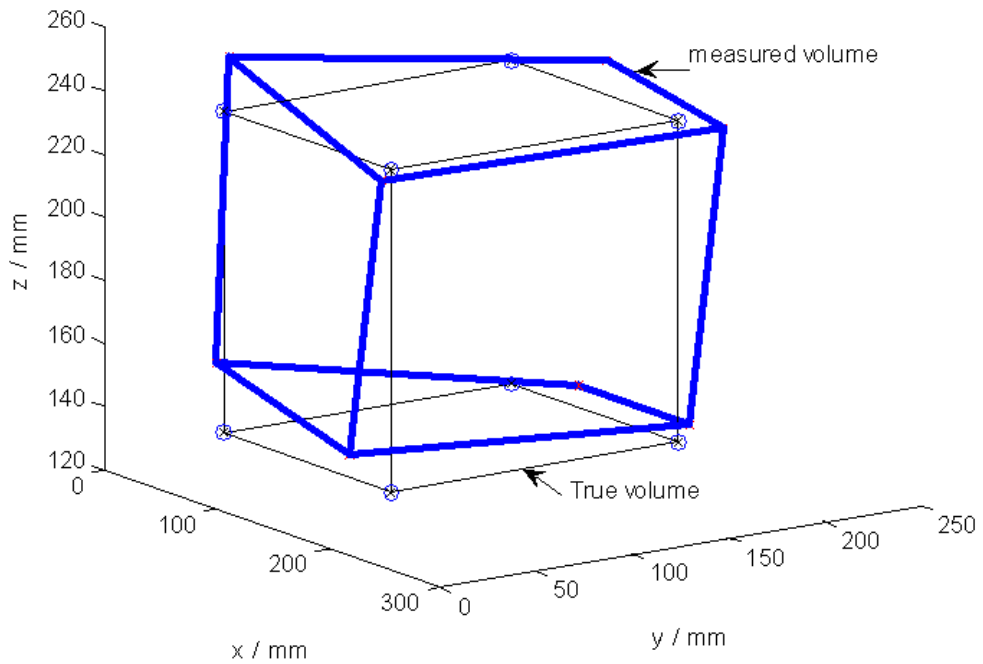


Fig. 2-20 Distortion caused by position measurement error.

Specific for a 3D cuboid area, eight corner points' coordinates are measured and compared with their true positions. A calibration matrix is then formed by equalizing all 8 results between each coordinate system. For any measurement inside the area defined by 8 boundary points, we calibrate the result by multiplying the computed calibration matrix. This calibration matrix is calculated by the process described in equation (2-23) below.

$$\begin{bmatrix} x_1 & x_2 & \dots & x_8 \\ y_1 & y_2 & \dots & y_8 \\ z_1 & z_2 & \dots & z_8 \end{bmatrix} = A_0 \begin{bmatrix} \xi_1 & \xi_2 & \dots & \xi_8 \\ \eta_1 & \eta_2 & \dots & \eta_8 \\ \varsigma_1 & \varsigma_2 & \dots & \varsigma_8 \\ \xi_1\eta_1 & \xi_2\eta_2 & \dots & \xi_8\eta_8 \\ \xi_1\varsigma_1 & \xi_2\varsigma_2 & \dots & \xi_8\varsigma_8 \\ \eta_1\varsigma_1 & \eta_2\varsigma_2 & \dots & \eta_8\varsigma_8 \\ \xi_1\eta_1\varsigma_1 & \xi_2\eta_2\varsigma_2 & \dots & \xi_8\eta_8\varsigma_8 \\ 1 & 1 & \dots & 1 \end{bmatrix}, \quad (2-23)$$

where $[x_i, y_i, z_i]$ ($i=1,2,\dots,8$) are the true position vectors and $[\xi_i, \eta_i, \varsigma_i]$ are the measured position vectors for the i^{th} corner of the cuboid; A_0 is the calibration matrix to bridge the two sets of results. Equation (2-23) yields a unique solution for A_0 , formed as a 3 by 8 matrix. Note that the information of shape function is stored in measured coordinates. Each column of the measurement matrix on the right hand side of equation contains all the first order terms and their cross products of the components for each measured position.

Knowing A_0 , any measured position can be calibrated by

$$\begin{bmatrix} x \\ y \\ z \end{bmatrix} = A_0 \begin{bmatrix} \xi \\ \eta \\ \varsigma \\ \xi\eta \\ \xi\varsigma \\ \eta\varsigma \\ \xi\eta\varsigma \\ 1 \end{bmatrix}, \quad (2-24)$$

If we divide the display area into multiple such calibration boxes within which position measurement is adjusted, we can theoretically create a large area of accurate localization. In current application, we split the shape display area into 8 small cuboids of $5 \text{ cm} \times 5 \text{ cm} \times 3.5 \text{ cm}$ size (as shown in Figure 2-21). In order to verify the accuracy of the position measurements, we select 9 points and compare the measured results with their known true positions. The error bound of 2 mm is found within the testing range, which defines the resolution of the shape to be displayed. The position measurement results are shown in Figure 2-22.

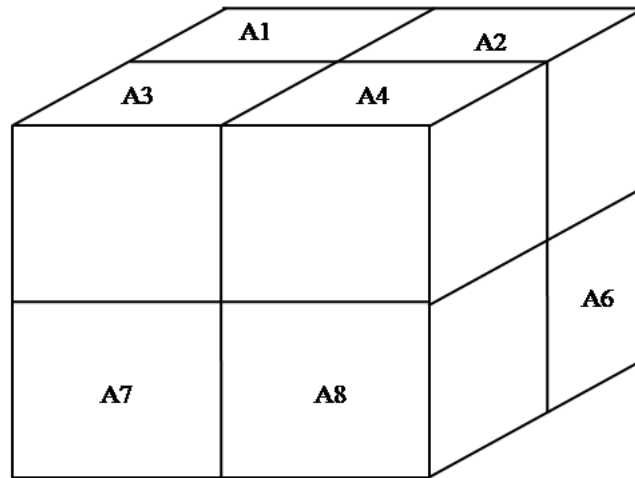


Fig. 2-22 The working space is divided into 8 small cuboids for position calibration.

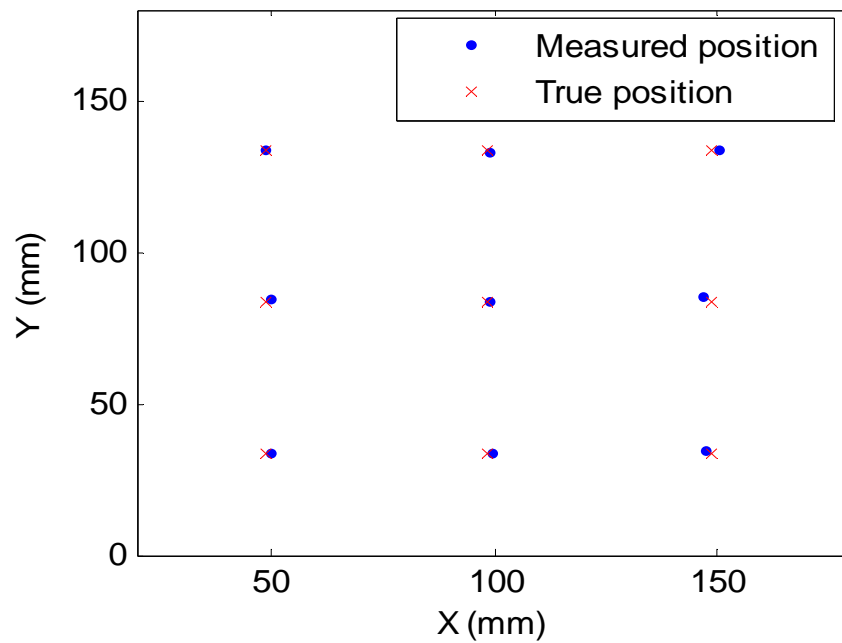


Fig. 2-21 Position measurement results within display area where $Z=166$ mm.

2.5.2 Time-budget Design

The refresh rate of the position detection is essential for operator's scanning speed. User's free scanning speed is measured to be around 100 mm/s. The position measurement is desired to be updated for every resolution distance i.e. 2 mm. Therefore, based on 100 mm/s scanning speed, the ideal position refresh rate should be higher than 50 s^{-1} . The time-budget design of the system is shown in Figure 2-23. PC and microcontroller formulate 2 parallel processing sequences which are synchronized through the interrupt that carries the actuation frequency command created by PC. In each cycle, PC calculates the position of the previous step while waiting for the microcontroller to deliver the data of the current step. The consequent time consumption for each cycle is then mainly decided by position computation, which is varied between 8-15 ms.

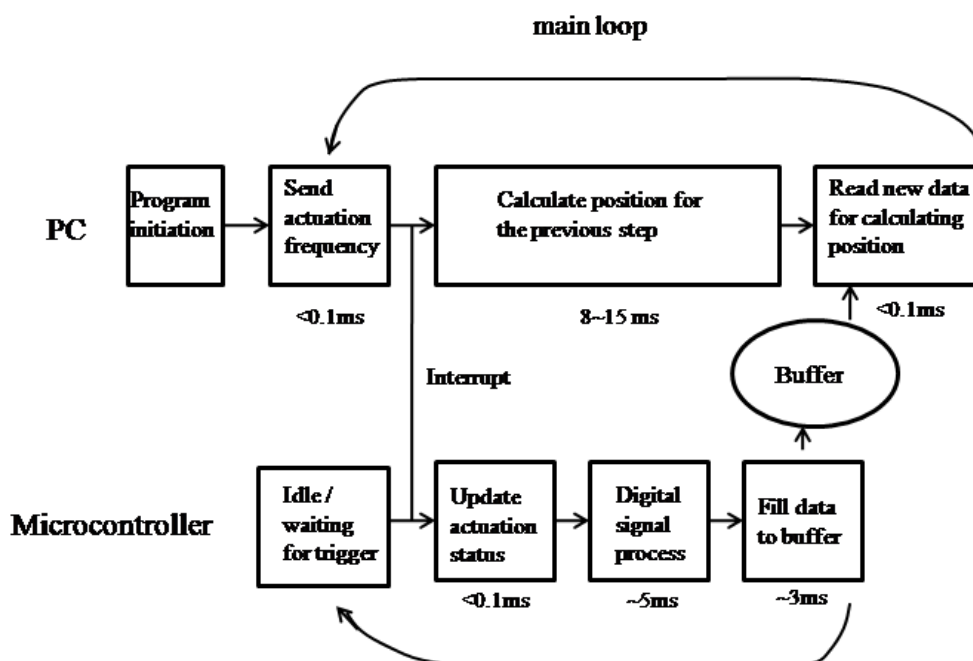


Fig. 2-23 Parallel timing design for PC and microcontroller.

The measured computing time for each PC cycle is shown in Figure 2-24, which gives an average of 10.9 ms/cycle for 1000 measurements. This period is correspondent to a refresh rate of 91 s^{-1} , which is sufficient for the proposed tactile display based on above analysis.

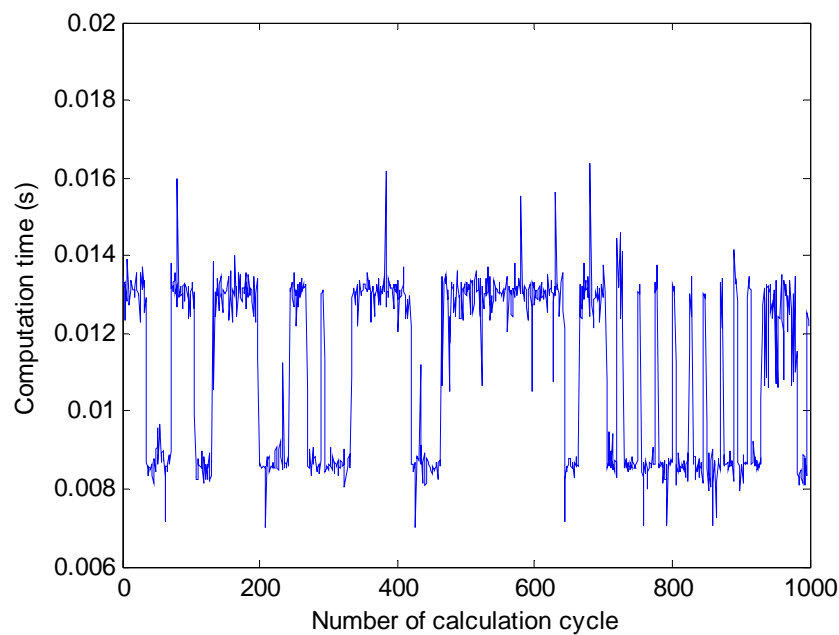


Fig. 2-24 Measured computation time per cycle.

An intuitive experiment is also performed by recording the positions of the scanning paths. Figure 2-25 shows the operator's handwriting of two words using one's normal scanning speed. The corresponding sampling rate appears to be sufficient to follow user's movement. The detailed MATLAB code and ASSEMBLY code for implementing such timing design is shown in Appendix B and Appendix C, respectively.

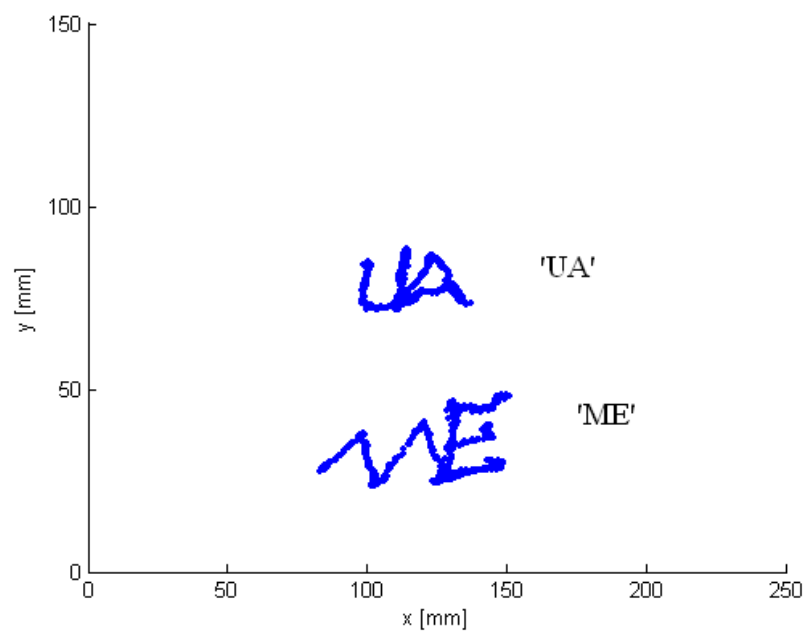


Fig. 2-25 Display of data sampling rate over users scanning rate.

3. DESIGN OF ELECTROMAGNETIC ACTUATOR

Many types of the vibrotactile actuation have been exploited. However, the widely used actuators that meet both the relative large perceivable stroke and vibration bandwidth are mainly based on piezoelectric and EM actuation [15]. Although piezoelectric actuator is fast responding and available in market with reasonable price [33], it usually requires bulky stack arrangement or high voltage supply / high power amplifier [34-36] in order to produce a perceivable displacement. Comparatively, EM actuation is safer and easier to be driven by a miniature coil. In the following sections, eddy-current based (section 3.1) and permanent magnet based (section 3.2) EM actuation will be described respectively. Due to its applicable actuator force range to produce perceivable stimulation, permanent magnet based actuation is used in our device. Section 3.2 describes the detailed design of the actuator including the analysis and measurements of the force characteristics; section 3.3 provides a vibration test for perception limit study under different actuation frequency.

3.1 Concept I: Eddy Current Actuator Method

Mechanical impulses generated from eddy current mechanism are widely used in aerodynamic surface to remove the ice [36]. Two coaxial current loops shown in Figure 3-1 produce repulsive force to each other when their current directions are opposite.

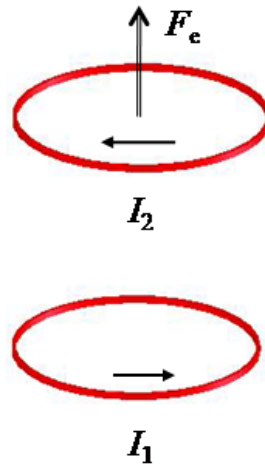


Fig. 3-1 Repulsive force generated from 2 current filaments.

The reaction force between the two coaxial current units can be described as [38]

$$F_e = -I_1 I_2 \frac{dM_{12}}{dz}, \quad (3-1)$$

where I_1 , I_2 and M_{12} are the current of each circuit and mutual inductance between the two current loops respectively; $\frac{dM_{12}}{dz}$ represents the gradient of the mutual inductance along their axis direction. For infinitely thin filaments, their mutual inductance is [38]

$$M_{12} = 2\mu_0 \sqrt{\frac{r_1 r_2}{m}} \left[\left(1 - \frac{m}{2}\right) K(m) - E(m) \right], \quad (3-2)$$

$$m = \frac{4r_1 r_2}{(r_1 + r_2)^2 + z^2}$$

where r_1 and r_2 is the radius of the each coil, and z is the distance between their centers; K and E are the complete elliptic integral of the first and second kind respectively. Using the relations of

$$\frac{dE(m)}{dm} = \frac{E(m) - K(m)}{m}$$

$$\frac{dK(m)}{dm} = \frac{E(m)}{m(1-m^2)} - \frac{K(m)}{m}$$

the expression of the gradient of mutual inductance along z direction can be derived into

$$\frac{dM_{12}}{dz} = -\frac{\mu_0}{4} \sqrt{\frac{r_1}{r_2}} \frac{\sqrt{m}}{1-m} [(2-m)E(m) + (2m-2)K(m)] \quad (3-3)$$

Combining equations (3-1) and (3-3), we can get the force expression for one pair of filaments. For any solenoid that contains multiple such filaments, their reaction force can be calculated by a numerical summation of force between each pair. Practically, we divide cross section of coil into multiple small areas within which equation (3-1) and equation (3-3) are considered to be valid, which is shown in Figure 3-2. Therefore the overall mutual inductance of two solenoids can be computed as

$$\frac{dM_{12}}{dz} = -\frac{\mu_0}{4} \sum_{ij} \sqrt{\frac{r_{1i}}{r_{2j}}} \frac{\sqrt{m_{ij}}}{1-m_{ij}} [(2-m_{ij})E(m_{ij}) + (2m_{ij}-2)K(m_{ij})] \quad (3-4)$$

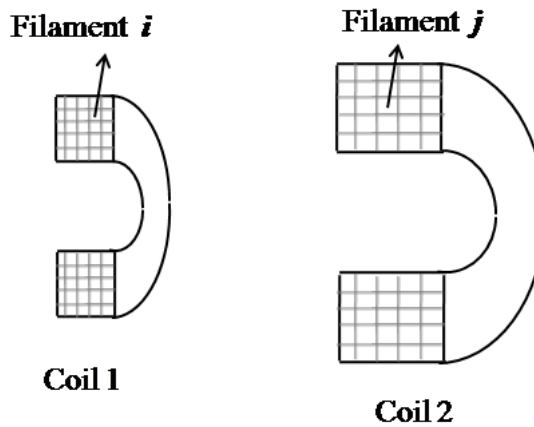


Fig. 3-2 Calculation model for two coils by dividing their cross sections.

An eddy current based actuator can be implemented by the electrical system shown in Figure 3-3. Voltage supply V_1 and capacitor C are used to provide periodic pulses to the coil L_1 which is in a fixed position. As the current I_1 flows through L_1 , an instant magnetic field is established such that armature coil L_a placed nearby generates eddy current I_a resulting in the repell force during the switching. The governing equations of this two coil system are

$$\begin{aligned} V_1 &= I_1 R_1 + \frac{d(I_a M)}{dt} + \frac{d(L_1 I_1)}{dt} + \frac{\int I_1 dt}{C} \\ 0 &= R_a I_a + \frac{d(I_1 M)}{dt} + \frac{d(L_a I_a)}{dt} \quad , \\ F &= m \frac{d^2 z}{dt^2} = -I_1 I_a \frac{dM}{dz} \end{aligned} \quad (3-5)$$

where the first two equations are Kirchoff laws for close loop voltage in each circuit including voltage drop on resistor, mutual inductive voltage, and the self inductive voltage; the third equation is the Newton's second law containing mutual magnetic force expressed by equation (3-1).

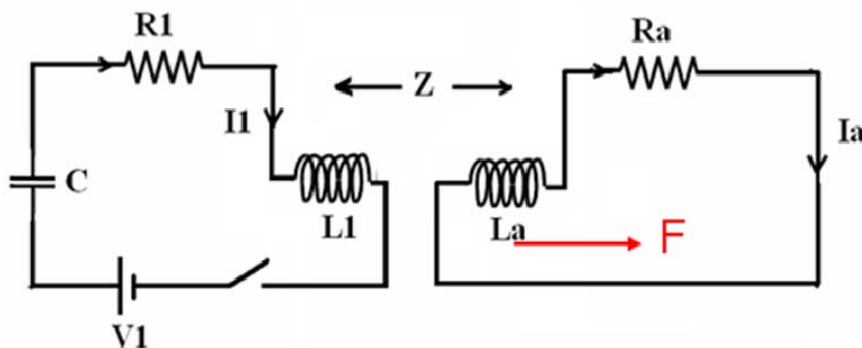


Fig. 3-3 Electrical system implementation for eddy current based EM actuation.

Equation (3-5) can be mathematically transformed into

$$\begin{aligned} V_1 &= I_1 R_1 + I_a \frac{dM}{dz} \frac{dz}{dt} + M \frac{dI_a}{dt} + L_1 \frac{dI_1}{dt} + \frac{\int I_1 dt}{C} \\ 0 &= R_a I_a + L_a \frac{dI_a}{dt} + M \frac{dI_1}{dt} + I_1 \frac{dM}{dz} \frac{dz}{dt} \quad , \\ F &= m \frac{d^2 z}{dt^2} = -I_1 I_a \frac{dM}{dz} \end{aligned} \quad (3-6)$$

where the terms of inductive voltage are splitted to the product of the mutual inductance gradient (dM/dz) and the armature's velocity (dz/dt).

In order to calculate the force and displacement determined by equation (3-6), we use MATLAB/SIMULINK to dynamically simulate this problem. Before the simulation, we firstly calculate coil's parameters including mutual inductance, self inductance and electrical resistance by using equation (3-4) based on coils' geometry and the wire's properties. Block diagram shown in Figure 3-4 describes the simulation scheme.

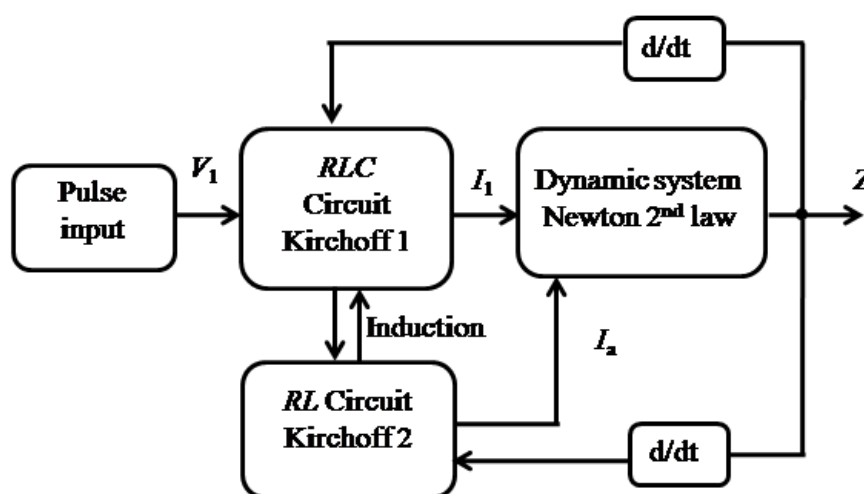


Fig. 3-4 Block diagram of the simulation process.

The entire system contains three subsystems: *RLC* circuit 1, *RL* circuit 2, and the dynamic system. The system's input is the pulse voltage to the driving circuit 1. The outputs of the two circuits subsystems, I_1 and I_a , are meanwhile the inputs to the dynamic subsystem. The output of the entire system is the position of the armature coil z , which is fed back to the two circuits subsystem to provide the momentary velocity state. The corresponding SIMULINK model is illustrated in Figure 3-5.

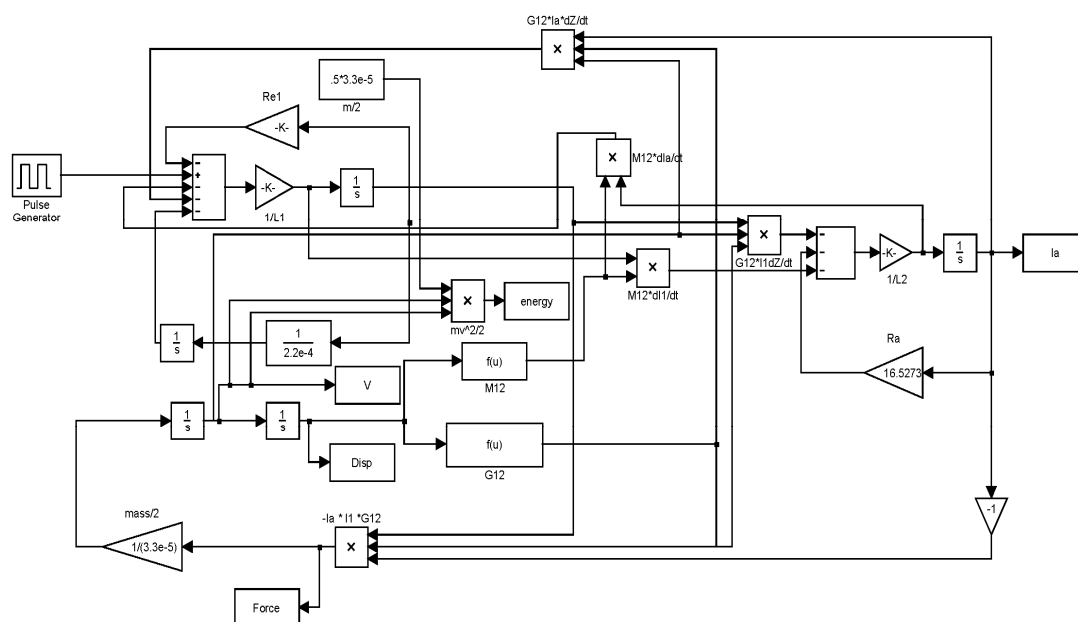


Fig. 3-5 SIMULINK model of the force simulation.

The simulated coils have the dimension described in Figure 3-6. The wire of the coil is AWG 44 with 50 μm cross section diameter. Mass and resistance is calculated from density and resistivity and the total circumference of the copper wire. Voltage pulse has 8 V amplitude and 100 Hz frequency. 100 μF capacitor is used for energy storage.

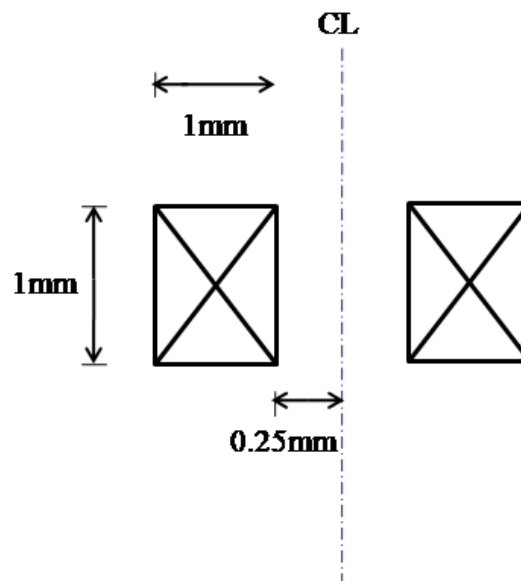


Fig. 3-6 Coil geometry used in simulation.

Figure 3-7 shows the simulation of the force and velocity of the armature coil due to one current pulse. Figure 3-8 shows the driving current I_1 and the inductive current I_a . According to Figure 3-7, a peak force of 1.9 mN can be obtained and the resulting velocity of the armature coil is 1 mm/s. Most of energy is consumed into current heat at the driving coil instead of the armature coil's kinetic energy. The main reason is that the inductive current (I_a) vanishes too quickly due to a very small time constant of the RL system (The time constant is L_a/R_a . For the coil with designed size, $L_a \sim 0.1$ mH and $R_a \sim 10 \Omega$, which results in $\sim 10 \mu\text{s}$ time constant for the inductive current I_a , as quantitatively shown in Figure 3-8). Within this short time, only a very small impulse can be applied to armature coil therefore the consequent velocity of the armature is negligibly small.

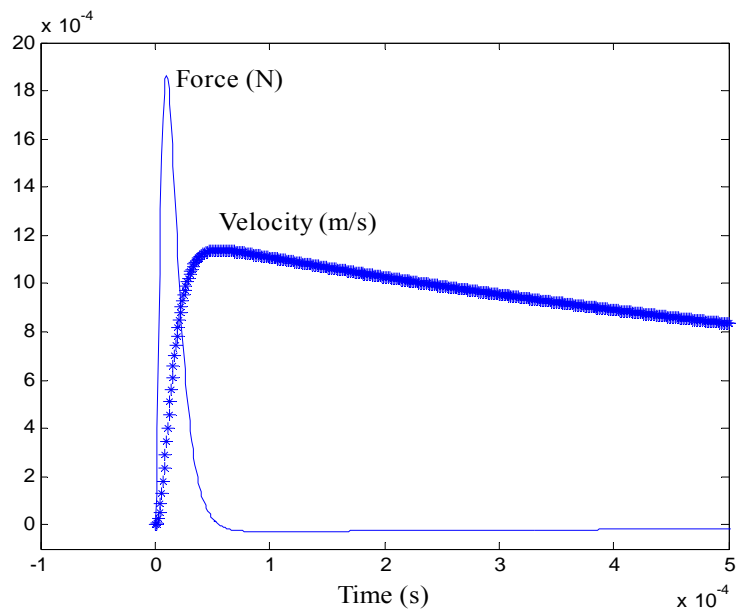


Fig. 3-7 Simulation results of force and velocity.

In order to increase the reaction impulse, one way is to increase the size of the coil by 10~100 times to yield a larger time constant which can be compared to vibrating period. This is not desired for the experiment in regard to miniature actuator. Another way is to use permanent magnet instead of armature coil, that allows a constant magnetization (infinite time constant) during the actuation. The next section will discuss the detailed actuator design by using a driving coil and permanent magnet.

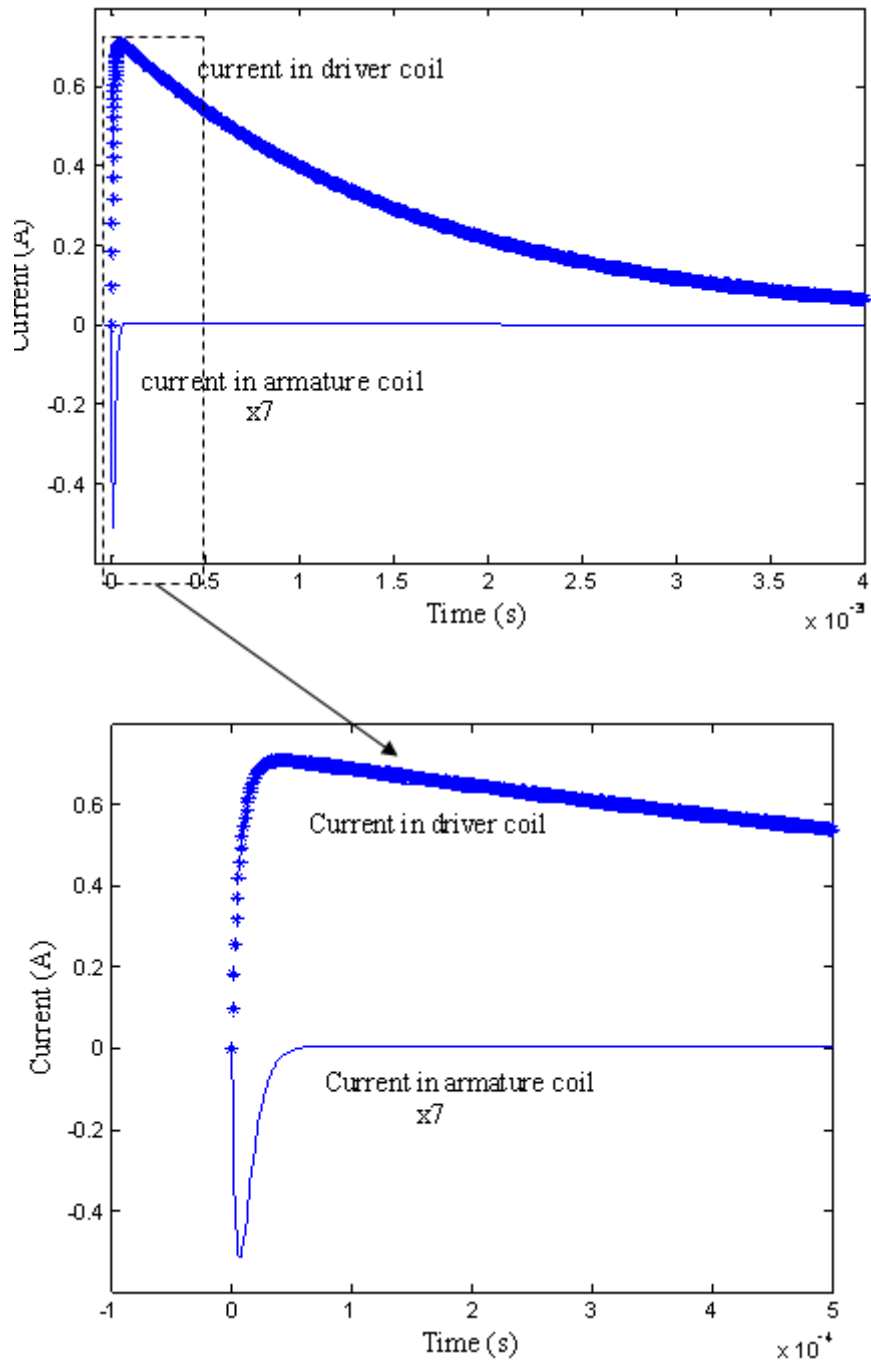


Fig. 3-8 Simulation results for driving current and armature current.

3.2 Concept II: Permanent Magnet Actuator Method

Figure 3-9 depicts the working principle and the mechanism of the permanent

magnet based EM actuator. Similar to eddy current mechanism, the current pulses are generated by a periodic discharge from the capacitor. We use a pair of switches to form a half bridge driving circuit such that the continuous current pulses are produced by periodically switching on and off the power supply to the capacitor connected in parallel. Accordingly, a magnetic field is established in opposite direction to the magnetization of the permanent magnet during half of the actuation cycle, which results in a rapid push of the permanent magnet.

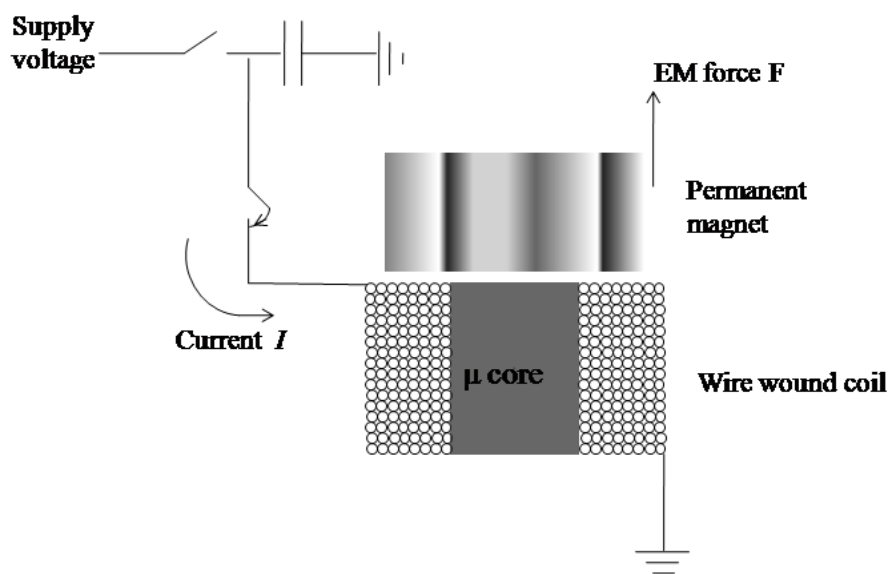


Fig. 3-9 Working principle of permanent magnet based EM actuation.

Based on Lorentz Law, the force obtained by the permanent magnet under an external magnetic field can be written as

$$\vec{F} = \int_S \vec{J}_{ms} \times \vec{B} dS, \quad (3-7)$$

where \vec{J}_{ms} is the density of the equivalent current source dimensioned as amp per unit length along the side surface, and \vec{B} is the external magnetic field flux density. The

equivalent current source model of a permanent magnet is shown in Figure 3-10.

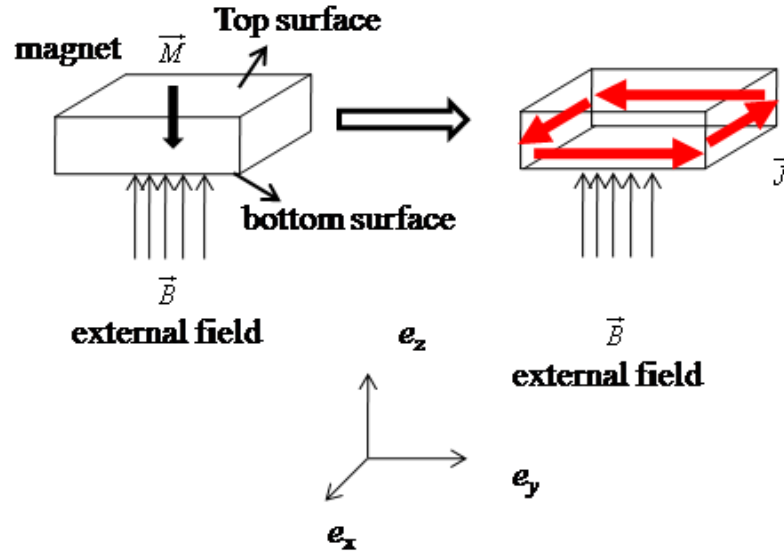


Fig. 3-10 Equivalent current source model of a permanent magnet.

The current source density has a general form of [39]

$$\vec{J}_{ms} = -\vec{n} \times \vec{M} / \mu_0, \quad (3-8)$$

where \vec{M} is the magnetization vector of the permanent magnet; \vec{n} is the unit normal vector of the surfaces of the magnet and μ_0 is the free space permeability.

Substitute equation (3-8) into (3-7), we get

$$\vec{F} = \int_s [(\vec{B} \cdot \vec{M})\vec{n} - (\vec{B} \cdot \vec{n})\vec{M}] / \mu_0. \quad (3-9)$$

Specific to the magnet where \vec{M} is along e_z direction, we can simplify equation (3-9) by performing the following derivation.

$$\begin{aligned}
\vec{F} &= \{-M[\int_{\text{side}} + \int_{\text{top}} + \int_{\text{bottom}}]B_z \vec{dS} - [M\hat{e}_z \oint (\vec{B} \cdot \vec{n})dS]\} / \mu_0 \\
&= \{-M[\int_{\text{side}} + \int_{\text{top}} + \int_{\text{bottom}}]B_z \vec{dS}\} / \mu_0 \\
&= \{-M[\int_{\text{top}} + \int_{\text{bottom}}]B_z \vec{dS}\} / \mu_0 \\
&= (\int_{\text{bottom}} B_z dS - \int_{\text{top}} B_z dS) / \mu_0 \hat{e}_z = M(\phi_{\text{bottom}} - \phi_{\text{top}}) / \mu_0 \hat{e}_z
\end{aligned} \tag{3-10}$$

where ϕ_{bottom} and ϕ_{top} are the flux caused by external magnetic field at the bottom and top surface of the permanent magnet respectively, and B_z is the e_z component of B .

Note that in derivation of equation (3-10), we have used Gauss law

$$\oint (\vec{B} \cdot \vec{n})dS = 0.$$

Equation (3-10) indicates that the desired actuator should contain a permanent magnet with high residual flux density (large M), meanwhile requires a solenoid providing a large flux difference between the bottom and top surfaces of the magnet. The latter condition can be achieved by using a high permeability magnetic core for the solenoid, which concentrates flux lines inside the coil and spread them quickly outside the coil.

The coil's geometric span is essential for the actuation force. To design the right size of the coil, we limit the outer radius to 1 mm to match the two point discrimination distance of human finger [1]. We vary the thickness t and inner radius r of the coil, illustrated in Figure 3-11.

Existence of the iron core forms a nonlinear relation between the force and coil's geometry. Therefore finite element software (ANSYS) was used to simulate the

magnetic force between permanent magnet and a solenoid driven by a 550 mA current, which is the designed peak value of the current pulse during the actuation. The residual flux density of the permanent magnet is 0.75 T and its coercive force is 5750 Oersteds. The magnet has $2\text{ mm} \times 2\text{ mm}$ surface and 1 mm thickness in its magnetization direction. The slope of its demagnetizing curve is assumed to be constant in the simulation. The wire-wound coil is substituted by an equivalent volume of current element, whose current density is determined by ratio of total applied current and cross section area of the wire-formed cylinder shell. The detailed ANSYS code of the force simulation is shown in Appendix D.

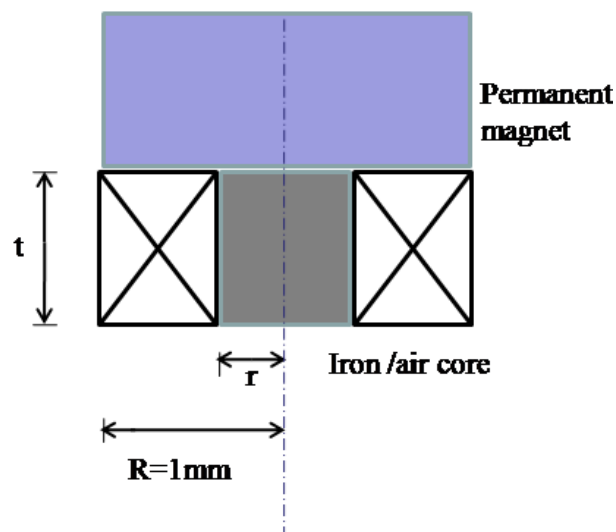
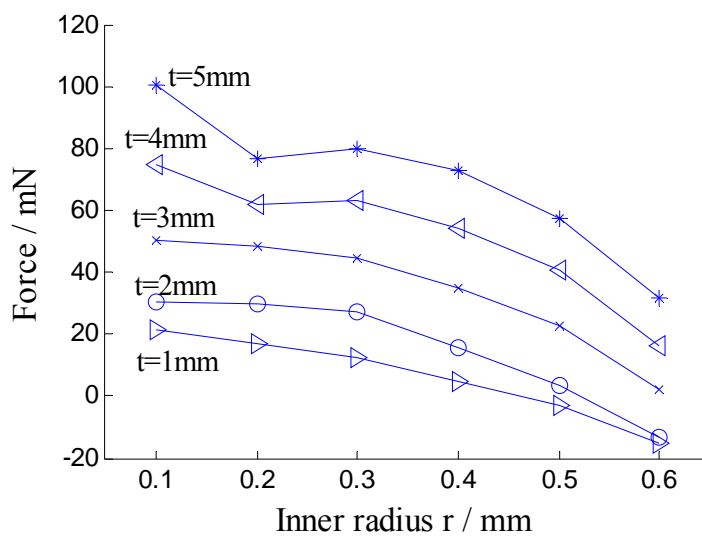


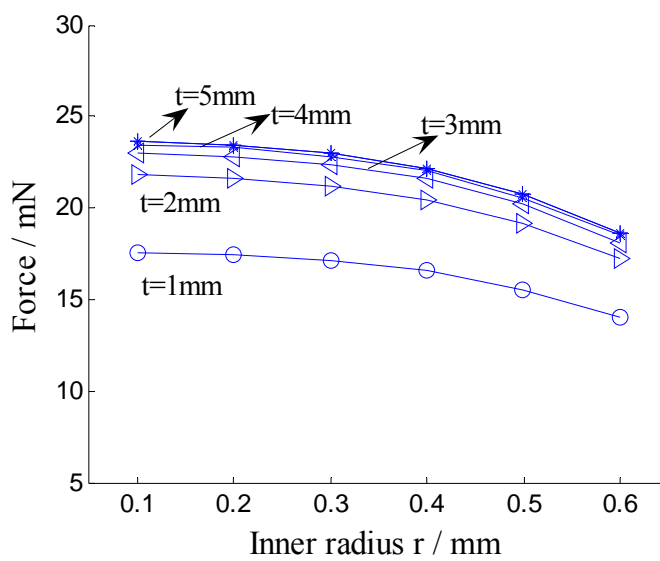
Fig. 3-11 Coil geometry parameter definition.

Figure 3-12 shows the simulation results. Figure 3-12(a) demonstrates a coil with an iron core with relative permeability of 200, while Figure 3-12(b) is the air core coil of the same dimension. With the help of the iron core, higher force can be achieved by increasing the coil's thickness, shown in Figure 3-12(a). Maximal thickness of 5 mm

is considered as a proper size of the miniature actuator. Small inner radius is desired, meaning more turns of solenoid and less initial attractive force between the magnet and the core. The limitation, however, lies in the reduction of Q factor of the coil when the inner radius of the coil decreases. The inner part of the wires contributes to the electrical resistance more than the magnetic force. A convenient selection of inner radius is 0.4 mm (5/32 inch) which is suitable for a proper resistance and the fabrication availability.



(a)



(b)

Fig. 3-12 Force simulation based on coil's geometry.

Table 3-1 shows the actuator's parameters.

The coil is made by the winding machine shown in Figure 3-13. In order to determine the force-current characteristic, we used a digital scale to record the force and used multimeter to measure the corresponding input current. Meanwhile, we

measured the magnetic field flux density at the positions of the permanent magnet's top and bottom surfaces under various input current, and obtained a calculated force-current characteristic to see if this agree with the experimental result. Specifically, the coil's resistance and inductance were measured by using Gamry PCI4 Impedance Analyzer. The flux density at centers of the bottom (B_{bottom}) and top (B_{top}) surfaces of the magnet were measured by using Alphalab DC Magnetometer.

TABLE 3-1
PARAMETERS OF ACTUATOR

Parameters	Values
inner radius	0.4 mm
outer radius	1 mm
wire diameter	0.05 mm
winding turns	430
coil length	5 mm
side length of magnet	2 mm
thickness of magnet	1 mm
residual flux density	0.75 T
coil resistance	15 Ω



Fig. 3-13 Winding machine for coil's fabrication.

B_{bottom} and B_{top} are linear functions of the applied current, as shown in Figure 3-14.

The flux difference of the two surfaces is approximately equal to

$$\phi_{\text{bottom}} - \phi_{\text{top}} \approx A(B_{\text{bottom}} - B_{\text{top}}), \quad (3-11)$$

where A is the top / bottom surface area of the permanent magnet. The force-current characteristic can be calculated by equations (3-10), (3-11) and the B - I relation shown in Figure 3-14, which is

$$\left. \frac{dF}{dI} \right|_{\text{calculated}} = 0.2515 \text{ (mN/mA)}.$$

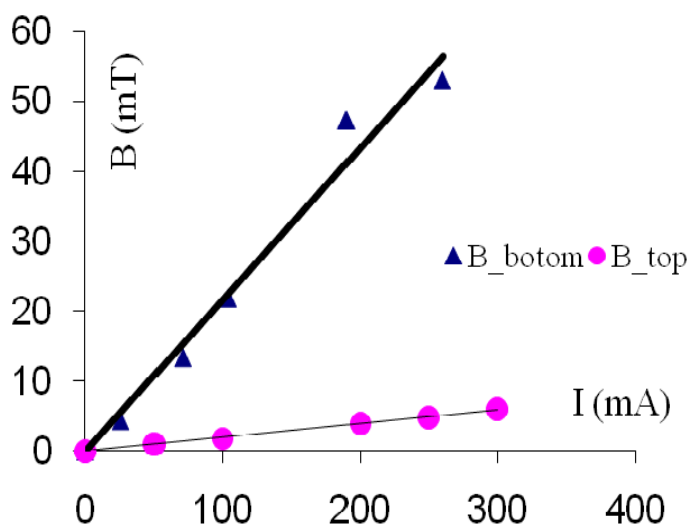


Fig. 3-14 Measured flux density at bottom and top surface of the magnet.

Figure 3-15 shows the experiment setup for measuring the static driving force under DC. The permanent magnet is attached to the digital scale, while the solenoid is fixed onto nonmagnetic material. Varied DC is applied through coil, and recorded by the multimeter.

Figure 3-16 shows the measured EM force versus current, for both the air core and

the identical iron core coil, the linear fitting slope of the force measurement is

$$\left. \frac{dF}{dI} \right|_{\text{measured}} = 0.2353 \text{ (mN/mA)}. \quad (3-12)$$

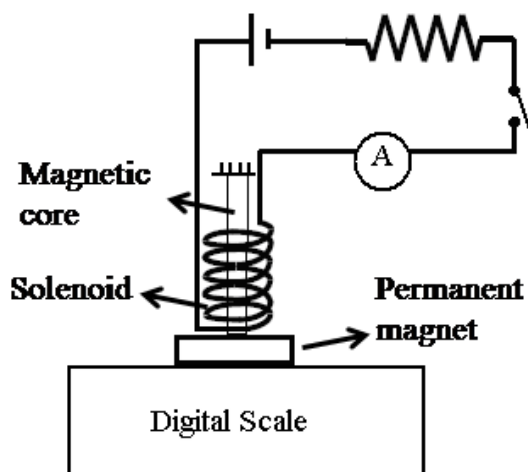


Fig. 3-16 Experiment setup for measuring magnetic force.

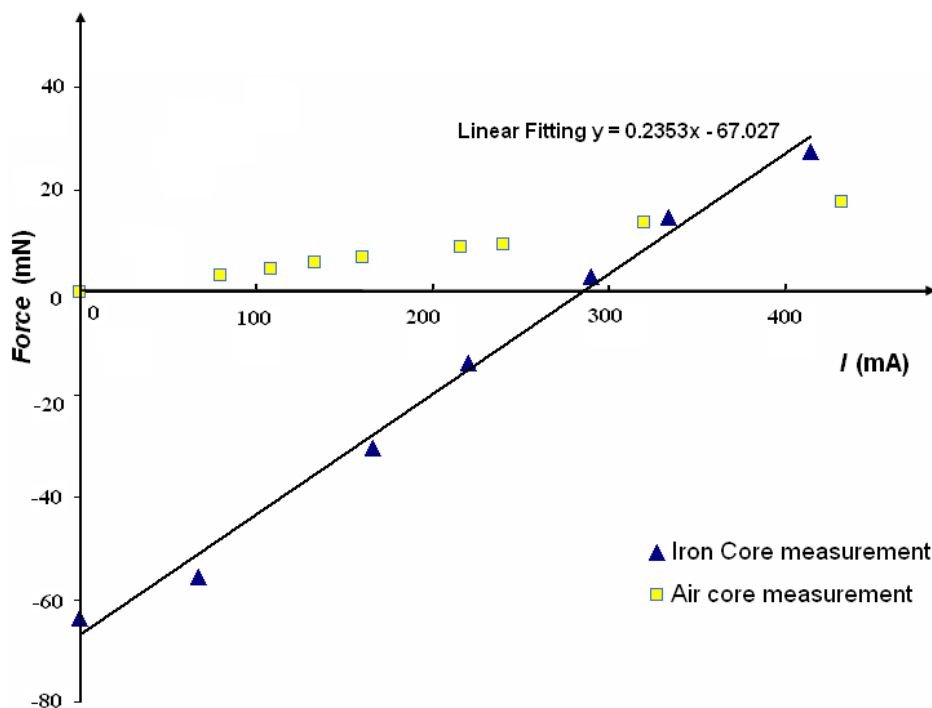


Fig. 3-15 Measured force characteristics versus input current.

Therefore the measured force-current relation agrees well with the calculation. Although there is an initial attractive force between the iron core and the magnet, the larger force can be obtained when the input current is higher than 350 mA.

3.3 Perception Limit of Vibratory Stimulation

Knowing the static force characteristic of the actuation, it is critical to test the perception of the vibratory stimulation and provide a basis for frequency perception preference and the minimum supply voltage. Figure 3-17 shows the experiment setup of the vibration stimulation test. Microcontroller and field effect transistor (FET) switch drivers supply a square wave signal to drive a half bridge switch pair. P metal oxide semiconductor (MOS) and NMOS switches perform a periodic charge and discharge to the capacitor by switching on and off the power supply. The supply voltage has adjusting range of 0-28V. During the discharge cycle of the capacitor, the actuator is engaged.

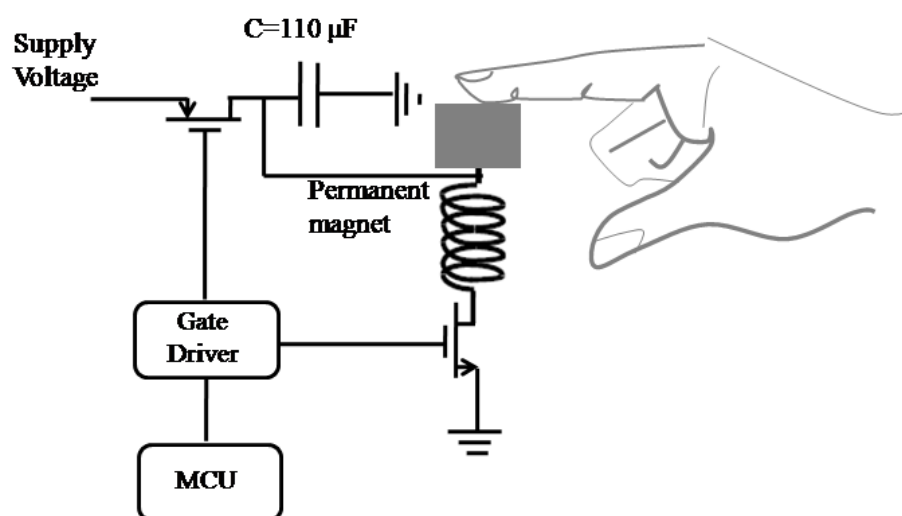


Fig. 3-17 Experiment setup for vibration stimulation test.

The charging and discharging curve of the capacitor are exponential function of time, which is schematically shown in Figure 3-18.

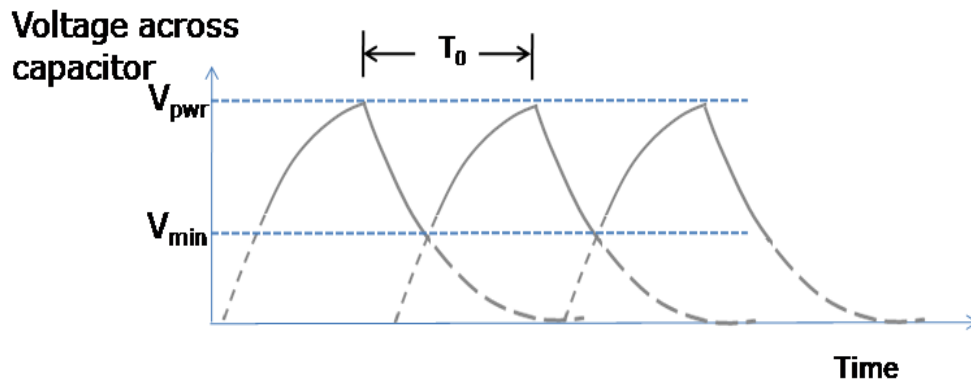


Fig. 3-18 Schematic illustration of the charging/discharging curve of the capacitor.

The actual energy delivered from capacitor is a function of the vibration frequency, which can be written as

$$E = \frac{1}{2} C (V_{\text{pwr}}^2 - V_{\text{min}}^2), \quad (3-13)$$

where

$$V_{\text{min}} = V_{\text{pwr}} e^{-\frac{T_0}{2\tau}}, \quad (3-14)$$

$$\tau = RC$$

Substitute equation (3-14) into (3-13),

$$E = \frac{1}{2} C V_{\text{pwr}}^2 (1 - e^{-\frac{1}{fRC}}), \quad (3-15)$$

where f is the vibration frequency. Substitute coil's parameters $R=16.2 \Omega$ and $C=115 \mu\text{F}$, we can plot the percentage of the delivered energy versus vibration frequency which is shown in Figure 3-19.

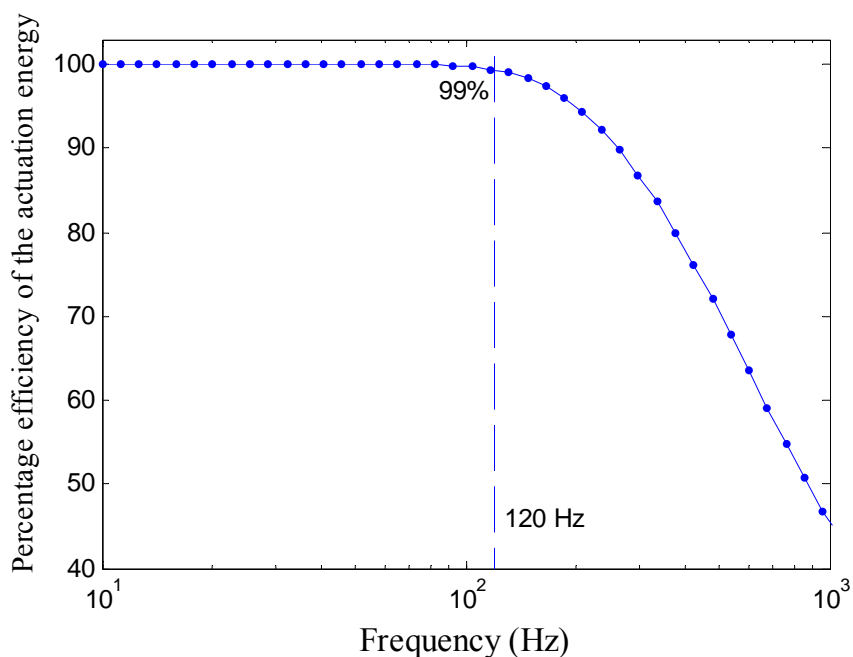


Fig. 3-19 Frequency response of the actuation energy efficiency.

According to Figure 3-19, 99% cutoff frequency of the actuation is 120 Hz. In order to compare the frequency dependence of the perception, we tested 10, 50, 80, and 120 Hz four frequency to 3 testers by slowly increasing the supply voltage. The threshold voltage at which the users perceive the continuous vibration was recorded. The corresponding peak current and pulse energy was also calculated and compared, as shown in Table 3-2.

The perception result shown in Figure 3-20 is compared with frequency response of the mechanoreceptor provided by [40]. The result indicates that Meissner corpuscle is the major mechanoreceptor for this type of vibration stimulation.

TABLE 3-2
VIBRATION TEST RESULTS

Tester	Data	Frequency (Hz)			
		10	50	80	120
1	voltage at perception (V)	7.9	8	8.6	9.3
	peak current (mA)	488	494	531	574
	peak force (mN)	50.1	51.6	60.4	70.8
	pulse energy (mJ)	3.6	3.7	4.3	5
2	voltage at perception (V)	8.3	8.2	8.5	8.8
	peak current (mA)	512	506	525	543
	peak force (mN)	55.9	54.4	59	63.3
	pulse energy (mJ)	4.0	3.9	4.2	4.5
3	voltage at perception (V)	8.6	8.4	8.6	9.2
	peak current (mA)	531	519	531	568
	peak force (mN)	60.4	57.6	60.4	69.3
	pulse energy (mJ)	4.3	4.1	4.3	4.9

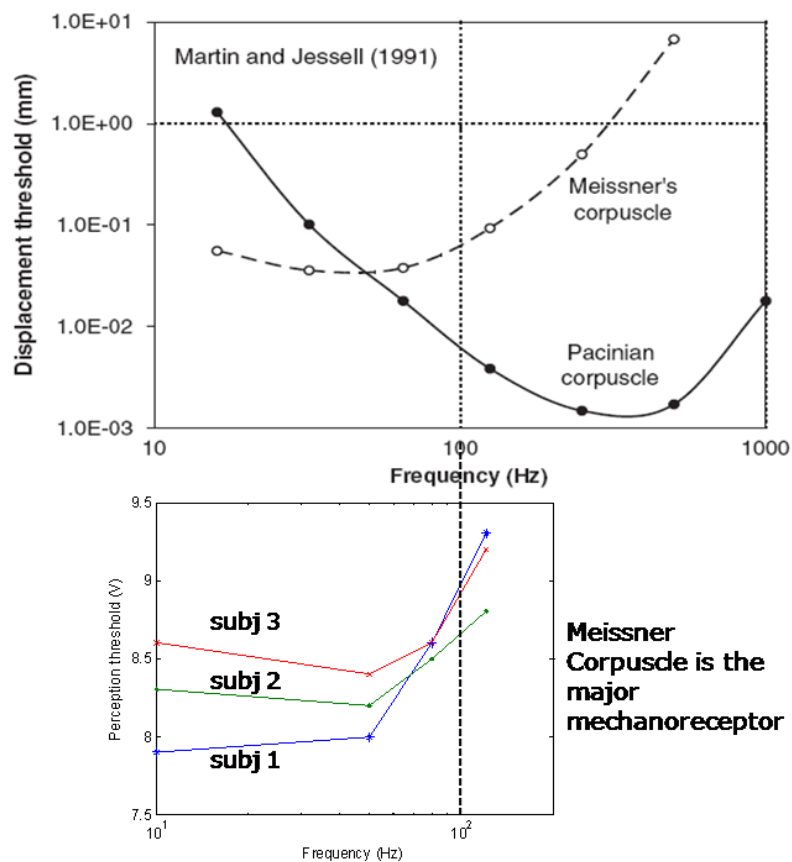


Fig. 3-20 Frequency preference of the perception threshold.

4. SYSTEM INTEGRATION

The position sensors can be combined with the EM actuator by using a nonmagnetic and nonconductive holder. Since the actuator works at much lower frequency (0-120 Hz) than the position sensors (125 kHz), the signal interference between each other can be eliminated by analog filter. To further reduce the interference caused by actuator's iron core and the permanent magnet, the actuator may be placed around the symmetrical center of the three position sensors.

4.1 Device structure and Experiment Setup

The schematic illustration of the integrated system is shown in Figure 4-1. The three position sensor modules, each containing a high sensitivity solenoid and a developed signal processing circuit board, are mounted perpendicularly on the sides of the plastic holder. An EM actuator containing a permanent magnet and a driving coil is inserted into center of the holder. The permanent magnet is attached to a thin plastic film to hold the vibration. The two small cylinders besides the magnet are used to support the fingertip in order to prevent from pressing the magnet too tightly, thus allowing a less resistance of the vibration. The sensors' outputs are connected to the analog to digital converter (ADC) and are later on directed to the microcontroller for signal processing. The photograph of the device and the experiment environment are shown in Figure 4-2.

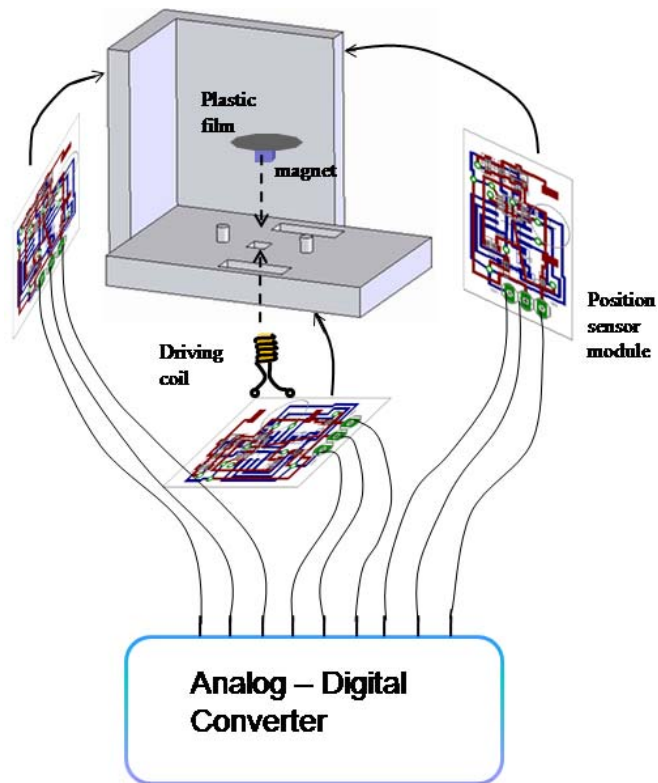


Fig. 4-2 Schematic illustration of the device structure.

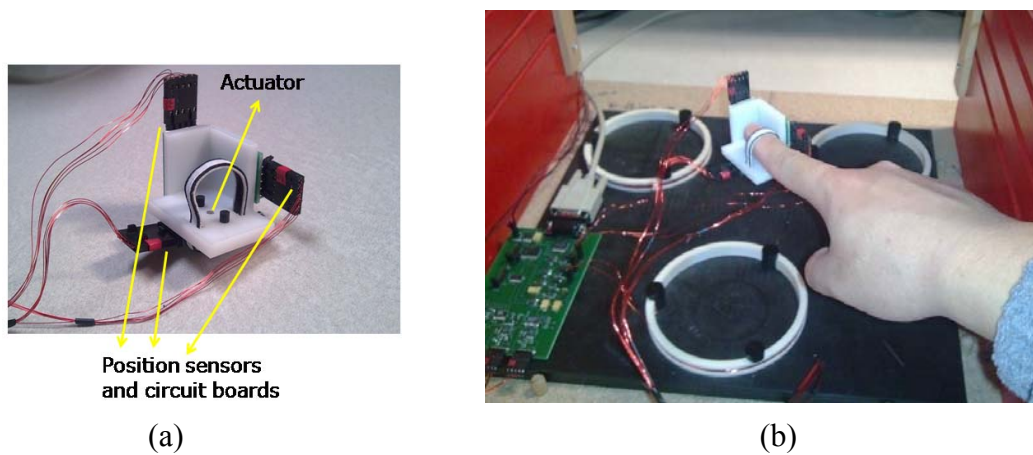


Fig. 4-1 (a) Photograph of the device and (b) tactile display space spatially defined by 3 beacon coils, and the master circuit board for signal transmission.

4.2 Heat Sink Design

The joule heat can be generated due to the switching current passing through the coil. The time domain electrical current activated by each pulse starts from peak value and decays exponentially over time. This results in a large average current when the switching frequency rises. Therefore it is necessary to determine the actual steady state temperature for each vibration frequency to consider operator's comfortability and safety. The variation of power density of the coil over switching frequency under 12 V supply voltage is shown in Figure 4-3.

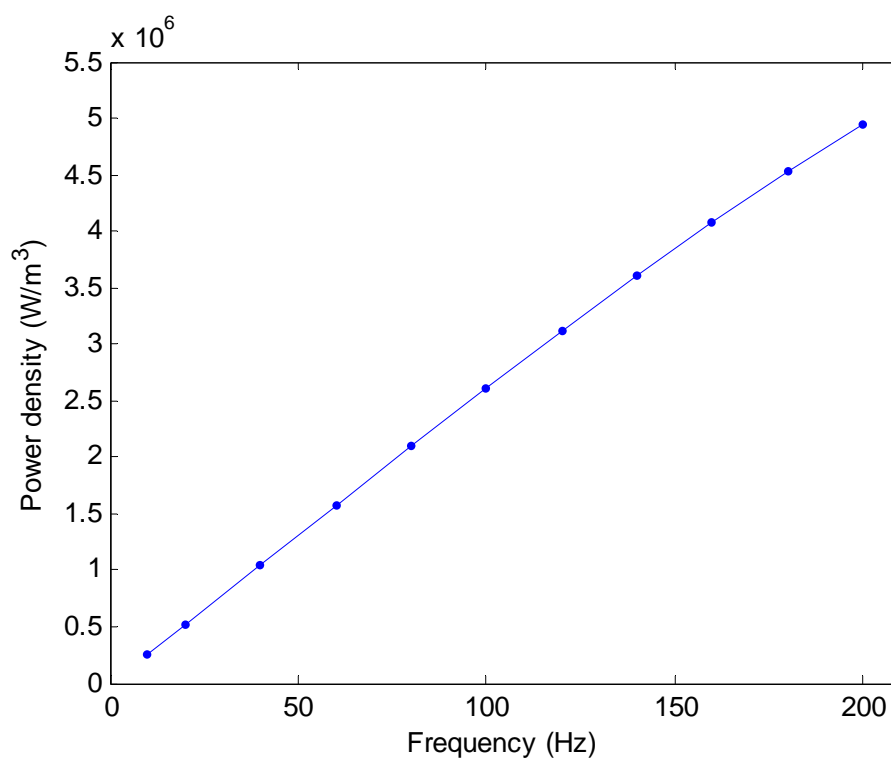


Fig. 4-3 Power density as a function of vibration frequency.

The power density is linearly proportional to the switching frequency for a fixed supply voltage. We previously mentioned that the actual supply voltage will decrease at high frequency due to device's bandwidth. As a result, the power density slightly

decreases its slope at high frequency, as shown in Figure 4-3. In order to compute the steady state temperature of the coil, Finite Element Heat Transfer (FEHT) is used to simulate the problem described by Figure 4-4.

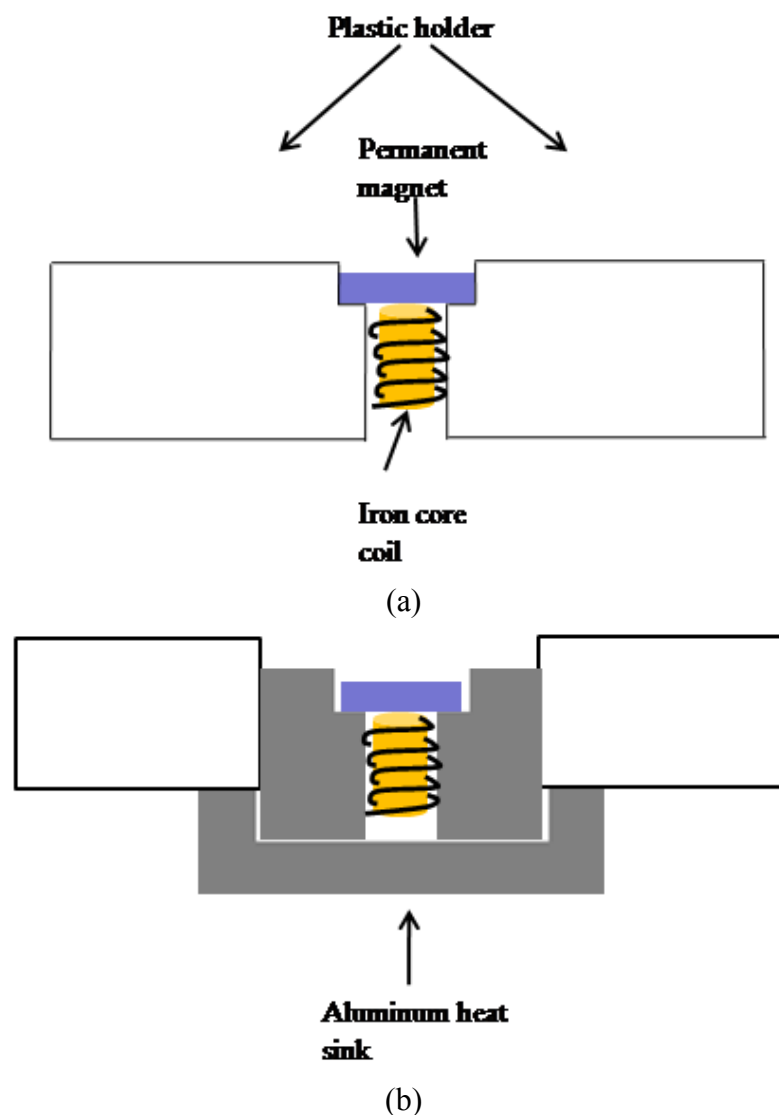


Fig. 4-4 Simulation structure of (a) actuator attached to holder and (b) actuator attached to heat sink.

Figure 4-4(a) shows the original design where the coil is directly attached to the plastic holder. Later experiments suggested that the coil was overheated when operator started to feel hot within perception duration. Figure 4-4(b) shows the

revised structure where the coil is attached to an aluminum block for heat dissipation.

The steady state temperature simulated by FEHT is shown in Figure 4-5.

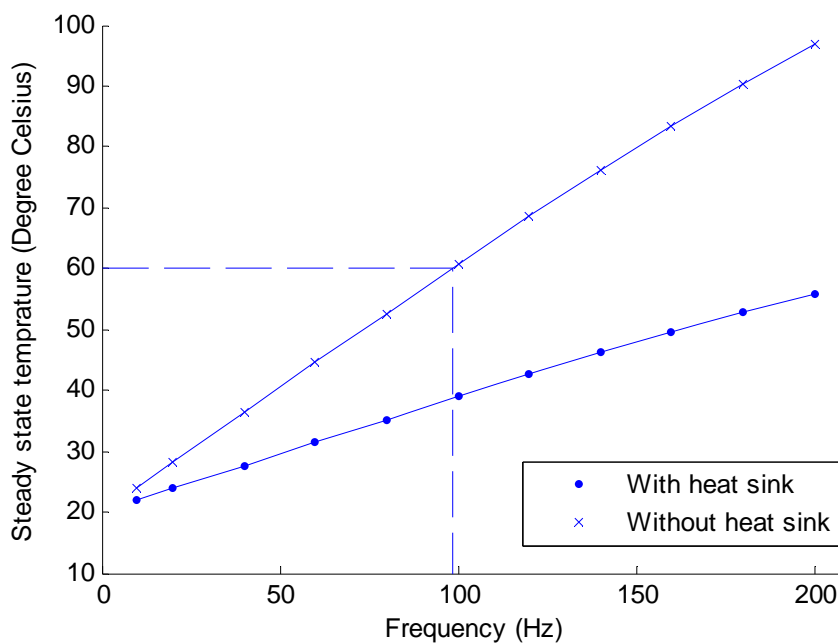


Fig. 4-5 Steady state temperature of the device with and without heat sink.

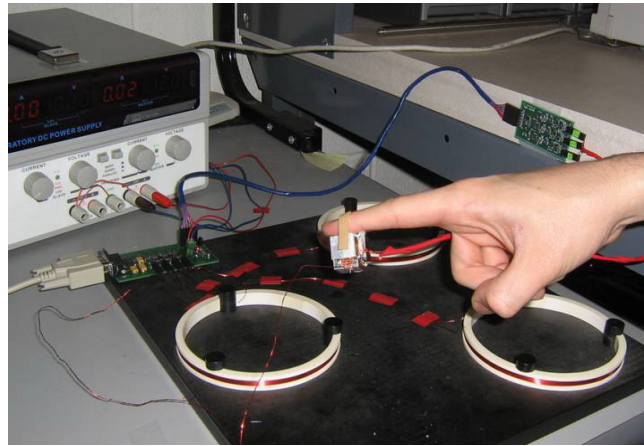
Without heat sink, the frequency needs to be limited at 98 Hz for a safety temperature of 60 °C. With the help of heat sink, the actuator's safety frequency range is increased about twice. As discussed in Chapter 3, the actuator's vibration frequency is limited below 120 Hz. In this frequency range, the steady state temperature is no more than 40 °C, which is a safe temperature for users.

5. EVALUATION

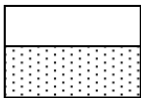
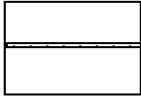
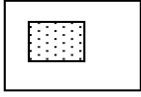
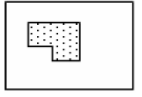
5.1 Shape Perception Test

In order to evaluate the effectiveness of the shape delivery, 3 volunteers participated in the experiment after providing consent to a protocol approved by the University of Arizona's Human Subjects Protection Committee. The volunteers are sighted, between 20-30 years old. Two of them are male and one is female. The subjects were able to see their hands but the displayed shapes were not disclosed except that the shapes were three dimensional.

The shapes test shown in Figure 5-1 is the preliminary test by using the first generation of the device which is depicted in Figure 5-1(a). We used aluminum block to accommodate 3 sensing coils and the actuator, which later on indicated a relatively large eddy noise appeared in the position measurement. The actuator had only one vibration frequency which was around 20 Hz. Figure 5-1(b) shows the results perceived by 2 testers. Although the early stage device had a limited display area and slow refresh rate, the relatively simple shapes were able to be perceived by the subjects. Except the incorrect corner perception of the cuboid by user 2, majority of the shapes were perceived correctly.



(a)

Virtual shape description	Perception		
	Subject 1	Subject 2	
$Z < Z_0$		Correct perception	Correct perception
$\Delta Z = 5\text{mm}$		Correct perception	Correct perception
40mm × 20mm × 30mm			Correct perception
	 static areas	 actuation areas	

(b)

Fig. 5-1 (a) Photograph of the device setup (b) Shape test set 1 from 2 volunteers [41].

By using the current version device (described previously in Figure 4-2), we developed a set of more complex 3D shapes which are shown in Figure 5-2. Except user 2 interpreted wrongly the continuous thin plates for shape (a) and (b), majority of the shapes are perceived correctly. Note that we retested the cuboid shape in order to compare the result with the early stage device. All 3 users correctly perceived this shape within 1 minute, which proves a substantial improvement to the previous version of device. The failure of thin plate perception from user 2, however, revealed that user may unnoticeably move away from one's scan path, which makes discrete thin surfaces more difficult to capture.

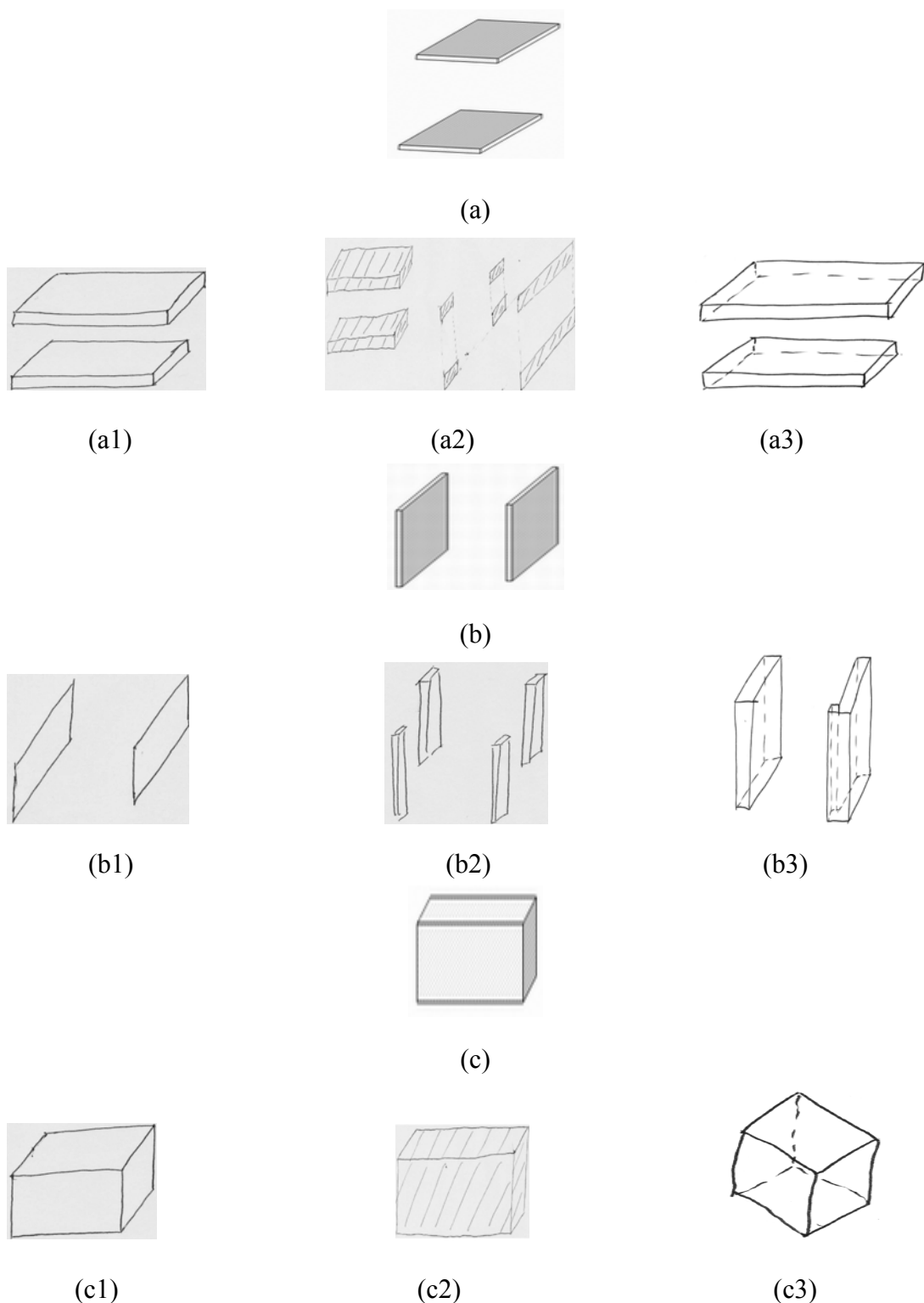


Fig. 5-2 Shape test set 2 (a) 2 horizontal plates with 6 mm thickness and 50 mm separation; (b) 2 vertical plates with 10 mm thickness and 50 mm separation; (c) cube of 70 mm side length; (a1 a2 a3, b1 b2 b3 and c1 c2 c3) are correspondent perceived shapes drawn by volunteers. The vibration frequency inside these shapes is fixed at 75 Hz, no vibration outside shapes.

The next set of shapes shown in Figure 5-3 are more complex. The shape (a) is an L structure, which is perceived well except for a minor incorrect estimation of joint plane by user 3 (Figure 5-3 (a3)). In order to enhance the curvature surface detection for shape (b) and (c), we command the vibration at surfaces faster (120 Hz) and the innermost points slower (15 Hz), and the vibration between them linearly change based on their relative distance. User 1 correctly perceived shape (b) and (c). User 2 had slight incorrect curvature estimation in shape (b) but well perceived shape (c). User 3 thought the shape (b) as a tilted partial sphere and shape (c) as a major partial of the upper half of the hollow sphere. Although these estimated shapes were not completely correct, we think majority of the shape information was able to be delivered to the users.

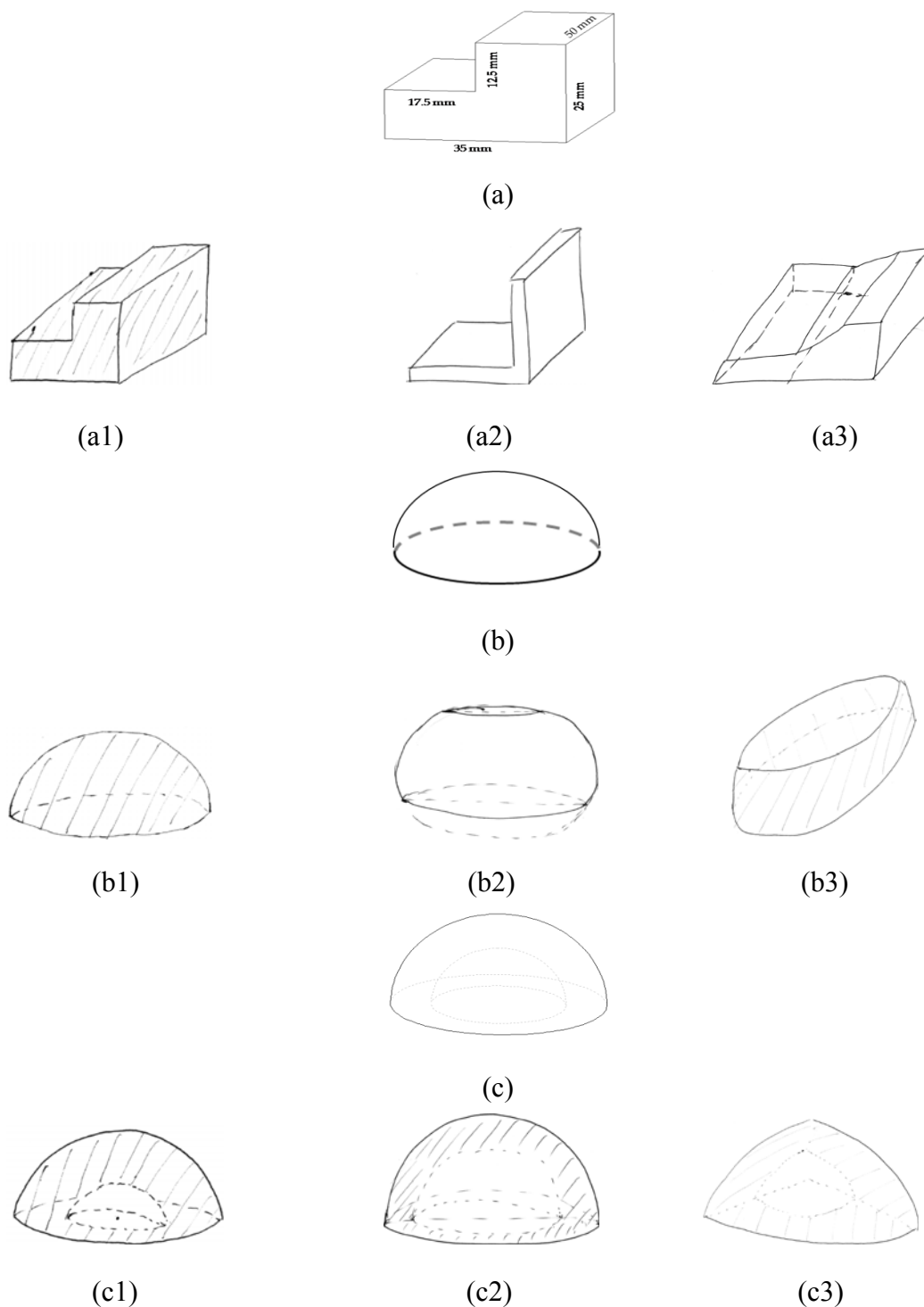


Fig. 5-3 Shape test set 3 (a) L shape structure; (b) Half sphere with 65 mm radius; (c) Half hollow sphere with outer and inner radius of 60 mm and 37 mm respectively. (a1 a2 a3, b1 b2 b3 and c1 c2 c3) are correspondent perceived shapes drawn by volunteers. The vibration frequency for (a) is 75 Hz inside shape, no vibration outside the shape; for (b) is 15 Hz at center of sphere, and linearly increase to 120 Hz at the surface, no vibration outside the sphere; for (c) is 15 Hz at the middle of inner and outer surface, and linearly increase to 120 Hz at inner and outer sphere surfaces.

While the steep vibration change at the shape surface helps with sensing the surface of the object, the perception for large curvature in a small object is more difficult. This can be seen from the shape test set 4 shown in Figure 5-4. The shape (a) is a smaller size /larger curvature sphere compared with shape (b) in set 3. Only user 1 was able to correctly tell the shape, while user 2 and user 3 sensed it as a cube and cylinder respectively. Shape (b) is a small hollow sphere. User 1 correctly perceived the hollow feature of the sphere. User 2 interpreted this shape as four thick plates structure forming a “hollow like” structure, while user 3 considered it as hollow pentahedron.

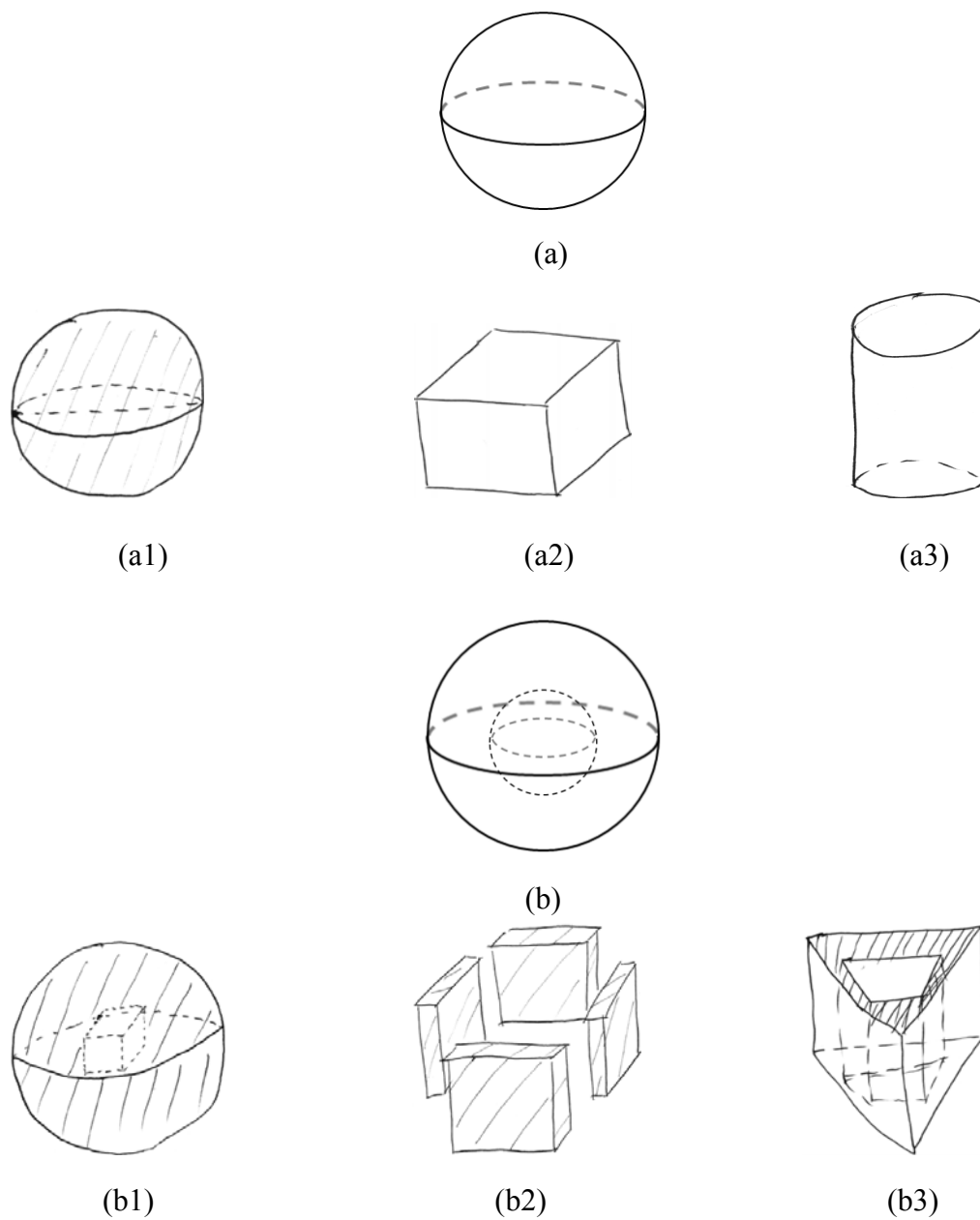


Fig. 5-4 Shape test set 4 (a) sphere with 35 mm radius (b) hollow sphere with outer and inner radius of 30 mm and 20 mm respectively. (a1 a2 a3 and b1 b2 b3) are correspondent perceived shapes drawn by volunteers. The vibration frequency is identically configured to shape test 2 (b) and 2 (c).

5.2 Discussion and Future Work

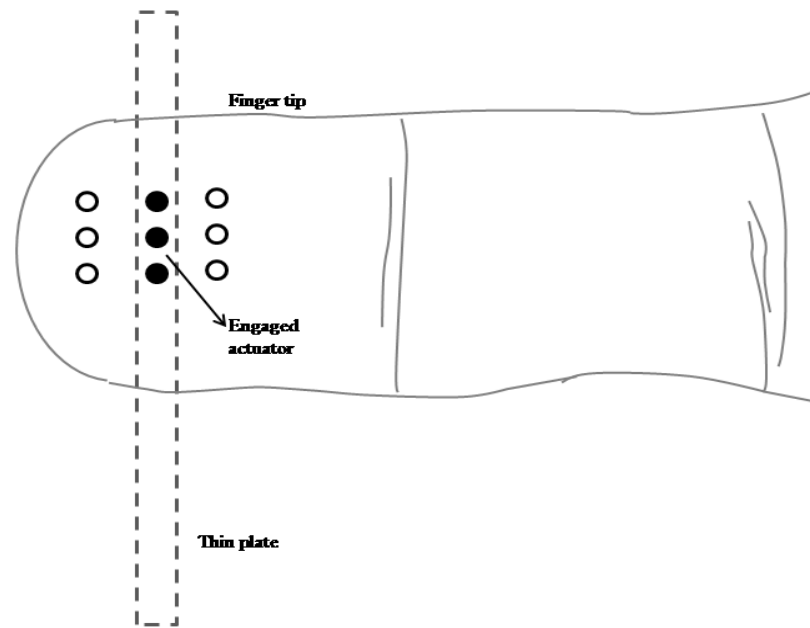
Based on the perception results, we consider displaying thin plate and large curvature is the challenge of the current device. The deficiency comes from that by requiring an intensive scan action, a single actuator can not effectively detect a locally sharp profile. The scan becomes even less effective when the user feels tired after spending a longer perceiving time. Therefore the future work could be focused on using multiple actuators to simultaneously detect a local shape. More actuators should lead to the less scan efforts from users. The benefit of multiple actuators can be described in Figure 5-5 for a better solution to thin plate (Figure 5-5(a)) and curved surface (Figure 5-5(b)) perception. Specifically,

- (1) Further miniaturize the actuator to create more space on finger tip.

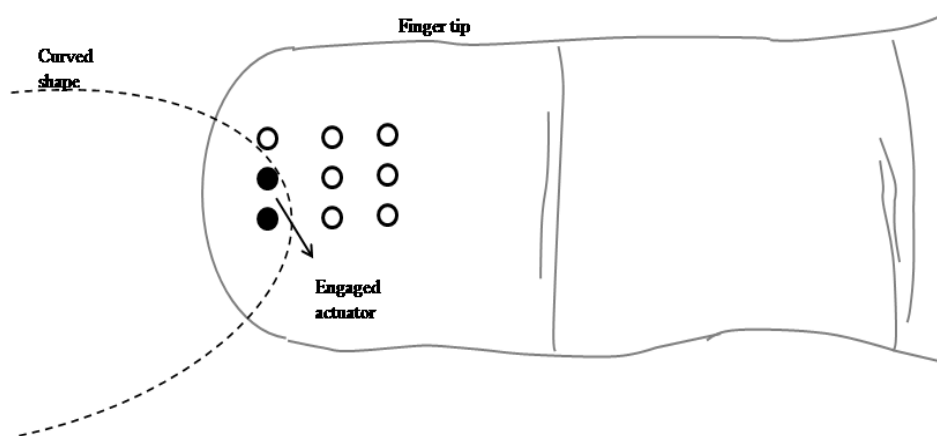
The current actuator features 0.24 mN/mA force characteristics, which provides 60-70 mN peak force during actuation. The reported minimum force required for vibrotactile is around 10 mN. There is still much room for reducing the dimension for both driving coil and permanent magnet.

- (2) Realize 6 DOF position measurement.

The multiple actuators can be engaged by calculating their global coordinates based on their local coordinates and orientation. Therefore it requires 6 DOF position measurement to be available.



(a)



(b)

Fig. 5-5 Multiple actuator solution to (a) thin plate display and (b) curved surface display.

6. CONCLUSION

A 3D tactile display device based on vibrotactile feedback using EM localization has been demonstrated.

We firstly compared DC and AC EM localization methods. AC inductive magnetization method was selected because the corresponding sensitivity is significantly higher. A calibration procedure based on shape functions correlating 3D natural coordinates to Cartesian coordinates was used to accurately adjust the measured position to the actuator's position. A maximal error of 2 mm was found based on 9 testing points in the shape display range, which defined the machine resolution of the shape display. The parallel data processing sequences for PC and microcontroller were designed to realize a 91 s⁻¹ refresh rate for real time position detection. This refresh rate was proved to be sufficient to follow the user's scanning speed during shape perception.

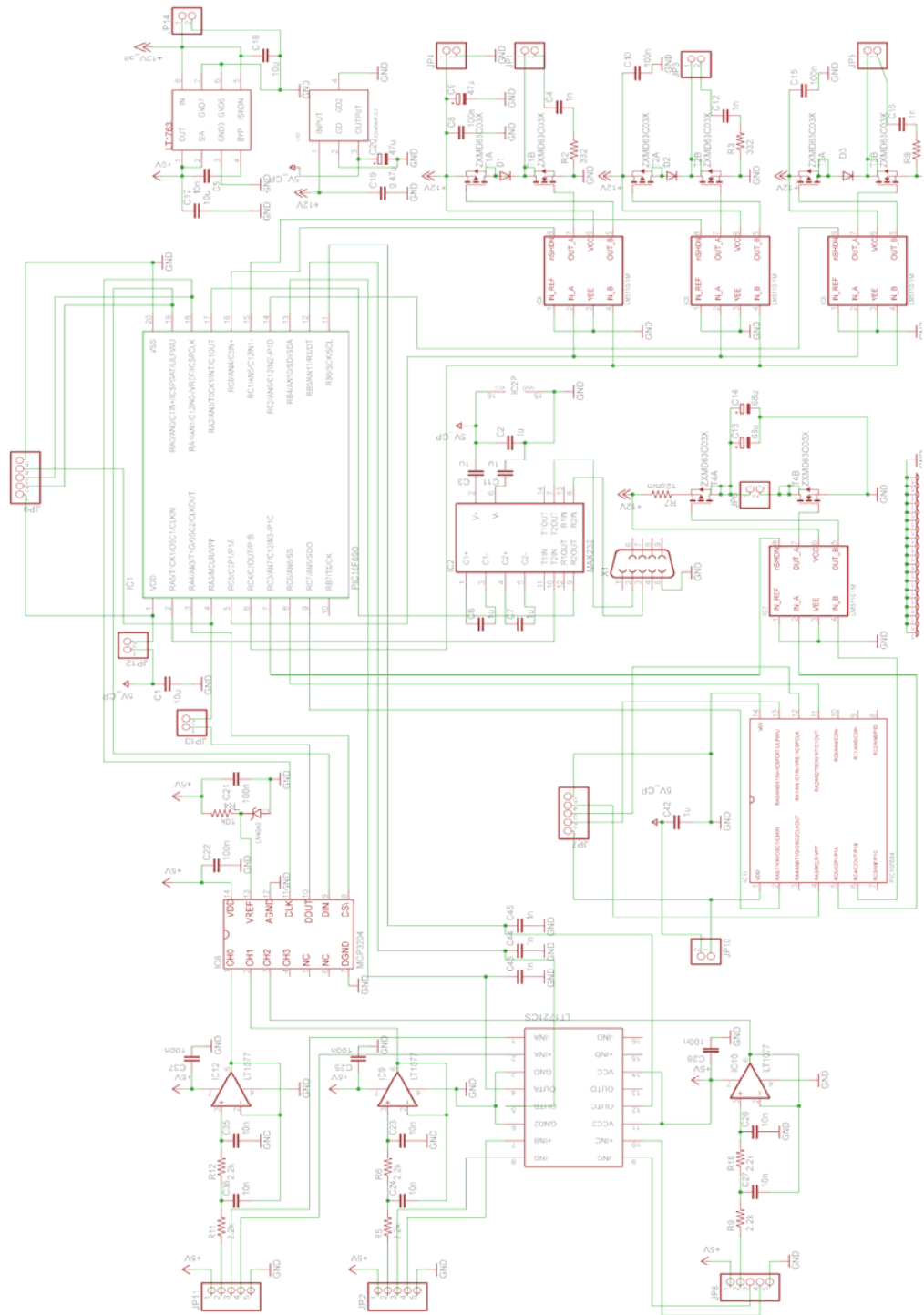
Vibrotactile features higher pain threshold and requires smaller actuation efforts compared with electrotactile and thermotactile. EM based vibrotactile was discussed based on two concepts: eddy current method and permanent magnet method. The eddy current method is not applicable for millimeter size coil since the induced eddy current decays much faster than the pulse width due to a small time constant determined by ratio of coil's inductance and resistance. As a result, the permanent magnet method equivalent to an eddy current but with infinite time constant is desired.

The designed actuator yielded a force characteristics of 0.24 mN/mA and was able to provide clear and comfortable perception to users in its 0~120 Hz working frequency range. A perception limit experiment at four vibration frequencies participated by 3 testers indicated the major mechanoreceptor is Meissner coupuscle in the testing range.

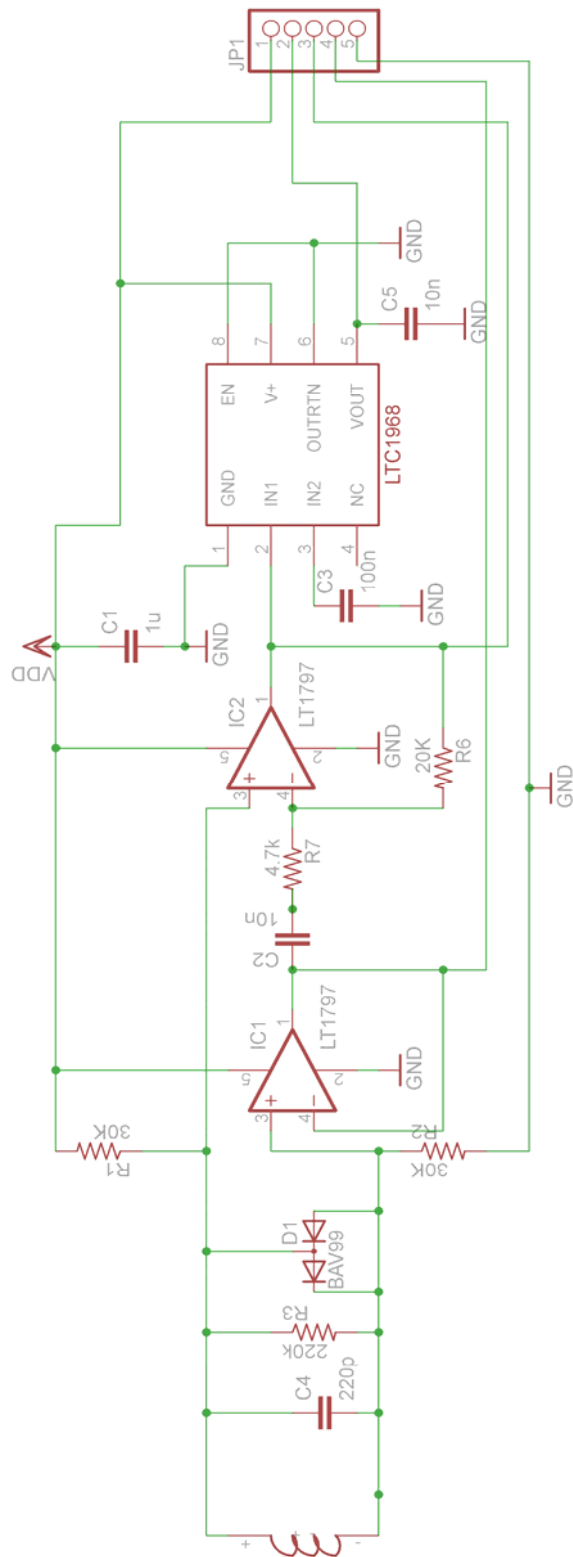
To integrate the device compactly, we developed separate PCBs for each position sensor and mounted them onto a plastic holder. A heat dissipation sink was used to limit the operating temperature below 40 °C in its vibration frequency range. The evaluation of the device was performed by participation of 3 volunteers who did not know the shapes' information prior to the tests. The four sets of shape perception tests indicated: (a) Majority of the shape information was able to be delivered to users using the proposed device. (b) It appeared difficult for thin surface and large curvature surface perception. A possible solution to improve these perceptions is to introduce multiple actuators in the proximity of the fingertip to simultaneously display more information of the local surface.

APPENDICES

APPENDIX A: COMPLETE CIRCUIT SCHEMATICS



1. DRIVER BOARD SCHEMATICS



2. RECEIVER BOARD SCHEMATICS

APPENDIX B: MATLAB SOURCE CODE

1. Main code

```

% Remove existing port taken hardware
out=instrfind;
delete(out);

% Clear the workspace, screen and all existing figures
clear
clc
close all
close hidden all

% Beacon coil's coordinates
c1x=0;      c1y=.1732;   c1z=0;   % Beacon 1
c2x=0.2;    c2y=.1732;   c2z=0;   % Beacon 2
c3x=0.1;    c3y=0;       c3z=0;   % Beacon 3
r1=[c1x c1y c1z]';
r2=[c2x c2y c2z]';
r3=[c3x c3y c3z]';

% Constants used in the formulation and solver
options=optimset('Display','off'); % default setup for FSOLVE
u0=pi*4e-7;                        % Free space permeability
r=2*25.4e-3;                        % Beacon coil's radius
N=[80 80 80];                      % Number of turns of beacon coil 1~3
I=18.072e-3;                       % (0.5V/R=6/332=0.018072)
a=pi*r^2;                          % Area of beacon coil
k=u0*N*I*a/(4*pi);                % Formulation constant

% Measured characteristics of inductance between sensing coils and beacon
%coils
k0=1e9*[1.5 1.55 1.41 1.47 1.45 1.4 1.53 1.45 1.48];
c0=[30 49 70 13 45 70 30 50 70];

% Measured center voltage of the 8 cuboids for calibration procedure
dc=
    [718.6730 462.1956 509.3548 348.1992 463.4824 335.3377 362.8383 272.3622
    604.0097 869.3486    483.6159 636.3365 435.8426 555.7652 370.6391 448.8162

```

486.1514 445.1314 741.2299 684.7082 337.5327 312.6262 466.1506 435.4261];

% Measured calibration matrix with dimension of 24×8

% The used calibration matrix will be selected based on comparison of the measurement with the center voltage

A =

1.0281	-0.2570	-0.3225	0.3581	0.1633	0.1918	-19.3412	-0.1424
0.5153	2.1181	0.3712	-0.6714	-0.2332	-0.6019	33.6836	-1.1132
-0.5646	-0.4475	0.5635	0.5356	0.2808	0.2927	-28.7694	0.7943
-0.3566	-1.2984	-0.8895	1.3142	0.7342	0.7035	-68.1532	1.3394
0.0479	1.2049	-0.1355	0.2082	0.2568	0.1203	-34.6707	-0.6645
0.5928	0.8835	1.1353	-0.7483	-0.2967	-0.3718	36.8502	-0.3859
6.8098	6.2711	3.5142	-5.0362	-3.1857	-3.4524	295.7519	-7.1138
2.9120	4.9046	1.9717	-2.9249	-1.5362	-2.1296	158.2385	-4.0832
-1.0361	-0.5511	0.3165	0.9161	0.6914	0.4772	-62.3975	0.9635
2.3302	1.5475	0.3565	-1.2550	-0.5883	-0.5786	62.2515	-1.5940
0.0507	1.1662	0.0309	0.2621	0.1080	0.0125	-25.2819	-0.6883
0.8525	1.6984	1.5599	-0.9688	-0.3508	-0.7542	41.5063	-1.3068
0.5814	-0.6718	-1.0458	0.5065	0.4610	0.4523	-29.4554	0.9891
-1.2516	1.1060	-0.6577	0.5803	0.9273	0.0592	-48.8037	0.4671
-0.4749	-0.4594	0.5516	0.4487	0.2180	0.2984	-22.7622	0.8166
0.7665	-0.6118	-0.3040	0.5953	0.0287	0.2596	-22.3263	0.4127
0.4813	2.2768	0.5707	-0.3643	-0.0640	-0.6133	5.2522	-1.6717
0.4939	0.6436	0.9960	-0.5882	-0.2266	-0.2135	26.2283	-0.1813

```

0.8207 -0.0702 -1.2206 0.1178 0.4813 0.4084 -19.5594 0.6391
-0.1655 1.6925 -0.4632 -0.3825 0.3462 -0.1742 3.1106 -0.0976
-0.0994 0.2684 0.9139 0.0923 0.1163 -0.0236 -11.7952 -0.0127
4.3906 3.7270 2.3480 -2.4376 -1.8976 -1.9776 138.6771 -4.7309
0.0008 1.3576 -0.0411 0.0708 0.1397 -0.1074 -13.3542 -0.5733
0.1432 0.7028 0.8643 -0.3474 0.0913 -0.1329 2.6861 -0.1895];

```

```
% Port communication setting
```

```

s = serial('COM8'); % Serial port configuration
set(s,'BaudRate',57600); % Boudrate=57.6kbps
set(s,'InputBufferSize',18); % Buffer contains 9 2-byte integers

```

```
% Shape constants (cube)
```

```

x0=100; x01=85; x02=115;
y01=60; y02=90; y0=75;
z0=150; z01=165; z02=135;
dx=20; dy=20; dz=20;

```

```
%Main loop
```

```

p=0; count=1;
fopen(s)
pwm=0;
for p=1:20000, % Number of points to measure
    if p==1, % For the first measurement, send '0' to initiate program
        fwrite(s,pwm,'async') % (this number+1)*.512ms is the PWM period
        V = fread(s,9,'uint16'); % Read data from the input buffer
        fwrite(s,pwm,'async')
    end
end

```

```
for jj=1:length(V) % Determine the sign of each voltage
```

```

    if V(jj)>4096
        V(jj)=V(jj)-4096;
    else
        V(jj)=-V(jj);
    end
end

```

```
end
```

```

vv=[norm(V(1:3));norm(V(4:6));norm(V(7:9))]; % Obtain magnitude of each sensing
voltage

% Find the closest cuboid to the position
for m=1:8,
    d(m)=norm(vv-dc(:,m));
end
for n=1:8,
    x=d(n)-min(d);
    if(x==0)
        break
    end
end

% Get the correspondent calibration matrix
tr=A(((n-1)*3+1):3*n,:);

% Calculate flux density using measured characteristic of inductance between sensing
and beacon coils
for i=1:9,
    if(V(i)>0)
        B(i)=(V(i)-c0(i))/k0(i);
    else
        B(i)=(V(i)+c0(i))/k0(i);
    end
end

% Get magnitudes of flux density
B1=norm(B(1:3)); B2=norm(B(4:6)); B3=norm(B(7:9));

% Compute position
if count==1 % If first point of imaging, find the starting point
    xyz0=[0.1; 0.09; 0.15]; % Initial trial

[xyz]=fsolve(@prexyz,xyz0,options,k,c1x,c1y,c1z,c2x,c2y,c2z,c3x,c3y,c3z,B1,B2,B3
);
    xyz0=[xyz(1); xyz(2); xyz(3)];
else %Else, use previous point of measurement as starting
    xyz0=[xyz(1); xyz(2); xyz(3)];
end

[xyz]=fsolve(@senxyz,xyz0,options,k,c1x,c1y,c1z,c2x,c2y,c2z,c3x,c3y,c3z,B1,B2,B3
);

```

```

% Calibrate this position
xc=tr*[xyz(1:3)*1e3;1e-2*xyz(1)*1e3*xyz(2)*1e3;1e-2*xyz(1)*1e3*xyz(3)*1e3;1e-
2*xyz(2)*1e3*xyz(3)*1e3;1e-6*xyz(1)*1e3*xyz(2)*1e3*xyz(3)*1e3;100];

% Read data for current-step measurement
V = fread(s,9,'uint16');

% Command a vibration frequency based on position, default status is no
%vibration pwm=0.
if (abs(xc(1)-x0)<dx)&&(abs(xc(2)-y0)<dy)&&(abs(xc(3)-z0)<dz)
    pwm=25;    % f=75 Hz
end
fwrite(s,pwm,'async') % send this command through external interrupt
count=count+1;
end

% Remove the defined port function
delete(s)
clear(s)

```

2. Functions

% Prexyz: Use formulation of $B=1.5k/r^3$ to determine initial guess in order to
% improve convergence for solving through Senxyz function.

```
function [XYZ]=prexyz(xyz,k,c1x,c1y,c1z,c2x,c2y,c2z,c3x,c3y,c3z,B1,B2,B3);
```

```
XYZ=
```

```

[ ((k(1)*1.5)/((xyz(1)-c1x)^2+(xyz(2)-c1y)^2+(xyz(3)-c1z)^2)^1.5-B1)*1e12;
  ((k(2)*1.5)/((xyz(1)-c2x)^2+(xyz(2)-c2y)^2+(xyz(3)-c2z)^2)^1.5-B2)*1e12;
  ((k(3)*1.5)/((xyz(1)-c3x)^2+(xyz(2)-c3y)^2+(xyz(3)-c3z)^2)^1.5-B3)*1e12];
```

% Senxyz: Use formulation of equation 2.8 to calculate 3D position
% coordinates.

```
function convg=senxyz(xyz,k,c1x,c1y,c1z,c2x,c2y,c2z,c3x,c3y,c3z,B1,B2,B3);
```

```
global convg
```

```

convg=[((k(1)*3*(xyz(3)-c1z)^2+((xyz(1)-c1x)^2+(xyz(2)-c1y)^2+(xyz(3)-c1z)^2))
^0.5)/((xyz(1)-c1x)^2+(xyz(2)-c1y)^2+(xyz(3)-c1z)^2)^2-B1)*1e12;
```

```

((k(2)*3*(xyz(3)-c2z)^2+((xyz(1)-c2x)^2+(xyz(2)-c2y)^2+(xyz(3)-c2z)^2))^0.5)/((x
yz(1)-c2x)^2+(xyz(2)-c2y)^2+(xyz(3)-c2z)^2)^2-B2)*1e12;
```

```

((k(3)*3*(xyz(3)-c3z)^2+((xyz(1)-c3x)^2+(xyz(2)-c3y)^2+(xyz(3)-c3z)^2))^0.5)/((x
yz(1)-c3x)^2+(xyz(2)-c3y)^2+(xyz(3)-c3z)^2)^2-B3)*1e12];
```

APPENDIX C: ASSEMBLY SOURCE CODE

1. PIC16F690 Source Code for Position Control

```

;*****
;
; Sign detection and actuation frequency modification
;*****

LIST      P=16F690

#include<p16F690.inc>

errorlevel  -302      ;suppress message 302 from list file
errorlevel  -305      ;suppress message 305 from list file

        __CONFIG_CP_OFF & _WDT_OFF & _INTOSCIO & _PWRTE_ON &
        _MCLRE_OFF & _BOR_OFF

#define TxD          PORTA,5      ;Data output for the RS-232
#define TxD_TRIS    TRISA,5

;-----
; Define registers

        cblock    0x20
        PWM_684
        PWM_684_old
        SIGN
        WORK_TEMP
        STATUS_TEMP
        endc

;-----
        org      0x00
        goto    Start

;-----
        org      0x04

```

```

;*****
;
;   Main interrupt code
;*****
;

    btfss    INTCON,INTF ;Test if interrupt is from PWM
    goto    Sign_cap      ; If yes, skip this line

    call RS232RxW      ;Read Actuator frequency from serial port
    movwf   PWM_684

    movf    PWM_684,1
    btfsc   STATUS,Z    ;Test if PWM equal to zero from STATUS,Z
    bcf     PORTC,3     ; If yes, stop actuation

    btfss   STATUS,Z
    call Send_PWM      ;Send the PWM frequency to actuator

    bcf     INTCON,INTF ;Clear interrupt flag bit
    bsf     INTCON,GIE  ;Set global interrupt enable bit

;-----
; Data Processing
;-----
    bsf     PORTC,0     ;Start driver coil 1

;***** Driver coil 1
    call Sign_cal      ;Get sign for driver coil 1

    call FCoil1       ;Measure voltage on finger coil 1
    call FCoil2       ;Measure voltage on finger coil 2
    call FCoil3       ;Measure voltage on finger coil 3

    btfss   SIGN,4     ; Write the sign from driver coil 1 to 4th bit of MSB
                                ; in 3 sensing coils respectively
    bcf     RESULT_HI_1,4
    btfsc   SIGN,4
    bsf     RESULT_HI_1,4

    btfss   SIGN,5
    bcf     RESULT_HI_2,4
    btfsc   SIGN,5
    bsf     RESULT_HI_2,4

```

```

btfss  SIGN,6
bsf    RESULT_HI_3,4
btfsc  SIGN,6
bcf    RESULT_HI_3,4

bcf    PORTC,0      ;Stop driver coil 1
bsf    PORTC,1      ;Start driver coil 2

movf   RESULT_LO_1,w ;Send result from finger coil 1
call  RS232TxW
movf   RESULT_HI_1,w
call  RS232TxW

movf   RESULT_LO_2,w ;Send result from finger coil 2
call  RS232TxW
movf   RESULT_HI_2,w
call  RS232TxW

movf   RESULT_LO_3,w ;Send result from finger coil 3
call  RS232TxW
movf   RESULT_HI_3,w
call  RS232TxW

;***** Driver coil 2
call  Sign_cal      ;Get sign for driver coil 2

call  FCoil1       ;Measure voltage on finger coil 1
call  FCoil2       ;Measure voltage on finger coil 2
call  FCoil3       ;Measure voltage on finger coil 3

btfss  SIGN,4      ; Write the sign from driver coil 2 to 4th bit of MSB
                          ;in 3 sensing coils respectively
bcf    RESULT_HI_1,4
btfsc  SIGN,4
bsf    RESULT_HI_1,4

btfss  SIGN,5
bcf    RESULT_HI_2,4
btfsc  SIGN,5
bsf    RESULT_HI_2,4

```

```

btfss    SIGN,6
bsf      RESULT_HI_3,4
btfsc   SIGN,6
bcf      RESULT_HI_3,4

bcf      PORTC,1      ;Stop driver coil 2
bsf      PORTC,2      ;Start driver coil 3

movf     RESULT_LO_1,w ;Send result from finger coil 1
call RS232TxW
movf     RESULT_HI_1,w
call RS232TxW

movf     RESULT_LO_2,w ;Send result from finger coil 2
call RS232TxW
movf     RESULT_HI_2,w
call RS232TxW

movf     RESULT_LO_3,w ;Send result from finger coil 3
call RS232TxW
movf     RESULT_HI_3,w
call RS232TxW

;***** Driver coil 3
call Sign_cal;Get sign for driver coil 3

call FCoil1      ;Measure voltage on finger coil 1
call FCoil2      ;Measure voltage on finger coil 2
call FCoil3      ;Measure voltage on finger coil 3

btfss    SIGN,4      ; Write the sign from driver coil 3 to 4th bit of MSB
                        ;in 3 Fcoils respectively
bcf      RESULT_HI_1,4
btfsc   SIGN,4
bsf      RESULT_HI_1,4

btfss    SIGN,5
bcf      RESULT_HI_2,4
btfsc   SIGN,5
bsf      RESULT_HI_2,4

```

```

btfss  SIGN,6
bsf    RESULT_HI_3,4
btfsc  SIGN,6
bcf    RESULT_HI_3,4

bcf    PORTC,2      ;Stop driver coil 3
bsf    PORTC,0      ;Start driver coil 1

movf   RESULT_LO_1,w ;Send result from finger coil 1
call  RS232TxW
movf   RESULT_HI_1,w
call  RS232TxW

movf   RESULT_LO_2,w ;Send result from finger coil 2
call  RS232TxW
movf   RESULT_HI_2,w
call  RS232TxW

movf   RESULT_LO_3,w ;Send result from finger coil 3
call  RS232TxW
movf   RESULT_HI_3,w
call  RS232TxW

goto   Wait_1s      ; Wait for 0.3 s if no interruption, end the actuation

      RETFIE
;-----End of main interrupt-----

;*****
;
;   Begin_ADC subroutine
;   Send initializing data to MCP3204 12-bit A/D converter
;   using SPI communication with the PIC16f684.
;*****
Begin_ADC          ;Put /CS low (RA4) and begin sending
  movlw  b'00110111' ;initializing bits
  movwf  PORTA
  movlw  b'00100101'
  movwf  PORTA
  movlw  b'00100111'
  movwf  PORTA

```

```

;***** SGL_DIFF bit - initializing the input channels mode to 1
(1=single/0=differential)

```

```

    movlw b'00100101'
    movwf PORTA
    movlw b'00100111'
    movwf PORTA

```

```

;***** D2 bit - don't care bit for MCP3204

```

```

    movlw b'00100101'
    movwf PORTA
    movlw b'00100111'
    movwf PORTA
    return

```

```

;-----

```

```

;*****

```

```

; CH0 subroutine
; Selects channel 0 on MCP3204 for the current
; A/D conversion.

```

```

;*****

```

```

CH0                ;Select Channel 0 on A/D

```

```

    movlw b'00100100'
    movwf PORTA
    movlw b'00100110'
    movwf PORTA

```

```

    movlw b'00100100'
    movwf PORTA
    movlw b'00100110'
    movwf PORTA
    return

```

```

;-----

```

```

;*****

```

```

; CH1 subroutine
; Selects channel 1 on MCP3204 for the current
; A/D conversion.

```

```

;*****

```

```

CH1                ;Select Channel 1 on A/D

```

```

    movlw b'00100100'

```

```

movwf PORTA
movlw b'00100110'
movwf PORTA

movlw b'00100101'
movwf PORTA
movlw b'00100111'
movwf PORTA
return
;-----

;*****
;
; CH2 subroutine
; Selects channel 2 on MCP3204 for the current
; A/D conversion.
;*****
CH2                ;Select Channel 2 on A/D
    movlw b'00100101'
    movwf PORTA
    movlw b'00100111'
    movwf PORTA

    movlw b'00100100'
    movwf PORTA
    movlw b'00100110'
    movwf PORTA
    return
;-----

;*****
;
; ADC_Continue subroutine
; Continue A/D conversion after choosing the channel.
; Sample voltage and receive data from MCP3204
; using SPI communication with the PIC16f684.
;*****

;***** Register definitions
    cblock
    BITS                ;Number of data bits (4 MSBs and 8 LSBs)
    RESULT_LO           ;The 8 LSBs are stored here

```

```

RESULT_HI      ;The 4 MSBs are stored here
ROT            ;Register used for the rotation of PORTA bits
endc

```

ADC_Continue

```

;***** Sample time needed for charging MCP3204 sample and hold capacitor
;***** (1.5 CLK cycles, 4.5 us)
    nop
    nop
    BCF      PORTA,1
    nop
    nop
    bsf      PORTA,1
    nop
    nop
    BCF      PORTA,1

    clrf RESULT_LO
    clrf RESULT_HI

    bsf      PORTA,1

;***** Data transfer from A/D Converter to PIC16f684
;**** The four MSB's stored in RESULT_HI register
    movlw d'4'
    movwf BITS
Loop1
    BCF      PORTA,1      ;Output data from A/D Converter (clock 掙 falling
edge)
    movf    PORTA,w      ;Read data from PORTA and store to ROT register
    movwf  ROT
    rrf    ROT           ;Rotate right ROT four times, put RA3 bit from ROT to
CARRY
    rrf    ROT
    rrf    ROT
    rrf    ROT
    bsf    PORTA,1      ;Clock rising edge
    rlf    RESULT_HI    ;Rotate left RESULT_HI, put RA1 from
                        ;CARRY to RESULT_HI,0
    decfsz BITS         ;Repeat four times

```

```

    goto    Loop1

;***** The eight LSB's stored in RESULT_LO register
    movlw  d'8'
    movwf  BITS
Loop2
    BCF    PORTA,1    ;Output data from A/D Converter (clock
                    ;falling edge)
    movf   PORTA,w    ;Read data from PORTA and store to ROT
                    ;register
    movwf  ROT
    rrf    ROT        ;Rotate right ROT four times, put RA3 bit from
                    ;ROT to CARRY

    rrf    ROT
    rrf    ROT
    rrf    ROT
    bsf    PORTA,1    ;Clock rising edge
    rlf    RESULT_LO  ;Rotate left RESULT_LO, put RA1 from
                    ;CARRY to RESULT_LO,0

    decfsz BITS      ;Repeat eight times
    goto   Loop2

    movlw  b'00110101' ;End A/D conversion data transfer (putting /CS to
                    ;high)
    movwf  PORTA
    return
;-----

```

```

;*****
;
; RS232TxW & RS232RxW subroutines
; Software implementation of RS-232 serial port.
;
; Baud Rate : 115200 to 4800 bps @ 10MHz
; Data bits : 8
; Stop bits : 1 or 2
; Parity    : None
;
; Usage RS232RxW:  1. Call RS232RxW.
;                  2. Load the byte that is read in W.
;                  3. The data is read from serial port
;

```

```

;
; Usage RS232TxW:  1. Load the byte to be transmitted in W.
;                  2. Call RS232TxW.
;                  3. The data is transmitted to serial port
;
;*****
;***** Definitions
BaudRate      set  d'57600'          ;Set the Baud rate [bps]
Stop_bits     set  1                  ;Set the number of stop bits

Quartz        equ  d'8000000'        ;Internal oscillator frequency [Hz]
Clock         set  (Quartz/4)         ;Instruction cycle frequency [Hz]
CyclesPerBit  set  ((Clock+(BaudRate/2))/BaudRate);Number of cycles per bit
Delay1        set  ((CyclesPerBit-0x11)/3) ;1/3 of bit delay for bit sample
[integer part]
Delay2        set  ((CyclesPerBit-0x11)%3) ;1/3 of bit delay for bit sample
[remainder]
DelayR        set  ((Delay1)/2)       ;Delay for start bit on reading (1/6 bit)
RS_Cyc       set  (0x08+Stop_bits)    ;Number of data bits + stop bits

    if (CyclesPerBit > d'784')
        error "Too slow baud rate for this oscillator!"
    endif

    if (CyclesPerBit < d'17')
        error "Too slow oscillator for this baud rate!"
    endif

;***** Define RS232 signal polarity
Set_RS232Tx_Low    MACRO              ;Set "0" on RS-232 output (+10V)
                    bcf  TxD
                    ENDM

Set_RS232Tx_High  MACRO              ;Set "1" on RS-232 output (-10V)
                    bsf  TxD
                    ENDM

;***** Register definitions
cblock
RX_REG            ;Used for temporary storage for receive

```

```

TX_REG          ;Used for temporary storage for transmit
RS_Bit          ;Bit counter
RS_Bit_R        ;Bit counter
RS_NOP          ;Counter of NOPs
    endc

;-----
RS232TxW
    Set_RS232Tx_Low    ;Start bit
    movwf TX_REG       ;Move data to be sent on TX_REG
    movlw RS_Cyc       ;Number of bits to be send (data+stop bits)
    movwf RS_Bit
    call RS_Delay
    nop
    nop
    nop
    nop

RS_Loop
    btfss TX_REG,0    ;Test TX_REG,0 and output the value on PORTA,5
    goto TxLow
    goto TxHigh

TxHigh
    Set_RS232Tx_High
    goto RS_next

TxLow
    nop
    Set_RS232Tx_Low
    goto RS_next

RS_next          ;Rotate right TX_REG and put the next bit to be sent on
TX_REG,0
    call RS_Delay
    bsf STATUS,C
    rrf TX_REG
    decfsz RS_Bit    ;Decrease the number of bits remaining to be sent with 1
    goto RS_Loop    ;and check if it is not the last one
    nop
    nop
    nop

```

```

nop
nop
return

```

```

;-----
RS232RxW

```

```

    movlw  d'8'      ;Number of bits to be read
    movwf  RS_Bit_R
    call   Start_Delay ;1/2 bit delay for sampling
    nop
    call   RS_Delay   ;1 bit delay for start bit
    nop
    nop
    nop
    nop

```

```

RS_Loop_R

```

```

    btfss  PORTA,2      ;Test PORTA,2 and put the value in STATUS,C
    goto   RxLow
    goto   RxHigh

```

```

RxHigh

```

```

    bsf    STATUS,C
    goto   RS_next_R

```

```

RxLow

```

```

    nop
    bcf    STATUS,C
    goto   RS_next_R

```

```

RS_next_R      ;Rotate right RX_REG and decrease the number of bits to
be read

```

```

    call   RS_Delay
    nop
    rrf    RX_REG
    decfsz RS_Bit_R ;Decrease the number of bits remaining to be read with 1
    goto   RS_Loop_R ;and check if it is not the last one
    nop
    nop
    nop
    nop
    movfw  RX_REG

```

```
return
```

```

;-----
RS_Delay          ;1 RS-232 bit time delay subroutine
    movlw Delay1
    if (Delay1 !=0)
        movwf RS_NOP
Delay_loop
    decfsz RS_NOP
    goto Delay_loop
    endif
    if (Delay2==1)
        nop
    endif
    if (Delay2==2)
        nop
        nop
    endif
    return

;-----
Start_Delay       ;1/2 RS-232 bit time delay subroutine
    movlw DelayR
    if (DelayR !=0)
        movwf RS_NOP
Delay_loop_S
    decfsz RS_NOP
    goto Delay_loop_S
    endif
    return
;*****
;***** Register definition for Finger coil measurements
    cblock
RESULT_LO_1      ;8 LSBs of the averaged voltage on coil1
RESULT_LO_2      ;8 LSBs of the averaged voltage on coil2
RESULT_LO_3      ;8 LSBs of the averaged voltage on coil3
RESULT_HI_1      ;4 MSBs of the averaged voltage on coil1
RESULT_HI_2      ;4 MSBs of the averaged voltage on coil2

```

```

RESULT_HI_3      ;4 MSBs of the averaged voltage on coil3
AVERAGE_LOW     ;Temporary storage of the averaging sum for low byte
AVERAGE_HIGH   ;Temporary storage of the averaging sum for high byte
AVERAGE_CARRY  ;Temporary storage of the averaging sum carry bits
AVERAGE_COUNT  ;Averaged data counter
    endc
;-----

;*****
;
; FCoil1 routine
; Measures 8 times and averages the voltage
; on finger coil 1.
; Uses Begin_ADC, CH0 and ADC_Continue subroutines.
;*****
FCoil1
    movlw d'8'
    movwf AVERAGE_COUNT
    clrf AVERAGE_LOW
    clrf AVERAGE_HIGH
    clrf AVERAGE_CARRY
Average_loop1
    call Begin_ADC
    call CH0
    call ADC_Continue

    movf RESULT_HI,w
    addwf AVERAGE_HIGH

    movf RESULT_LO,w
    addwf AVERAGE_LOW
    movlw 0
    btfsc STATUS,C
    movlw 1
    addwf AVERAGE_CARRY
    decfsz AVERAGE_COUNT
    goto Average_loop1

    movf AVERAGE_CARRY,w
    addwf AVERAGE_HIGH

```

```

    rrf    AVERAGE_HIGH
    rrf    AVERAGE_LOW
    bcf    AVERAGE_HIGH,7

    rrf    AVERAGE_HIGH
    rrf    AVERAGE_LOW
    bcf    AVERAGE_HIGH,7

    rrf    AVERAGE_HIGH
    rrf    AVERAGE_LOW
    bcf    AVERAGE_HIGH,7

    movf   AVERAGE_LOW,w
    movwf  RESULT_LO_1
    movf   AVERAGE_HIGH,w
    movwf  RESULT_HI_1
    return
;-----

;*****
;
;   FCoil2 routine
;   Measures 8 times and averages the voltage
;   on finger coil 2.
;   Uses Begin_ADC, CH1 and ADC_Continue subroutines.
;*****
FCoil2
    movlw  d'8'
    movwf  AVERAGE_COUNT
    clrf  AVERAGE_LOW
    clrf  AVERAGE_HIGH
    clrf  AVERAGE_CARRY
Average_loop2
    call  Begin_ADC
    call  CH1
    call  ADC_Continue
    movf  RESULT_HI,w
    addwf AVERAGE_HIGH

    movf  RESULT_LO,w
    addwf AVERAGE_LOW
    movlw 0

```

```

btfsc STATUS,C
movlw 1
addwf AVERAGE_CARRY
decfsz AVERAGE_COUNT
goto Average_loop2

movf AVERAGE_CARRY,w
addwf AVERAGE_HIGH

rrf AVERAGE_HIGH
rrf AVERAGE_LOW
bcf AVERAGE_HIGH,7

rrf AVERAGE_HIGH
rrf AVERAGE_LOW
bcf AVERAGE_HIGH,7

rrf AVERAGE_HIGH
rrf AVERAGE_LOW
bcf AVERAGE_HIGH,7

movf AVERAGE_LOW,w
movwf RESULT_LO_2
movf AVERAGE_HIGH,w
movwf RESULT_HI_2
return

```

```

;-----

```

```

;*****
;
; FCoil3 routine
; Measures 8 times and averages the voltage
; on finger coil 3.
; Uses Begin_ADC, CH2 and ADC_Continue subroutines.
; Duration: 723.5 us
;*****
;

```

```

FCoil3

```

```

movlw d'8'
movwf AVERAGE_COUNT
clrf AVERAGE_LOW
clrf AVERAGE_HIGH

```

```

    clrf AVERAGE_CARRY
Average_loop3
    call Begin_ADC
    call CH2
    call ADC_Continue
    movf    RESULT_HI,w
    addwf   AVERAGE_HIGH

    movf    RESULT_LO,w
    addwf   AVERAGE_LOW
    movlw   0
    btfsc   STATUS,C
    movlw   1
    addwf   AVERAGE_CARRY
    decfsz  AVERAGE_COUNT
    goto    Average_loop3

    movf    AVERAGE_CARRY,w
    addwf   AVERAGE_HIGH

    rrf     AVERAGE_HIGH
    rrf     AVERAGE_LOW
    bcf     AVERAGE_HIGH,7

    rrf     AVERAGE_HIGH
    rrf     AVERAGE_LOW
    bcf     AVERAGE_HIGH,7

    rrf     AVERAGE_HIGH
    rrf     AVERAGE_LOW
    bcf     AVERAGE_HIGH,7

    movf    AVERAGE_LOW,w
    movwf   RESULT_LO_3
    movf    AVERAGE_HIGH,w
    movwf   RESULT_HI_3
    return
;-----

```



```

;-----
;   Send PWM frequency to the actuator uC
;-----

    cblock
    Delay_1
    Delay_2
    BITCOUNT
    endc

Send_PWM
    movfw  PWM_684_old    ;Compare the new and old PWM
    xorwf  PWM_684,0     ;don't send if the same
    btfsc  STATUS,Z
    goto   Act_on

    movfw  PWM_684
    movwf  PWM_684_old

    movlw  d'8'         ;Set the number of bits to be sent
    movwf  BITCOUNT

Send_loop
    btfss  PWM_684,0    ;Set the data pin to the state of the LSB
    bcf    PORTC,7
    btfsc  PWM_684,0
    bsf    PORTC,7

    bsf    PORTC,6      ;Rising edge of clock

    btfsc  BITCOUNT,3
    call  Delay_long
    btfss  BITCOUNT,3
    call  Delay_short

    bcf    PORTC,6      ;Falling edge of clock

    rrf    PWM_684
    decfsz BITCOUNT
    goto   Send_loop

```

```

Act_on
    bsf    PORTC,3          ;Trun on actuator driver
    return

```

```

Delay_long
    movlw  d'200'          ;Set delay time 1 (~300 us)
    movwf  Delay_1
    decfsz Delay_1
    goto   $-1
    return

```

```

Delay_short
    movlw  d'2'           ;Set delay time 2 (~5 us)
    movwf  Delay_2
    decfsz Delay_2
    goto   $-1
    return

```

```

;-----
; 0.3s Wait loop for end of actuation
;-----

```

```

Wait_1s
    cblock
        Wait_11
        Wait_12
    endc

    movlw  d'255'
    movwf  Wait_11
Wait_loop1
    movlw  d'255'
    movwf  Wait_12
    decfsz Wait_12
    goto   $-1
    decfsz Wait_11
    goto   Wait_loop1

    bcf    PORTC,3        ;stop actuation
    return

```

```

;*****
;

```

```

; Main program
; Initialize oscillator frequency, PWM mode,
; RS-232 and SPI ports. Enable external interrupt.
;*****
Start
  clrf PORTA
  clrf PORTC
  clrf  PORTB
  clrf PWM_684_old

  BANKSEL ANSEL      ;Bank 2
;-----
  clrf ANSEL
  clrf ANSELH

  BANKSEL OSCCON      ;Bank 1
;-----
  movlw b'01110000' ;Set internal oscillator frequency to 8 MHz
  movwf OSCCON
  movlw d'15'      ;Set PWM frequency to 125 kHz
  movwf PR2

  bsf TRISA,3      ;Set RA3 to input (SPI Data_in)
  bsf TRISA,2      ;Set RA2 to input (RS-232 data input port)
  BCF TRISA,0      ;Set RA<0,1,4> to output:
  BCF TRISA,1      ;RA0 ?SPI Data_out, RA1 ?SPI clock,
  BCF TRISA,4      ;RA4 - /CS (MCP3204 chip select)
  BCF TxD_TRIS    ;Set RA5 to output (RS-232 data output port)
  movlw b'11111111'
  movwf TRISB      ;Set PORTB to input
  clrf TRISC       ;Set PORTC to output

  BCF OPTION_REG,INTEDG ;Set interrupt on falling edge on
                        ;RA2 pin

  BANKSEL PORTC    ;Bank 0
;-----
  movlw b'10000000' ;Set PWM switching delay to 0 us
  movwf PWM1CON
  movlw b'10001101' ;Half bridge, DC 2 LSBs, PWM: P1A active-high,
                    ;P1B active-low
  movwf CCP1CON

```

```
movlw b'00001000' ;DC 8 MSBs (DC=50%)
movwf CCPR1L
bcf   PIR1,1      ;Clear TMR2 interrupt flag
movlw b'00000100' ;TMR2 ON (Start PWM), Prescaler = 1
movwf T2CON
```

```
movlw b'11010000' ;Enable global, peripheral and RA2 pin interrupts
movwf INTCON
```

```
Loop_wait_for_INT
```

```
    nop
```

```
    nop
```

```
    goto Loop_wait_for_INT
```

```
-----
```

```
END
```

2. PIC16F684 Source Code for Actuation Frequency Control

```

;*****
;
;               Actuator controller
;*****

LIST          P=16F684

#include<p16F684.inc>

errorlevel  -302          ;suppress message 302 from list file
errorlevel  -305          ;suppress message 305 from list file

    __CONFIG _CP_OFF & _WDT_OFF & _INTOSCIO & _PWRTE_ON &
    _MCLRE_OFF

    cblock    0x20
INTCOUNT          ;Number of points to measure and send to PC
PWM
DC_PWM
    endc

;-----
    org      0x00
    goto    Start

;-----
;*****
;
;   Main interrupt code
;*****
    org      0x04

;-----
    bcf     T2CON,2      ;TMR2 OFF (Stop PWM)
    clrf   TMR2         ;Clear Timer2 register

    BANKSEL OSCCON      ;Go to Bank 1

;-----
    movlw  b'01110000' ;Set internal oscillator frequency to 8 MHz
    movwf  OSCCON

    BANKSEL INTCOUNT ;Bank 0

```

```

;-----
    movlw d'7'           ;7 more "interrupts" are to occur
    movwf INTCOUNT

PWM_Read
    btfsc PORTA,5
    bsf STATUS,C
    btfss PORTA,5
    bcf STATUS,C
    bcf INTCON,INTF ;Clear RA2 interrupt flag
    btfss INTCON,INTF ;Check if flag is set again
    goto $-1

    rrf PWM
    decfsz INTCOUNT
    goto PWM_Read
    btfsc PORTA,5
    bsf STATUS,C
    btfss PORTA,5
    bcf STATUS,C
    rrf PWM
    movfw PWM
    movwf DC_PWM
    bcf STATUS,C
    rrf DC_PWM
    movfw DC_PWM
    movwf CCPR1L
    movfw PWM
    BANKSEL OSCCON ;Go to Bank 1
;-----

    movwf PR2
    movlw b'00010000' ;Set internal oscillator frequency to 125 kHz
    movwf OSCCON
    BANKSEL T2CON ;Go to Bank 0
;-----

    bsf T2CON,2 ;TMR2 ON (Start PWM)
    bcf INTCON,INTF ;Clear flag bit
    RETFIE
;*****
;
;*****
;

```

```

; Main program
; Initialize oscillator frequency, PWM mode, ADC,
; RS-232 ports. Enable external interrupt.
;*****
;
Start
    clrf    PORTC
    clrf    PORTA
    clrf    PWM
    clrf    DC_PWM

    movlw  07h        ;Disconnect RA<2:0> and RC<4,1:0> from built-in
                    ;comparator
    movwf  CMCON0

    movlw  b'10001101' ;Set PWM: Half Bridge forward, DC 2 LSBs = 00,
    movwf  CCP1CON    ;P1A & P1C active-high, P1B & P1D active-high

    bsf    T2CON,1    ;Set Timer2 prescaler to 16

    BANKSEL OSCCON    ;Bank 1
;-----
    clrf  TRISC      ;Set PORTC outputs for the PWM
    clrf  TRISA
    bsf  TRISA,2    ;Set RA2 to input (PWM clock input pin/Interrupt source)
    bsf  TRISA,5    ;Set RA5 to input (PWM data input pin)

    clrf  ANSEL

    bsf  OPTION_REG,INTEDG ;Set interrupt on rising edge on RA2 pin

    movlw b'00010000' ;Set internal oscillator frequency to 125 kHz
    movwf OSCCON

    BANKSEL INTCON    ;Go to Bank 0
;-----
    movlw b'10010000' ;Enable the RA2/INT external interrupt
    movwf INTCON

    bcf  PIR1,1      ;Clear TMR2 interrupt flag

Loop_wait_for_INT
    nop

```

```
    nop  
    goto Loop_wait_for_INT  
;-----  
END
```

APPENDIX D: ANSYS SOURCE CODE

```

!*****
! Solver preference setting
!*****
/COM,
/COM,Preferences for GUI filtering have been set to display:
/COM,  Magnetic-Nodal
/COM,  Magnetic-Edge
!*
/PREP7

!*****
! Model parameters setting
!*****
*SET,mu0,4*3.1416e-7      !Free space permeability
*SET,l,5e-3              !Thickness of coil
*SET,r2,1.0e-3           !Outer radius
*SET,r1,.6e-3            !Inner radius
*SET,br,.75              !Residual flux density
*SET,hc,460000           !Coercive force
*SET,mup,br/mu0/hc      !Relative permeability of magnet
*set,mui,200             !Relative permeability of iron core
*SET,a,2e-3              !Side length of magnet
*SET,h,1e-3              !Thickness of magnet
*set,h0,0.02e-3         !Gap between magnet and coil for convergence
*set,i,.55*450          !Total current
*set,s,(r2-r1)*l        !Cross section area

!*****
! Create models
!*****
et,1,117
mp,murx,1,1
mp,murx,2,mui
mp,mgzz,3,hc
mp,murx,3,mup
mp,murx,4,1

```

```

CYLIND,r2,r1,l/2,-l/2,0,360,          ! Create coil model
CYLIND,r1, ,l/2,-l/2,0,360,
BLOCK,-a/2,a/2,a/2,-a/2,l/2+h0,l/2+h0+h,      ! Create magnet model
BLOCK,-10*r2,10*r2,-10*r2,10*r2,-10*r2,10*r2+h, ! Create boundary box

```

```

local,11,1          ! Assign material 1 to coil

```

```

vsel,s,,1

```

```

VATT,      1, ,    1,      11

```

```

vsel,s,,2

```

```

VATT,      2, ,    1,      0          ! Assign material 2 to magnet

```

```

vsel,s,,3

```

```

VATT,      3, ,    1,      0          ! Assign material 3 to core

```

```

vsel,all

```

```

vsbv,4,1,,,keep

```

```

vsbv,5,2,,,keep

```

```

vsbv,4,3,,,keep

```

```

vsel,u,mat,,1

```

```

vsel,u,mat,,2

```

```

vsel,u,mat,,3

```

```

VATT,      4, ,    1,      0

```

```

!*****

```

```

! Mesh all volumes

```

```

!*****

```

```

ALLSEL,ALL

```

```

nummrg,all

```

```

smrt,3

```

```

mshape,1,3d

```

```

mshkey,0

```

```

vmesh,all

```

```

vsel,s,,1

```

```

eslv,s

```

```

!*****

```

```

! Apply current to coil

```

```

!*****

```

```

bfe,all,js,1,-i/s,,

```

```

!*****

```

!Apply boundary conditions

!*****

```

asel,s,loc,x,-10*r2
asel,a,loc,x,10*r2
asel,a,loc,y,10*r2
asel,a,loc,y,-10*r2
asel,a,loc,z,-10*r2
asel,a,loc,z,10*r2+h
da,all,az,0

```

!*****

! Define component- force on magnet

!*****

```

vsel,s,mat,,3
eslv,s
cm,ss,elem
FMAGBC,'SS'
finish

```

!*****

! Solve the problem

!*****

```

/SOL
eqslv,sparse
ALLSEL,ALL
solve
FINISH
/POST1

```

!*****

! Display the magnetic force

!*****

```

FMAGSUM,'SS'
FINISH

```

REFERENCES

- [1] T. Fukuda, H. Morita and F. Arai et al, "Micro resonator using electromagnetic actuator for tactile display", *1997 International Symposium on Micromechatronics and Human Science*, pp: 143-148, 1997.
- [2] M. Hafez, M. B. Khoudja and J. M. Alexandre et al, "Electromagnetically driven high-density tactile interface based on a multi-layer approach", *2003 International Symposium on Micromechatronics and Human Science*, pp. 147-152, 2003.
- [3] T. Maucher, J. Schemmel and K. Meier, "The Heidelberg tactile vision substitution system", *Proceeding of the 6th International Conference on Tactile Aids, Hearing Aids and Cochlear Implants*, May 2000.
- [4] H. Iwata, H. Yano, and F. Nakaizumi et al, "Project FEELEX: Adding haptic surface to graphics", *Proceedings of the 28th Annual Conference on Computer Graphics and Interactive Techniques*, pp: 469-476, 2001.
- [5] Y. Kawai, N. Ohnishi and N. Sugie, "A support system for the blind to recognize a diagram", *Systems and Computers in Japan*, vol. 21, No. 7, pp.75-85, 1990.
- [6] Y. Kawai and F. Tomita, "Interactive tactile display system – A support system for the visually disabled to recognize 3D objects", *ASSETS'96*, pp. 45-50, 1996.
- [7] M. Shinohara, Y. Shimizu and A. Mochizuki, "Three-dimensional tactile display for the blind", *IEEE Transactions on Rehabilitation Engineering*, vol. 6, No. 3, pp. 249-256, 1998.
- [8] T. Iwamoto, M. Tatzono and H. Shinoda, "Non-contact method for producing tactile sensation using airborne ultrasound", *EuroHaptics 2008*, pp. 504-513, 2008.
- [9] T. H. Massie and J. K. Salisbury, "The PHANTom haptic interface: A device for probing virtual objects", *Proceedings of the ASME Winter Annual Meeting, Symposium on Haptic Interfaces for Virtual Environment and Teleoperator Systems*, Nov. 1994.
- [10] Y. Hirata and M. Sato, "3-Dimensional interface device for virtual work space", *Proceedings of the 1992 IEEE/RSJ International Conference on Intelligent Robots and Systems*, pp.889-896, July 7-10, 1992.

- [11] A. Fischer and J. M. Vance, "PHANToM haptic device implemented in a projection screen virtual environment", *7th International Immersive Projection Technologies Workshop*, pp.225-230, 2003.
- [12] J. Murayama, L. Bougrila and Y. Luo et al, "SPIDAR G&G: A two-handed haptic interface for bimanual VR interaction", *Proceedings of EuroHaptics 2004*, pp. 138-146, June 5-7, 2004.
- [13] G. Nikolakis, D. Tzovaras and S. Moustakidis et al, "CyberGrasp and PHANToM integration: Enhanced haptic access for visually impaired users", *SPECOM' 2004*, Sep 20-22, 2004.
- [14] Immersion CyberGrasp™,
www.est-kl.com/hardware/gloves/immersion/cybergrasp.html, 2009.
- [15] F. V. Verdu and M. Hafez, "Graphical tactile displays for visually impaired people", *IEEE Transactions on Neural Systems and Rehabilitation Engineering*, vol.15, no.1, pp: 119-130, 2007.
- [16] H. Noma, Y. Yanagida and N. Tetsutani, "The proactive desk: A new force display system for a digital desk using a 2-DOF linear induction motor", *Proceedings of IEEE Virtual Reality 2003*, pp. 217-224, 2003.
- [17] K. A. Kaczmarek, J. G. Webster and P. B. Rita, "Electrotactile and vibrotactile displays for sensory substitution systems", *IEEE Transactions on Biomedical Engineering*, vol.38, no.1, pp:1-16, 1991.
- [18] G. Baratoff and S. Blanksteen, Tracking Devices,
www.hitl.washington.edu/scivw/EVE/I.D.1.b.TrackingDevices.html, 2008.
- [19] Honeywell Inc. Hall Effect Sensors,
<http://content.honeywell.com/sensing/prodinfo/solidstate/technical/chapter2.pdf>, 2009
- [20] General Magnetoresistive Sensors for Magnetic Field Measurement
www.nxp.com/acrobat_download/various/SC17_GENERAL_MAG_2-1.pdf, 2009.
- [21] Wikipedia, Faraday's Law of Induction,
http://en.wikipedia.org/wiki/Electromagnetic_induction, 2009.
- [22] Wikipedia, Hall Effect, en.wikipedia.org/wiki/Hall_effect, 2008

- [23] ZETEX Inc., Magnetoresistive Sensors,
<http://bestinbipolars.com/3.0/appnotes/apps/an20.pdf>, 2009
- [24] H. Blanchard, Ch. Schott, High Sensitivity Hall Sensor,
<http://lmis3.epfl.ch/research/old/cylhall/CYHdatasheets.pdf>, 2008
- [25] GMW Associates, Asahi Hall Element Magnetic Sensors,
www.gmw.com/magnetic_sensors/asahi/documents/hw-101a-4t_gmw.pdf, 2008
- [26] GMW Associates, Asahi Hall Element Magnetic Sensors,
www.gmw.com/magnetic_sensors/sentron/csa/documents/CSA-1V-SO%20Lead%20Free%20Specification.pdf, 2008
- [27] E. A. Prigge and J. P. How, “Signal architecture for a distributed magnetic local positioning system”, *IEEE Sensors Journal*, vol.4, no.6, pp: 864-873, 2004.
- [28] Wire Gauge and Current Limit,
http://www.powerstream.com/Wire_Size.htm, 2009
- [29] Wikipedia, Skin depth, http://en.wikipedia.org/wiki/Skin_depth, 2008
- [30] Glenn Elert, Resistivity of Copper,
<http://hypertextbook.com/facts/2004/BridgetRitter.shtml>, 2008
- [31] Y. Ulgen, M. Sezdi, “Estimating the resistivity of the interior fluid of red blood cells using fricke’s equation”, *Proceedings of the 19th IEEE/EMBS International Conference*, pp: 2112-2115, Oct.30 – Nov.2, 1997.
- [32] S. S. Rao, *The Finite Element Method in Engineering*, Elsevier, 2005
- [33] KGS ASSISTIVE TECHNOLOGY,
www.kgs-america.com/product_at.html, 2009
- [34] J. Pasquero and V. Hayward, “A practical tactile display system with one millimeter spatial resolution and 700 Hz refresh rate”, *Proceedings of Eurohaptics 2003*, p94-110, July 2003,
- [35] H. Janocha and C. Stiebel, “New approach to a switching amplifier for piezoelectric actuators,” *Actuator 98*, pp. 191-194, 1998.
- [36] S. Robinson, *Design Solution Analog*,

www.cirrus.com/en/pubs/whitePaper/1105_Drive_PE_Actuators_with_Op_Amps.pdf.
2009

[37] R. M. Bowley, P. J. King and G. J. Lewis et al, "Production of short mechanical impulses by means of eddy currents", *IEE Proceedings: Part B Electric Power Applications*, vol. 130, no. 6, pp: 415-423, 1983.

[38] P. P. Mongeau, "Coaxial Air Core Electromagnetic Accelerators", *PhD Dissertation*, MIT, chapter 2, pp: 90-127, October 1981.

[39] L. H. de Medeiros, G. Reyne and G. Meunier, "About the distribution of forces in permanent magnets", *IEEE Transactions on Magnetics*, vol.35, no.3, pp: 1215-1218, May 1999.

[40] J. Z. Wu, K. Krajnak, and D. E. Welcome, "Analysis of the dynamic strains in a fingertip exposed to vibrations: correlation to the mechanical stimuli on mechanoreceptors", *Journal of Biomechanics* 39, pp: 2445-2456, 2006.

[41] K. Deng, E. T. Enikov and H. Zhang, "Development of a pulsed micro-actuator for 3D tactile display", *2007 IEEE/ASME International Conference on Advanced Intelligent Mechatronics*, pp. 1-5, Sep4-7, 2007.